Research on Transmitarray Antennas with Enhanced Performance and Expanded Functionalities

Abstract

Novel high-gain antennas are emerging in a wide range of applications such as satellite communications, 5G wireless communications, and remote sensing. As the combination of lens antennas and microstrip array antennas, transmitarray antenna creates a hybrid high-gain antenna with advantages of being low-profile, light weight, and versatile radiation performances. In this dissertation, methods for designing transmitarray antennas with enhanced performance and expanded functionalities are investigated.

Transmitarray elements with Fabry-Pérot-like cavity are discussed in detail, with a focus on operation principle. The generalized scattering matrix-based analysis approach for layered element evaluation is presented. Array factor-based approach for computing radiation pattern is formulated.

By involving complete transmission amplitude and phase control into consideration, an amplitude-phase synthesis method is developed for designing transmitarray antennas with an expected shaped beam for satellite communications, which is composed of two parts—transmitarray element design and transmitarray synthesis. For the element design, a three-layer transmitarray element with full-coverage of complex transmission coefficient is developed. For the transmitarray synthesis, an amplitude-phase synthesis technique, based on particle swarm algorithm, is developed for optimizing element distribution on the transmitarray aperture. Transmission amplitude control is included during the synthesis process. A transmitarray antenna with a flat-top radiation pattern has been designed, fabricated and tested. Compared with the conventional phase-only synthesis method, the developed amplitude-phase synthesis method offers feature of flexible beam-shaping capability.

In order to enhance the aperture efficiency of transmit-reflect-combined-array antennas, a novel four-layer unit cell is proposed. The element has the features of

simultaneous and decoupled control of transmission phase and reflection phase. Besides, the element demonstrates stable responses under oblique incidence for both transmission and reflection, which is vital for antenna efficiency. Based on the element, a single-feed transmit-reflect-combined-array antenna has been designed, fabricated, and tested. The resulting antenna achieves better performance in terms of aperture efficiency than the existing designs. Moreover, by slanting the source feed, simultaneously bidirectional capability of the antenna is confirmed.

In order to realize wideband transmitarray antennas in a low-cost and reduced-complexity manner, an efficient approach is proposed. The design approach combines two different techniques—1-bit phase quantization and phase distribution optimization. First, a 3-layer 1-bit unit cell is designed. The 1-bit element is used to introduce phase error on the aperture. Then, considering the element performance, the phase distribution at multiple frequency points is optimized with modified weight at each frequency point to further balance the gain curve. The optimization is based on redistribute the phases on the aperture for all the desired frequency points to minimize the influence of large phase errors on the basis of ensuring wideband characteristics. A 13×17-element transmitarray antenna working at 10 GHz is designed, fabricated, and tested. 1-dB fractional gain bandwidth of 37% is achieved. Considering the low-cost fabrication and reduced-complexity of the system design, the proposed approach is a valid alternative for designing wideband transmitarray antennas.

In summary, different challenges for designing transmitarray antennas with enhanced performance and expanded functionalities have been addressed. Several novel designs have been proposed, detailed design procedures have been presented, and numerical and experimental studies have been carried out for verification.

Acknowledgments

Foremost, I would like to sincerely thank my supervisor Prof. Qiang Chen for his constant support and mentorship throughout my studies. I am extremely grateful for his patience and effort in guiding and teaching me.

I would like to thank Prof. Taiichi Otsuji, Prof. Noriharu Suematsu, and Prof. Keisuke Konno for being my examination committees. It was not possible for improving this thesis without their valuable feedback and comments.

I am very grateful to Prof. Hiroyasu Sato for the helpful guidance in experimental settings. I would like to sincerely thank Prof. Qiaowei Yuan for providing me valuable support.

I would also like to thank for the many friendships that I have built with the students and staffs in Tohoku University. In particular, I would like to thank Jiyao Yu and Hejie Yan for the many insightful conversations and unmemorable experiences.

Finally, I would like to express my deep appreciation to my parents and my parents-in-law for their unconditional support and encouragement. Most of all, I would like to thank my beloved wife for sharing every step of this journey with me. I could not have asked for a better companion through life's adventures.

Contents

List of Tables

List of Figures

Chapter 1

Introduction

1.1 Overview of Transmitarray Antennas and Related State-of-the-Art Research

With the rapid development of printed circuit board technology, a new kind of high-gain antennas, namely transmitarray antennas, that combine the advantages of lens antennas and phased array antennas have gained much attentions recently. Figure 1-1 shows the general description of a transmitarray antenna. It typically consists of a source feed and a flat transmitarray aperture. Illuminating by the source feed, the transmitarray aperture can generate a collimated beam in desired direction. The transmitarray aperture is composed of a large number of transmitarray elements, each of which can be individually designed to control the transmission amplitude and phase.

Figure 1-2 shows the typical antenna technologies that are related to transmitarray antennas. Although the design principles of transmitarray antennas and phased array antennas, as shown in Figure 1-2 (b), are the same, which are based on individually controlling the excitation of the elements to form a collimated beam in desired direction, the main distinction lies in the feeding mechanism. The phased array antenna uses a feeding network, leading to severe loss and complex design. However, the only required one for transmitarray antenna is a spacing source feed. Besides, compared with lens antennas, as shown in Figure 1-2 (a), where curved surfaces are required, the transmitarray antennas are more easy-to-fabricate and low-profile.

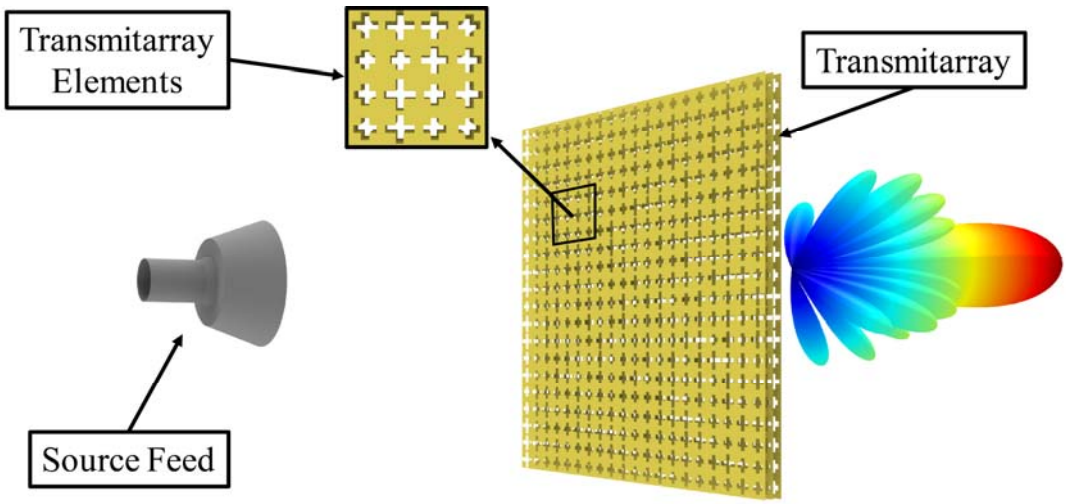

Figure 1-1 General Description of a transmitarray antenna.

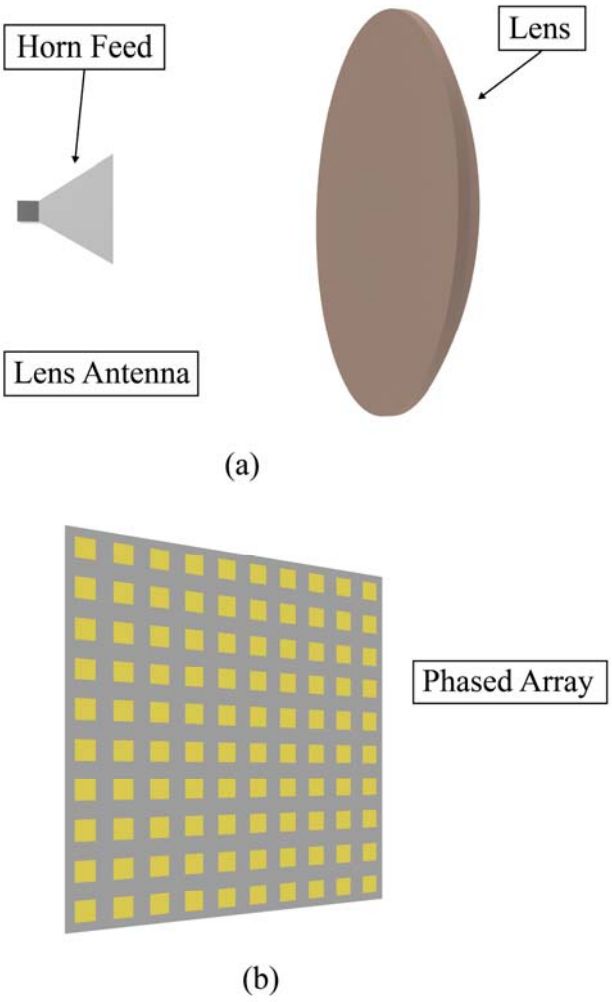

Figure 1-2 Antennas related to transmitarray antennas (a) Lens antenna; (b) Phased array

Due to the versatile advantages provided, transmitarray antennas show considerable potentials in many applications such as [1, 2]:

1) Earth remote sensing;
2) Millimeter wave and sub-millimeter wave wireless communications;
3) Broadcasting satellites;
4) THz images and sensors;
5) Solar energy concentrator.

However, before real practical implementation, the corresponding challenges of designing transmitarray antennas associated with each application scenario need to be addressed first.

In broadcasting satellites, where contour or shaped radiation beams are required, transmitarray antennas should provide beam-shaping capability. Owing to the feature of individual control of each element on the aperture of transmitarray antennas, these radiation patterns can be synthesized. A transmitarray antenna with contour radiation beam has been demonstrated [3] by deploying a four-layer transmitarray element with 360° transmission phase range and using phase-only synthesis method. Alternating projection method [4, 5] was used to iteratively obtain the required transmission phase mask on the aperture. Besides, a quad-beam transmitarray antenna has been designed [6] with a quad-layer phasing element. Particle swarm optimization technique [7, 8] was implemented for aperture phase synthesis. Here, the techniques involved are confined to phase-only synthesis method, which means that the transmitarray elements are designed to obtain a transmission phase range of 360° with transmission magnitude maintaining to unity. Considerable challenge lies in involving both transmission amplitude and phase controls during the synthesis process. To the best of our knowledge, few works is reported [9]. Besides, the unit cell developed in [9] can only cover limited transmission coefficient range, leading to incomplete control of EM waves and beam-shaping capability.

In some certain application scenarios, such as interferometric synthetic aperture radar [10], simultaneous indoor and outdoor communications, and tunnel

communications [11, 12], high-gain bidirectional antennas are required, leading to challenges in designing transmitarray antennas with forward and backward beams or transmit-reflect-combined-array antennas. An anisotropic-metasurface-based high-gain bidirectional antenna has been demonstrated [13] with advantages of being ultrathin, lightweight, and low-cost. $360°$ phase coverage was achieved by exploiting the cross-polarized component of the element. Besides, polarization-dependent multifunctional microstrip array has been reported [14] to simultaneously realize reflection and transmission. By introducing multi-layer element, the functionalities of reflection and transmission can be controlled independently. Moreover, a frequency selective surface-backed phase-shifting surface with multimode operation has been presented [15]. The functionalities of transmitarray and reflectarray can be achieved independently by discriminating in operation frequency. Although bidirectional capabilities are all obtained in these works, considerable challenges lie in improving the aperture efficiency of these antennas.

Transmitarray antennas suffer from their narrow bandwidth inherently. Various efforts have been paid to enhance the bandwidth of transmitarray antennas. The potential solutions can be divided into two aspects. One involves transmitarray element design [16-28]. Particularly, transmitarray elements based on multi-order spatial filters have been realized in [17, 20, 24, 28]. True-time-delay transmitarray elements have been demonstrated [18, 19, 21, 25] to overcome the differential spatial phase delay resulting from the different lengths from the source feed to each element on the aperture. Sub-wavelength transmitarray elements have been developed in [16, 18, 26]. The other one is based on the optimization of the transmission phase distribution on the aperture [29-31]. The algorithms are usually based on optimizing the reference phase or/and weight at each frequency point to balance the antenna system gain behavior.

The design of beam-steering transmitarray antennas is also a challenging field. The techniques that have been reported are concluded as: microstrip patches-based reconfigurability [32-39], tunable metamaterials-based reconfigurability [40-42], and frequency selective surfaces-based reconfigurability [43-48].

1.2 Research Motivations and Novelties

For being one of the most prominent types of high gain antennas, transmitarray antennas have attract considerable attentions in recent years. This work covers several major topics required to be tackled and investigated on transmitarray antennas with enhanced performance and expanded functionalities.

Firstly, transmitarray antenna with a shaped radiation pattern is important for some practical applications. Most of the previous research focus on phase-only synthesis, which means that only transmission phase is controlled. However, for complete manipulations of electromagnetic waves, both amplitude and phase controls with full coverage are required. It is emergent to involve complete amplitude and phase controls during the transmitarray synthesis. Therefore, an amplitude-phase synthesis method, that is composed of transmitarray element design and transmitarray synthesis, is developed to involve complete transmission coefficient control for designing transmitarray antennas with an expected shaped radiation beam. In the process of the element design, inspired from the element used in [30], a three-layer transmitarray element with shaped-dipole structure in the middle layer sandwiched by two orthogonal grid polarizers is developed and investigated. By turning the dimensions of the shaped-dipole structure in the middle layer, the developed transmitarray element achieves full-coverage of complex transmission coefficient, which is rarely reported before in the field of transmitarray element. In the process of transmitarray synthesis, a synthesis method based on particle swarm optimization algorithm is developed for optimizing the element distribution on the transmitarray aperture. Transmission amplitude control is taken into consideration during the synthesis process, which is rarely reported before in transmitarray synthesis. A transmitarray antenna with a flat-top radiation pattern is then designed, fabricated and tested to verify the effectiveness of the developed synthesis method. In addition, the conventional phase-only synthesis method is also implemented for validation and comparison purpose, which is realized by enforcing the transmission

amplitude of each element to unity. Compared with the conventional phase-only synthesis method, the developed amplitude-phase synthesis method offers feature of flexible beam-shaping capability.

Based on these researches, it has been shown that with fixed transmitarray aperture size, the beam-shaping capability is limited by only allowing phase control. Transmission amplitude control is required for complicated shaped beam, especially with limited aperture size. A realistic approach to achieve transmission amplitude control is based on attenuating the transmitted waves.

Secondly, in order to enhance the efficiency of the transmit-reflect-combined-array antenna, which is required in some certain applications as presented in the previous section, a novel unit cell is proposed. By adding one more bowtie layer in front of the element in chapter 3 and optimizing the element geometric parameters, the proposed four-layer element has the features of simultaneous and decoupled control of transmission phase and reflection phase, and same polarization of transmitted and reflected waves. Besides, the element demonstrates stable responses under oblique incidence, which is vital for the antenna efficiency. To verify the effectiveness of the proposed element, a single-feed transmit-reflect-combined-array antenna is designed, fabricated, and tested, and expected forward and backward beams are obtained. Moreover, by slanting the source feed, simultaneously bidirectional capability of the antenna is achieved.

Compared with the previous studies, the aperture efficiency of the transmit-reflect-combined-array antenna is effectively improved based on the proposed element. Besides, the amplitudes of the forward and backward beams can be dynamically controlled by simply slanting the source feed.

Thirdly, although improved bandwidth is obtained in previous studies, they usually involve either complicated element structure [18, 25] or sophisticated optimization process [30, 31], leading to considerable design complexity and high fabrication cost. Therefore, in order to realize wideband transmitarray antennas in a low-cost and reduced-complexity manner, an efficient approach is proposed. The design approach

combines two different techniques—1-bit phase quantization and phase distribution optimization. First, a three-layer polarization-rotation 1-bit unit cell with multiple $45°$-positioned parallel strip lines printed in the middle layer is designed, and extremely wide 1-dB element bandwidth is obtained. Here, the 1-bit element is used to introduce phase error. It is the first time that phase error is used to design wideband transmitarray antennas. Then, considering the element performance, the phase distribution at multiple frequency points is optimized with modified weight at each frequency point to further balance the gain curve. To verify the effectiveness of the proposed approach, a 13×17-element transmitarray antenna working at 10 GHz is designed, fabricated, and tested. 1-dB fractional gain bandwidth of 37% is achieved.

Although the obtained bandwidth is not the best compared with the existing designs, the proposed design approach can well balance the bandwidth behavior and system design complexity. Considering the low-cost fabrication and reduced-complexity of the system design, the proposed approach is a valid alternative for designing wideband transmitarray antennas.

1.3 Outlines of this Dissertation

This dissertation is divided into 6 chapters.

In Chapter 2, theory and analysis methods of transmitarray antennas are presented. Transmitarray elements with Fabry-Pérot-like cavity are discussed in detail. Particular emphasis is focused on the general operation principle. The generalized scattering matrix-based approach for efficiently evaluating the performance of layered element is presented. Array factor-based method for computing the radiation pattern of transmitarray antennas is described.

Chapter 3 presents the design of transmitarray antenna with complete amplitude and phase controls for beam shaping. The developed amplitude-phase synthesis method is presented. A $6.5\lambda_0 \times 6.5\lambda_0$ transmitarray antenna with a flat-top radiation beam is

designed and synthesized. The effectiveness of the amplitude-phase synthesis method is numerically and experimentally demonstrated.

In Chapter 4, the developed transmit-reflect-combined-array antenna is presented. The proposed four-layer polarization-dependent multifunctional unit cell is widely investigated. Based on the element, a $6.5\lambda_0 \times 6.5\lambda_0$ single-feed transmit-reflect-combined-array antenna prototype is designed, fabricated, and tested. At last, the simultaneously bidirectional capability of the antenna is experimentally demonstrated.

Chapter 5 presents the design of wideband 1-bit transmitarray antenna system. The developed design approach is first described in detail. A $6.5\lambda_0 \times 8.5\lambda_0$ transmitarray prototype is then designed, fabricated, and tested. Numerical and experimental results demonstrate the effectiveness of the proposed design approach.

Chapter 6 concludes this dissertation.

The structure of this dissertation is given in Figure 1-3. Although the chapters 3 to 5 are in parallel, they are related to each other. All the transmitarray elements in chapters 3 to 5 involve two orthogonal grid polarizers and are based on Fabry-Pérot-like cavity, which is discussed in chapter 2. Besides, the element in chapter 4 is introduced from the element in chapter 3.

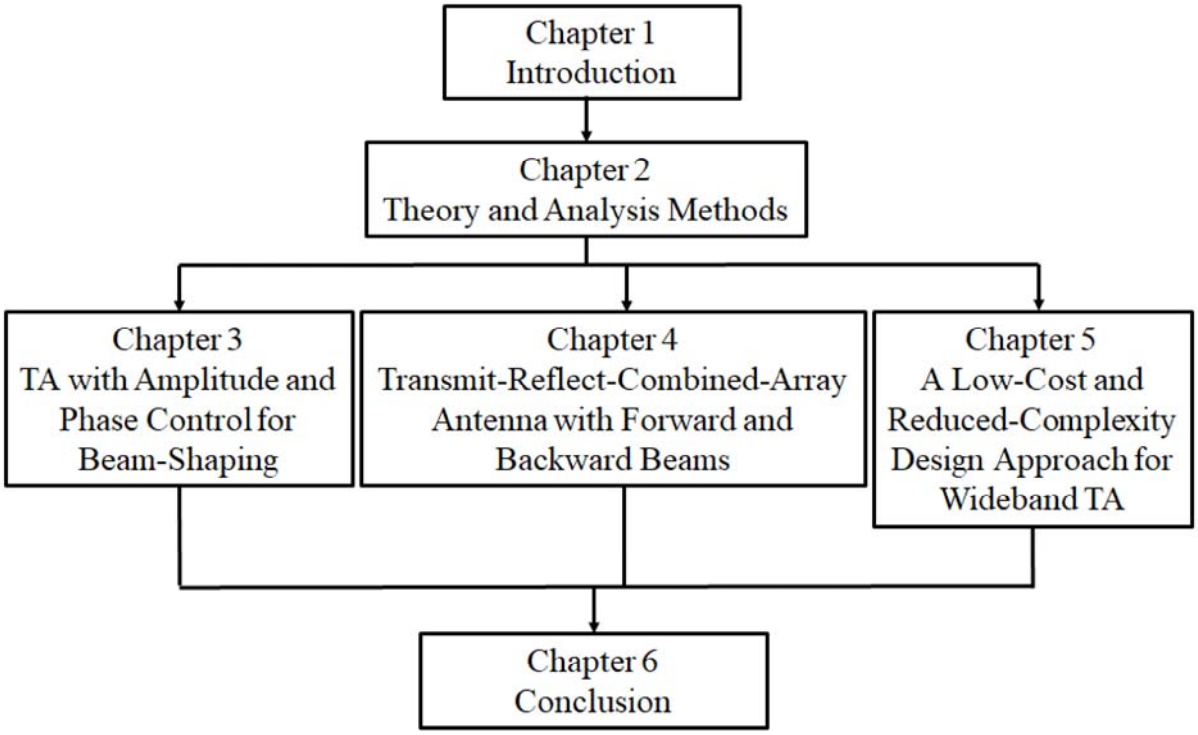

Figure 1-3 Structure of this dissertation.

Chapter 2

Theory and Analysis Methods

In this chapter, the general theory and analysis methods for transmitarray antennas are presented, with a focus on those used in this dissertation. First the source feed is discussed. Specifically, the source feed used in this dissertation, namely fermi antenna [49-56], is described. Then, the design and analysis of the transmitarray element are separately presented. Transmitarray elements with Fabry-Pérot-like cavity [30, 31, 57-59] are discussed, with a focus on the underlying operation principle. Generalized scattering matrix (GSM)-based approach [60-63] for analyzing layered element is presented in detail in the following. The accuracy and evaluation time of the GSM-based approach are presented. Next, transmitarray element arrangement corresponding to the required aperture phase distribution is described. Finally, the radiation pattern computation based on array factor approach is presented. The comparisons between the results of array factor approach and full-wave simulation are discussed.

2.1 Source Feed in this Dissertation

Corrugated horn antennas are usually used with advantages of symmetric radiation patterns and excellent antenna efficiency to illuminate the transmitarray aperture. However, here, a fermi antenna [49-56] is introduced, providing advantages of being light-weight and low-profile. For completeness and clarity, it is necessary to provide the performance of the source feed.

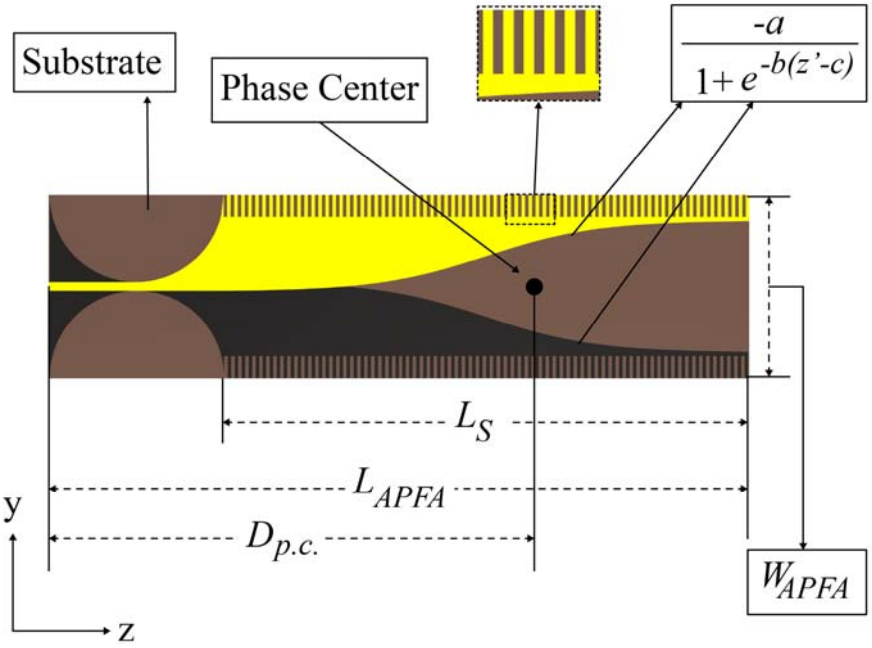

Figure 2-1 Source feed schematic view.

The schematic view of the source feed is shown in Figure 2-1. Each side of the substrate ($\epsilon_r = 3.3,\ \tan\delta = 0.001,\ \text{thickness} = 0.8\ \text{mm}$) is printed with a metal slot. The curve of the slot satisfies the Fermi-Dirac function shown below:

$$f(z') = \frac{-a}{1 + e^{-b\cdot(z'-c)}} \tag{2-1}$$

where a, b, and c are related to the asymptotic value, gradient at inflection point, and inflection point coordinate, respectively. The detailed design parameters are listed in Table 2-1.

The comprehensive performances of the source feed are summarized in Figure 2-

TABLE 2-1
DESIGN PARAMETERS OF THE SOURCE FEED

a	16
b	0.083
c	60
Ls	120 mm
L_{APFA}	160 mm
W_{APFA}	42 mm

2. Asymmetric radiation patterns with narrower beamwidth in E-plane and wider beamwidth in H-plane are obtained from Figure 2-2 (b)-(d). Besides, from Figure 2-2 (e), the realized gain increases with increasing frequency. However, the total efficiency of the source feed (T.E.), which is defined as:

$$\text{T.E.} = \frac{\text{Radiated Power}}{\text{Stimulated Power}} \tag{2-2}$$

shows a decreasing curve. In addition, the phase center response of the source feed is given in Figure 2-2 (f).

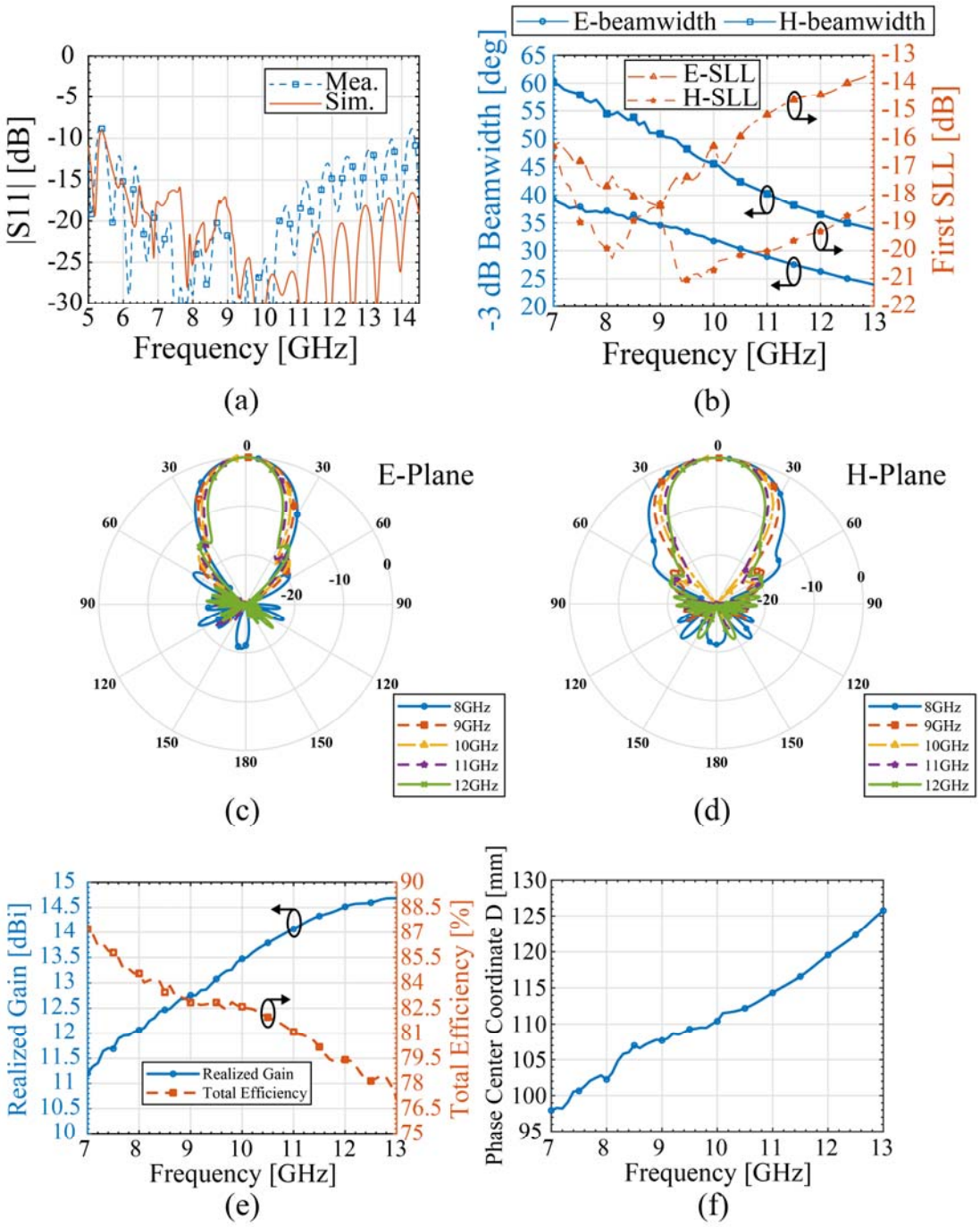

Figure 2-2 Source feed performances (a) return loss; (b) Beamwidth and First SLL; (c) normalized radiation patterns in E-plane; (d) normalized radiation patterns in H-plane; (e) Realized gain and total efficiency; (f) Phase center coordinate response.

2.2 Design and Analysis of the Transmitarray Element

There are different techniques for designing transmitarray element, such as multi-layer frequency selective surfaces (M-FSSs) [17, 23, 64], receiver-transmitter design [39, 65-67]. M-FSSs are used as spatial phase shifters. Studies have found that single layer of FSS cannot provide full coverage of compensation phase [68]. Instead, layered structure of FSS separated by either thick substrate or air gap is required [47]. Besides, a receiver-transmitter configuration typically consists of two planar arrays named receiver/transmitter array and the interconnected phase delay lines. The incident fields captured by the receiver array re-radiate into free space by transmitter array after passing through the phase delay lines, which are mainly composed of coupling structure and/or transmission line. However, in this chapter, particular focus is placed on the transmitarray element with Fabry-Pérot-like Cavity [30, 31, 57-59], which can be physically explained by interference theory [69-71]. Due to the flexibility provided, all the transmitarray elements in this dissertation are developed based on this kind. Therefore, it is necessary to provide the underlying operation principle of such kind of element. Next is to analyze the performance of the element. Due to the multi-layer nature of such kind of elements, generalized scattering matrix (GSM)-based approach [60-63] is used to efficiently evaluate the element performance. These two aspects are separately discussed in the following.

2.2.1 Transmitarray Element with Fabry-Pérot-like Cavity

The concept of Fabry-Pérot-like cavity is from Fabry-Pérot interferometer [72, 73], which is an optical cavity made from a pair of partially reflective surfaces allowing interference of all the partially transmitted waves. For transmitarray element, under some certain conditions, such as thick substrate layer or thick air layer between adjacent layers [30, 31, 58], the combined element can be treated as a Fabry-Pérot-like cavity,

and the element behavior can be explained by using interference theory [69-71].

Figure 2-3 shows the 3-D perspective view of a typical transmitarray element with Fabry-Pérot-like cavity. One should be mentioned that although only one element is illustrated, the element performance is in fact obtained in a periodically infinite array environment. The cross-section view of the element is shown in Figure 2-4. With y-polarized normal incidence, the waves directly pass through the first layer. After passing the air layer, the waves interact with the second layer, consequently resulting in y-polarized reflected waves ($E_{r,1}^{y}$), x-polarized reflected waves ($E_{r,1}^{x}$), y-polarized transmitted waves ($E_{t,1}^{y}$), and x-polarized transmitted waves ($E_{t,1}^{x}$). Here, the number 1 in the subscript is the interaction round number. Considering the grid orientation of the

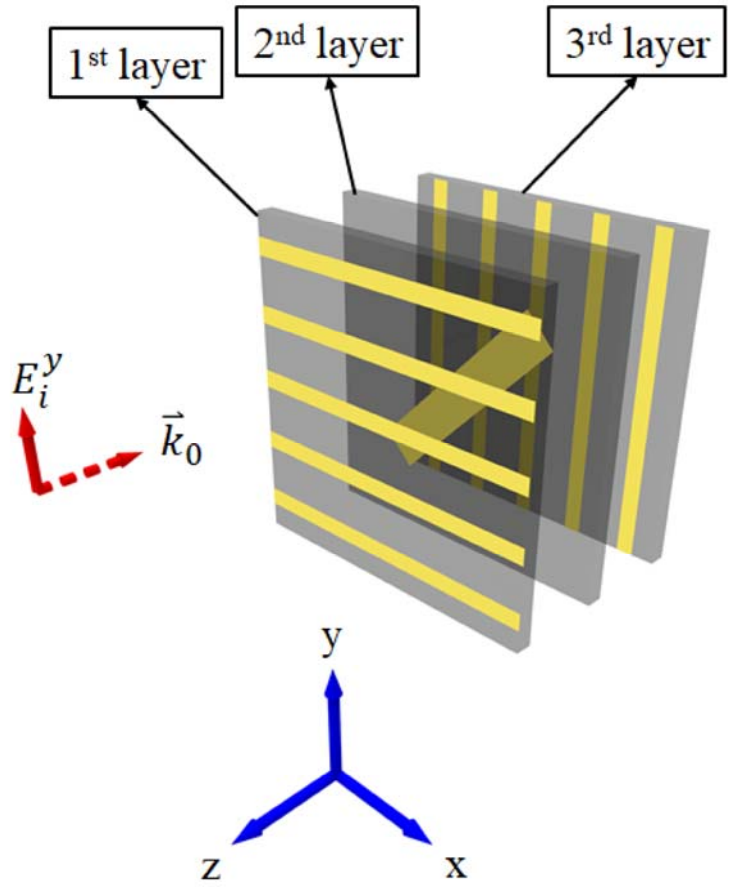

Figure 2-3 3D perspective view of transmitarray element with Fabry-Pérot-like cavity. The air gaps between adjacent layers is 4 mm. The periodicity is 15 mm.

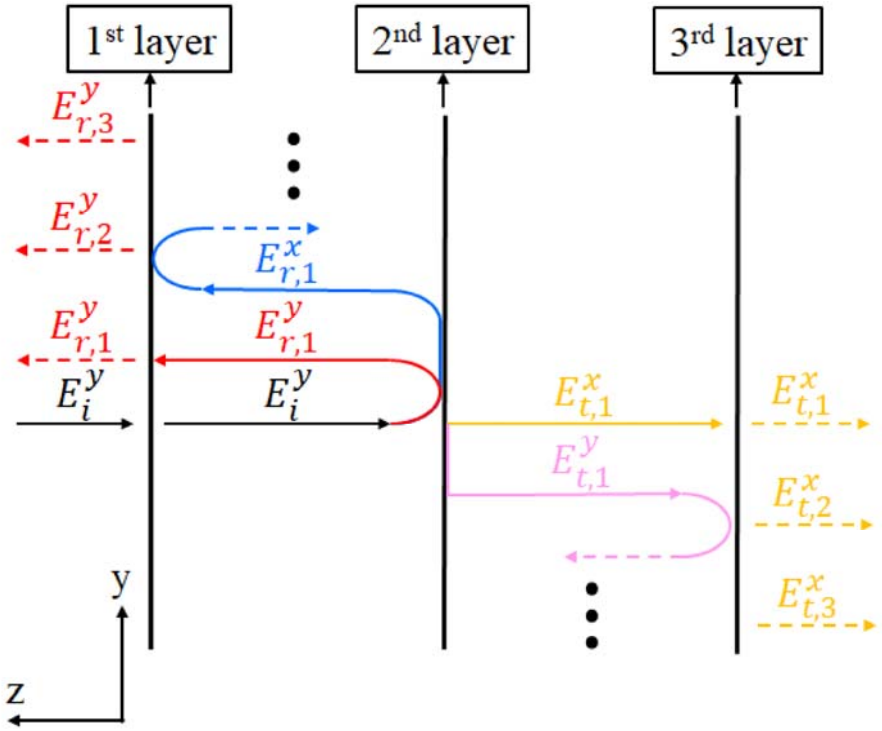

Figure 2-4 Cross section view of the element shown in Figure 2-3.

two polarizers, as the red solid line and yellow solid line indicate in Figure 2-4, the y-polarized reflected waves ($E^y_{r,1}$) pass through the first layer to the outside, while the x-polarized transmitted waves ($E^x_{t,1}$) pass through the third layer to the outside. However, as the blue lines and pink lines indicate in Figure 2-4, the x-polarized reflected waves ($E^x_{r,1}$) and y-polarized transmitted waves ($E^y_{t,1}$) are reflected back to the second layer. These back-reflected waves further interact with the second layer, leading to second round and third round y-polarized reflected waves ($E^y_{r,2}$, $E^y_{r,3}$) and x-polarized transmitted waves ($E^x_{t,2}$, $E^x_{t,3}$). These waves will interfere with each other. Similar to the wave propagation in a stratified media [74, 75], the overall reflected and transmitted waves of the element are then the superposition of these multiple reflected and transmitted waves. Mathematically, they are described as:

$$E_r^{overall} = E^y_{r,1} + E^y_{r,2} + E^y_{r,3} + \cdots \tag{2-3}$$

$$E_t^{overall} = E_{t,1}^x + E_{t,2}^x + E_{t,3}^x + \cdots \tag{2-4}$$

Each component can be obtained by using transmission line model once the individual behavior of each layer is known, which is usually obtained by full-wave simulation. Then, the overall reflection coefficient and transmission coefficient are computed by using the formulas shown below:

$$R_{overall} = \frac{E_r^{overall}}{E_i^y} \tag{2-5}$$

$$T_{overall} = \frac{E_t^{overall}}{E_i^y} \tag{2-6}$$

2.2.2 Generalized Scattering Matrix-Based Analysis Method

The analysis technique for multilayer transmitarray elements, such as those based on Fabry-Pérot-like cavity as shown in Figure 2-3, can be addressed, either by an overall or a modular technique. For overall method, the element responses are evaluated by periodic boundary condition [76, 77]-based full-wave analysis with the entire element as a whole. However, with layered element, the number of unknows and evaluation time are exponentially increased. Instead, the modular method, as presented in [60-63], is based on the computation of the generalized scattering matrix (GSM) for each layer. Then, the performance of the entire element can be obtained by using cascading process. Specifically, the responses of each layer (including air layer if exist) is obtained by using periodic boundary condition-based full-wave simulation and packed as a building block. Next, considering proper mode-matching between each layer, the layers are connected to form a cascaded scattering parameter network. Finally, the total responses are obtained by using simple matrix computations. The flowchart of the GSM method is shown in Figure 2-5. It should be noticed that sufficient Floquet modes need to be considered during the cascading process to obtain accurate overall

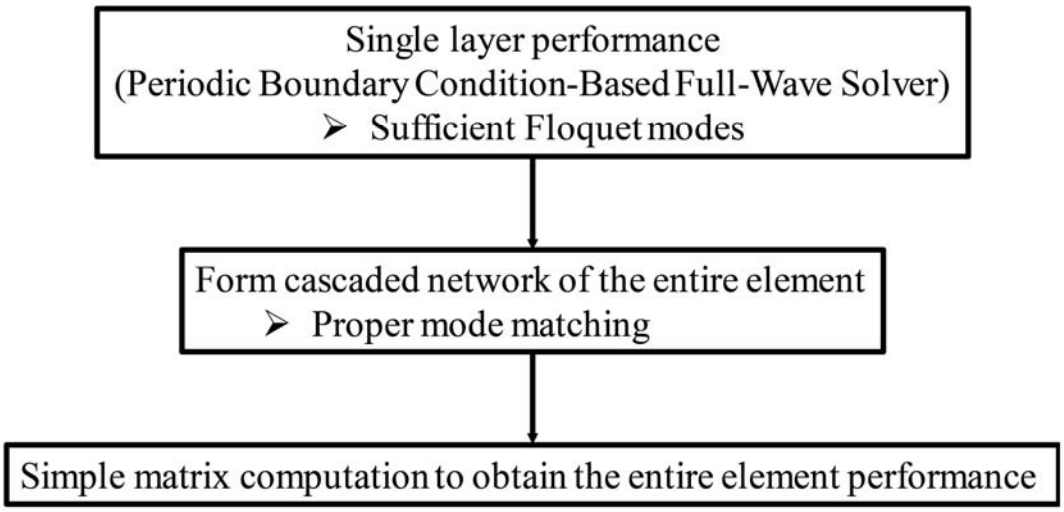

Figure 2-5 Flowchart of the GSM method.

performance, especially for transmitarray element with a small separation between adjacent layers. However, for transmitarray elements with Fabry-Pérot-like cavity, where the separation between two adjacent layers is usually large, only fundamental Floquet modes are enough to obtain accurate results.

To verify the effectiveness, the transmitarray element shown in Figure 2-3 is evaluated by both GSM approach and overall method under normal incidence. For GSM approach, only the two fundamental Floquet modes are taken into account during the cascading process. Therefore, as shown in Figure 2-6, the element is equivalent to a 4-port network with 5 building blocks representing each layer. Here, the port superscripts denote the polarization, and the subscripts represent the reflection or transmission side. The performance of the element can be fully characterized by two matrix equations shown in the following:

$$\begin{pmatrix} E_t^x \\ E_t^y \end{pmatrix} = \overline{\overline{\boldsymbol{T}}} \cdot \begin{pmatrix} E_i^x \\ E_i^y \end{pmatrix} \tag{2-7}$$

$$\begin{pmatrix} E_r^x \\ E_r^y \end{pmatrix} = \overline{\overline{\boldsymbol{R}}} \cdot \begin{pmatrix} E_i^x \\ E_i^y \end{pmatrix} \tag{2-8}$$

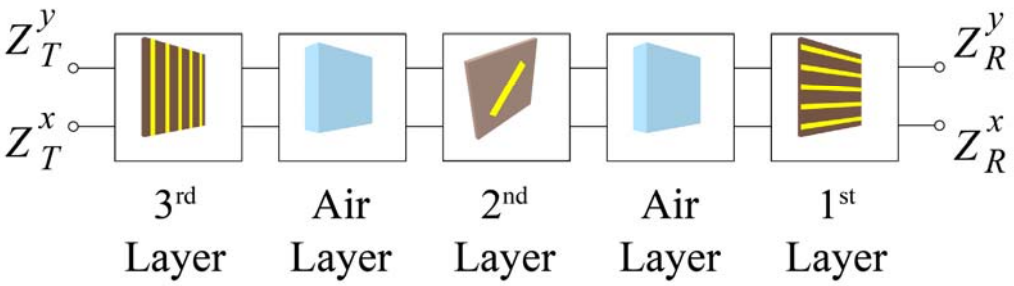

Figure 2-6 Equivalent network representation of the element shown in Figure 2-3.

$$\overline{\overline{\boldsymbol{T}}} = \begin{bmatrix} T_{xx} & T_{xy} \\ T_{yx} & T_{yy} \end{bmatrix} \tag{2-9}$$

$$\overline{\overline{\boldsymbol{R}}} = \begin{bmatrix} R_{xx} & R_{xy} \\ R_{yx} & R_{yy} \end{bmatrix} \tag{2-10}$$

where $E_{i/r/t}^{x/y}$ represents the incident/reflected/transmitted fields for the element with x or y polarizations. The complex matrices $\overline{\overline{T}}$ and $\overline{\overline{R}}$ describe the transmission and reflection performance of the element. Here, the first letter of the subscript denotes the polarization of transmitted or reflected fields, along with the second letter for that of incident fields. Figure 2-7 shows the comparisons between the results of GSM approach and overall method. The results show high consistency, demonstrating the high accuracy of the GSM approach with only the two fundamental Floquet modes taken into consideration. To further demonstrate the applicable conditions of GSM method with only fundamental Floquet modes taken into account, another two sets of simulation results are given in Figure 2-8. The insets are the evaluated element model, and the only difference between the two element models is the thickness of the air gap between adjacent layers. For element shown in Figure 2-8 (a), the air gap is 4 mm, while that of the element shown in Figure 2-8 (b) is 2 mm. No matter how many modes are considered, for 4 mm air gap element, the results show high consistency. However, for

2 mm air gap element, accurate results can only be obtained with high-order Floquet modes taken into consideration. Besides, for first high-order mode appeared in these elements, which is surface wave mode, the propagation loss through 4 mm air gap is 12.6 dB at 10 GHz. It is this large propagation loss of the first high-order mode enables the GSM method with only fundamental modes obtain accurate results. However, for 2 mm air gap, the propagation loss of the first high-order mode is only 6.3 dB at 10 GHz, which is too small to ignore. Therefore, the critical condition that obtain accurate results under consideration of only fundamental Floquet modes is the air gap thickness of the element. Besides, the GSM approach provides 10-times fast evaluation time compared with overall method. The high efficiency and accuracy of the GSM approach make it possible to perform parametric studies and optimize the element geometry within an acceptable time.

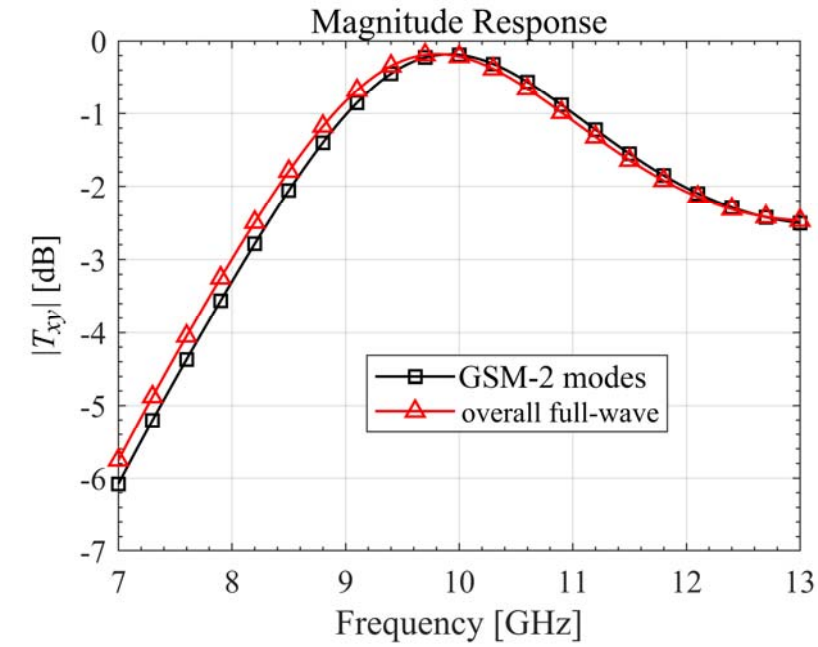

(a)

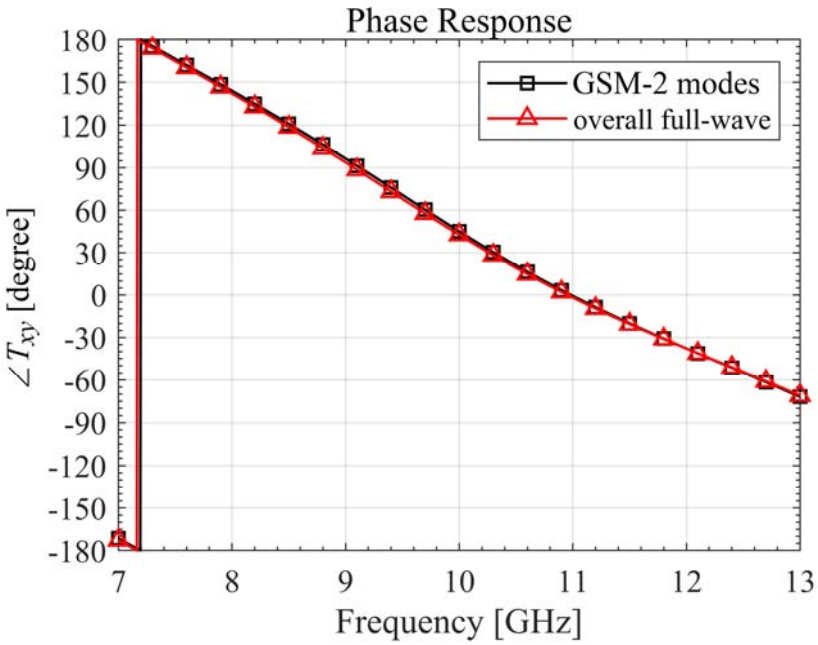

(b)

Figure 2-7 Comparison results of (a) magnitude response; (b) phase response.

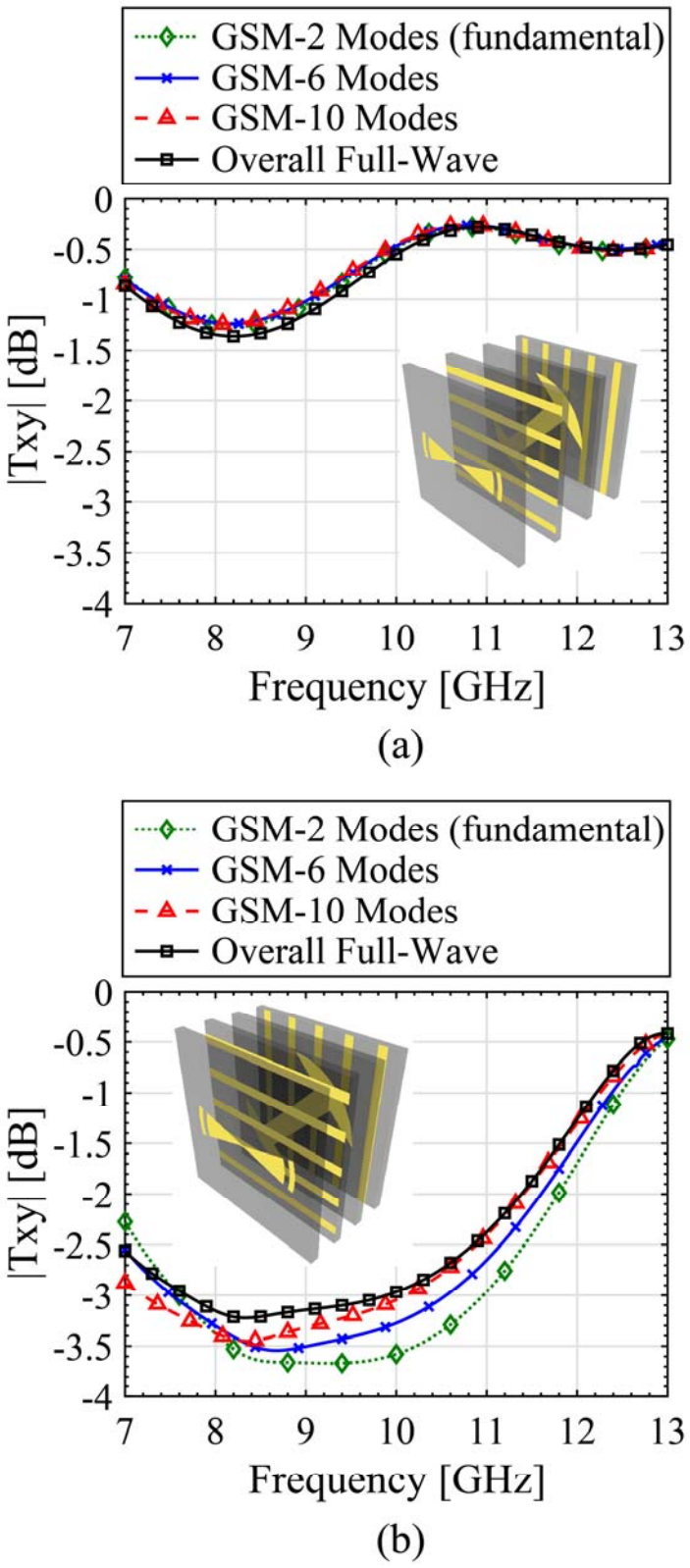

Figure 2-8 Comparison results of (a) 4 mm air gap element; (b) 2 mm air gap element. Insets: element model. The periodicity of the element is 15 mm.

2.3 Phase Distribution and Element Arrangement on Transmitarray Aperture

The operation mechanism of transmitarray antennas is based on assuming that the transmitarray elements are located in the far-field region of the source feed, which is usually center positioned. In such situation, the EM field impinging on each transmitarray element on the aperture can be locally considered as a plane wave with a certain incident angle and a certain incident phase.

Each transmitarray element on the aperture need to be designed to recompense the spatial phase delay that is proportional to the length from the source feed to the element plus a progressive phase term to generate a collimated beam in desired direction, as shown in Figure 2-9.

Mathematically, the required phase ϕ_{mn} for the mnth element is described

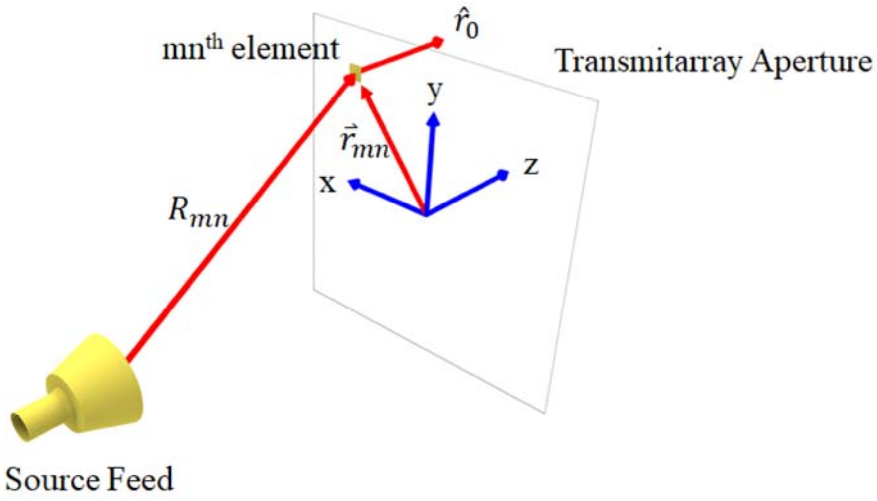

Figure 2-9 mnth element compensation phase.

as [62, 78]:

$$\phi_{mn} = k_0 \cdot (R_{mn} - \vec{r}_{mn} \cdot \hat{r}_0) + \psi_0 \tag{2-11}$$

where k_0 is the propagation constant in free-space, R_{mn} is the length from the source feed to the mnth element, $\vec{r}_{mn}$ is the position vector of the mnth element, and $\hat{r}_0$ represents the main beam direction. For broadside beam, the equation can be simplified as:

$$\phi_{mn}^{broadside} = k_0 \cdot R_{mn} + \psi_0 \tag{2-12}$$

ψ_0 is the constant reference phase, revealing that a relative transmission phase distribution rather than the absolute transmission phase distribution is enough for transmitarray design.

Figure 2-10 shows the required transmission phase distribution on the aperture of a 30×30-element transmitarray antenna ($F/D = 0.8,\ P = \frac{\lambda_0}{2}$). The source feed is center-positioned, and the beam is broadside.

Once the required transmission phase distribution is determined, the associated transmitarray element dimension distribution is given by referring to the transmission phase diagram obtained in the previous section.

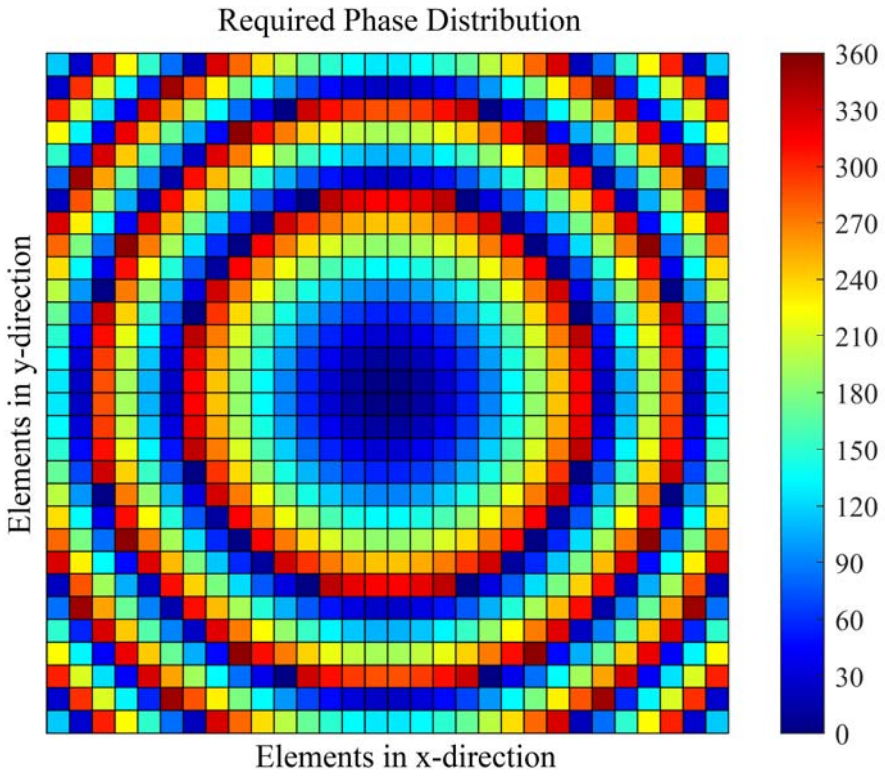

Figure 2-10 Required compensation phase distribution on the aperture.

2.4 Radiation Pattern Calculation using Array Factor Approach

Exact radiation pattern of a transmitarray antenna can be obtained by using aperture field integration [79]. However, the exact aperture field distribution is difficult to obtain as the adjacent transmitarray elements are slightly different, and the formulation of the integration is usually hard. Instead, the far-field radiation pattern can be efficiently computed by using conventional array theory with certain approximations introduced during the formulation. Mathematically, the radiation pattern of a $M \times N$-

element planar array is described as [78, 80]:

$$\vec{E}(\hat{u}) = \sum_{M}\sum_{N} \overline{\overline{A}}_{mn}(\hat{u}) \cdot \vec{I}(\vec{r}_{mn}) \tag{2-13}$$

where $\overline{\overline{A}}_{mn}(\hat{u})$ is the vector function of the element pattern, $\vec{r}_{mn}$ is the position vector of the mnth element, $\vec{I}(\vec{r}_{mn})$ is the element excitation vector function for mnth element, and $\hat{u} = \hat{x}\sin\theta\cos\varphi + \hat{y}\sin\theta\sin\varphi + \hat{z}\cos\theta$ represents the observation direction. A transmitarray antenna system is given in Figure 2-11. The source feed is center-positioned with a distance to the transmitarray aperture of $|\vec{r}_f|$.

To simplify the formulations, scalar cosine q models are usually introduced to approximate the element-pattern function and source feed pattern function. For element-pattern function, it is described as:

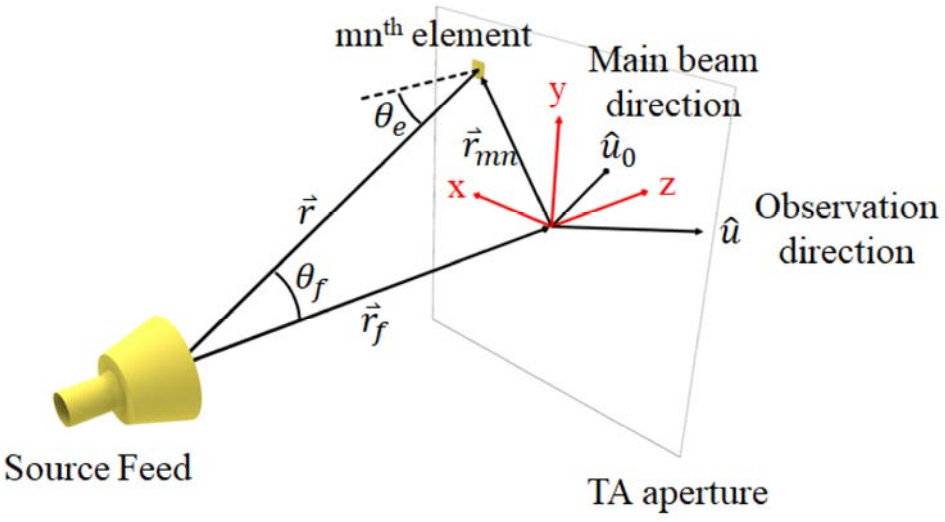

Figure 2-11 Transmitarray antenna system.

$$A_{mn}(\theta,\varphi) \approx \cos^{q_e}(\theta) \cdot e^{j \cdot k_0 \cdot (\vec{r}_{mn} \cdot \hat{u})} \tag{2-14}$$

where q_e represents the power factor of the element pattern. It is usually obtained by using full-wave simulation of the element with infinite array approximation. By approximating the source feed with another cosine q model and taking the Euclidian distance between the source feed and the transmitarray element into consideration, the element excitation function can then be described as [78, 80]:

$$I(m,n) \approx \frac{\cos^{q_f}(\theta_f^{mn})}{\left|\vec{r}_{mn} + \vec{r}_f\right|} \cdot e^{-j \cdot k_0 \cdot \left|\vec{r}_{mn} + \vec{r}_f\right|} \cdot \cos^{q_e}(\theta_e^{mn}) \cdot e^{j \cdot \psi_{mn}} \tag{2-15}$$

where θ_f^{mn} is the spherical angle in the feed's coordinate system for mnth element, q_f is the power factor of the source feed, $\vec{r}_f$ is the source feed position vector, θ_e^{mn} is the angle between the line from source feed to the mnth element $\left|\vec{r}\right|$ and the normal direction of the aperture plane, ψ_{mn} is the required compensation phase for the mnth element to form a collimated main beam in the $\hat{u}_0$ direction, as presented in equation 2-11.

The mutual coupling between adjacent elements is approximated by using the infinite periodic array approach, which means that each element is located in an infinite array environment with all surrounding elements considered identical.

Based on the above analysis, the radiation pattern presented in equation 2-13 can now be expressed to the scalar form as [78, 80]:

$$E(\theta,\varphi) = \sum_M \sum_N \cos^{q_e}(\theta) \cdot \frac{\cos^{q_f}(\theta_f^{mn})}{\left|\vec{r}_{mn} + \vec{r}_f\right|} \cdot e^{-j \cdot k_0 \cdot \left(\left|\vec{r}_{mn} + \vec{r}_f\right| - \vec{r}_{mn} \cdot \hat{u}\right)} \cdot \cos^{q_e}(\theta_e^{mn}) \cdot e^{j \cdot \psi_{mn}} \tag{2-16}$$

TABLE 2-2
TRANSMITARRAY ANTENNA SETTINGS

Element Periodicity	15 mm ($0.5\lambda_0$@10 GHz)
Aperture Size	375 mm × 375 mm (25 × 25-element)
Source Feed	Corrugated horn (15dBi@10 GHz)
F/D	0.9
Main Beam Direction	$(\theta, \varphi) = (20°, 0°)$

It should be noticed that the incident field distribution can also be alternatively obtained by either full-wave simulation or measurement. Besides, equation 2-16 can only be applied to compute the co-polarized radiation pattern of a transmitarray antenna. The calculation can further be accelerated by using Fast Fourier Transform algorithm to evaluate the double summation in equation 2-16.

The radiation pattern of a 25×25-element transmitarray antenna is computed by both array factor-based approach and full-wave simulation. The detailed transmitarray antenna settings are listed in Table 2-2. For array factor approach, the element power factor is set to 1, and the incident field distribution on the transmitarray aperture is obtained by full-wave simulation rather than cosine q model. For full-wave simulation, the source feed is equivalent to a field source instead of the real modeling. Figure 2-12 shows the comparisons between the results of both methods in $\varphi = 0°$ plane. The main beam shape and direction, beamwidth, and the SLL in beam region can be accurately computed by array factor approach. The discrepancies outside the main beam region is mainly due to that exact interelement mutual coupling and edge diffraction are not considered in the array factor approach formulation. The evaluation time for both methods are also summarized in Table 2-3. The fast evaluation provided by the array factor approach is helpful for array synthesis applications, and the array factor approach is used in Chapter 3.

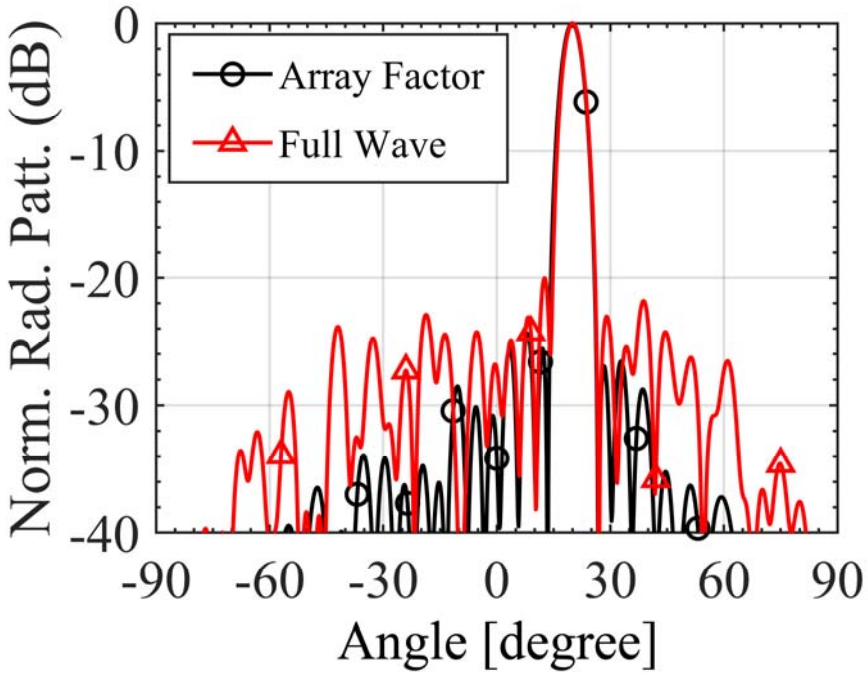

Figure 2-12 Comparison results between both methods in $\varphi = 0°$ plane.

TABLE 2-3
EVALUATION TIME COMPARISON

Method	Evaluation time
Full-wave analysis	14024s
Array factor approach	0.5s

Chapter 3

Transmitarray Antenna with Amplitude and Phase Control for Beam-Shaping

As presented in chapter 1, beam-shaping transmitarray antenna that involves complete transmission coefficient control is emergent. In this chapter, an amplitude-phase synthesis method is developed to design transmitarray antennas with an expected shaped beam. The amplitude-phase synthesis method is composed of two parts—transmitarray element design and transmitarray synthesis. In the process of the transmitarray element design, a three-layer transmitarray element with shaped-dipole structure in the middle layer sandwiched by two orthogonal grid polarizers is developed and studied. By turning the dimensions of the shaped-dipole structure, the proposed transmitarray element achieves full-coverage of complex transmission coefficient, which is rarely reported before in the field of transmitarray element. In the process of transmitarray synthesis, a complex amplitude synthesis technique, based on particle swarm algorithm, is developed for optimizing the element distribution on the transmitarray aperture. Transmission amplitude control is considered during the synthesis process, which is rarely reported before in the field of transmitarray synthesis. To verify the effectiveness of the method, a $195\ \text{mm} \times 195\ \text{mm}$ ($6.5\lambda_0 \times 6.5\lambda_0$ @10GHz) transmitarray antenna with a flat-top radiation pattern is designed, fabricated, and tested. Besides, for comparison purpose, the conventional phase-only synthesis method is also implemented by enforcing the transmission amplitude of each element to unity. Compared with the conventional phase-only synthesis method, the developed

amplitude-phase synthesis method offers feature of flexible beam-shaping capability, and is a valid alternative to design shaped-beam transmitarray antenna with limited aperture size.

3.1 Amplitude-Phase Synthesis Method

The developed amplitude-phase synthesis method is composed of two parts. part one is to design a transmitarray element that is capable of providing full-coverage of complex transmission coefficient. Part two is to synthesize the element distribution on the aperture for required shaped radiation pattern. They are discussed separately in the following.

3.1.1 Transmitarray Element Design

Transmitarray element with both amplitude and phase control is rarely reported before. Inspired from the transmitarray element in [30], a new transmitarray element is developed. It is found that the transmitarray element is able to involve complete transmission amplitude control, which is rarely reported before. It should be pointed out that the element in [30] is mainly focused on wideband operation, while in this chapter the element is centered to the control of both amplitude and phase of the transmission coefficient. The 3-D perspective view of the element is shown in Figure 3-1 (a). Three metal layers (yellow parts) are etched on corresponding three dielectric substrates ($\varepsilon_r = 3.3,\ \tan\delta = 0.001,\ T_{sub} = 0.8\ \text{mm}$), which are separated by the same air gaps ($T_{air} = 4.0\ \text{mm}$). The top layer and bottom layers are two identical orthogonal-positioned grid polarizers with strip width of $s = 0.8\ \text{mm}$ and gap of $w = 2.2\ \text{mm}$, which work as perfect lens or reflector depending on the grid orientation. An obliquely placed (θ) shaped-dipole with radius of R_1, dipole width of w_1, and dipole length of L, is printed on the middle layer, where the detailed top view is presented in

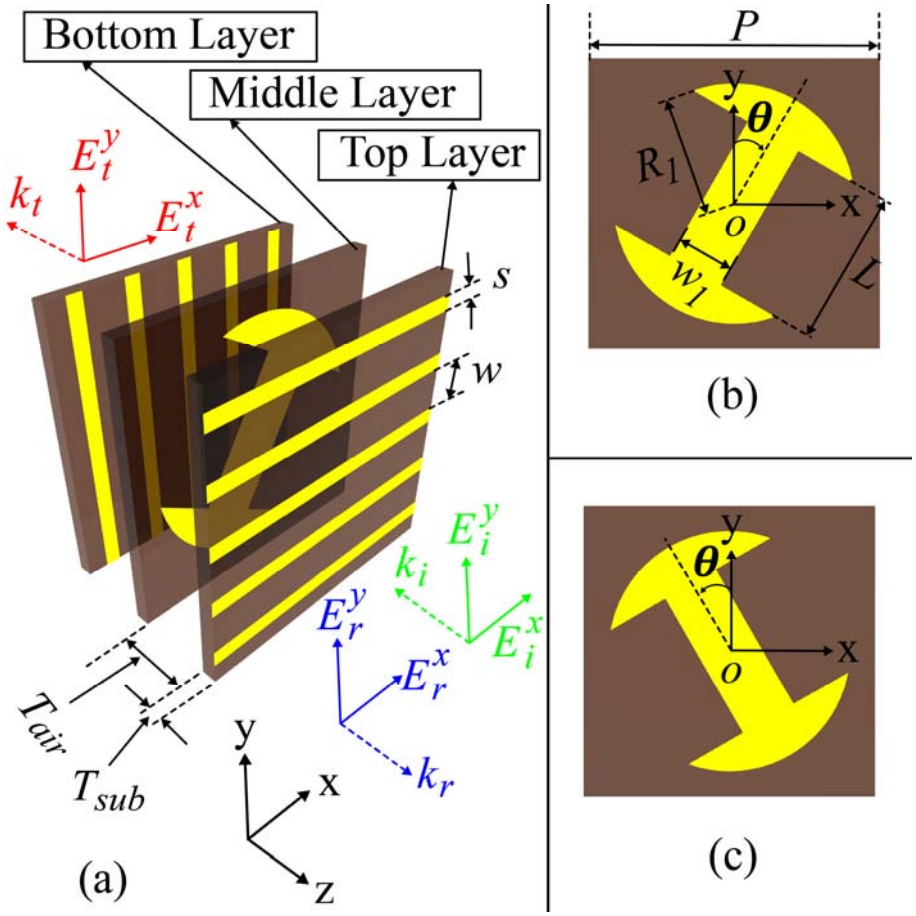

Figure 3-1 Unit cell view (a) 3-D perspective view of the unit cell; green arrows: incident field components; blue arrows: reflected field components; red arrows: transmitted field components; (b) Top view of the middle layer; (c) Top view of the mirrored middle layer.

Figure 3-1 (b). Besides, the periodicity of the element is $P = 15\,\mathrm{mm}$, which is equivalent to $0.5\lambda_0$, where λ_0 denotes the free-space wavelength at 10 GHz. The element responses highly rely on the polarization of the incident fields. Specifically, with y-polarized normal illumination (E_i^y), the combined element forms a Fabry-Pérot-like cavity [30, 31, 57-59], and can be explained by the interference theory presented in Chapter 2. By rotating the θ in the middle layer of the element, the consequent Cr-Pol transmissive (E_t^x) interference can either be constructive or destructive, leading to the manipulation of the $|E_t^x|$. It should be pointed out that the control of the

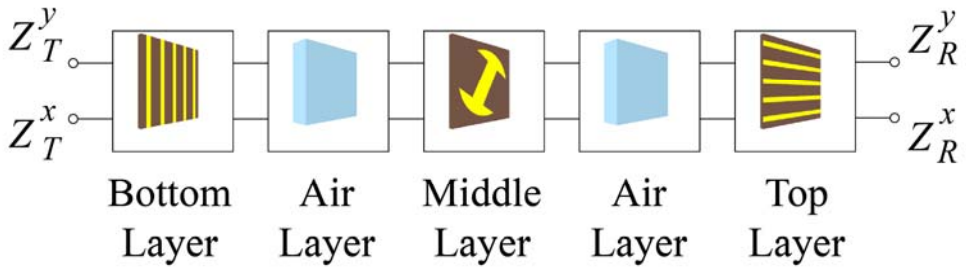

Figure 3-2 Equivalent S-parameter network representation of the element.

transmission magnitude ($|E_t^x|$) is at the cost of the reduced transmission efficiency. Considering the grid orientation of the top and bottom layers, in order to attenuate $|E_t^x|$, part of the power should be reflected by means of E_r^y. As a consequence, the resulting antenna system inevitably suffers from less efficiency, which is an evident shortcoming. However, the undesired E_r^y component is isolated on the reflection side. Meanwhile, the phase of the E_t^x component can be controlled by varying L. Besides, the fields are fully reflected by means of E_r^x with x-polarized normal incident waves (E_i^x), which means the Cr-Pol of the source feed has little effect on the transmission side.

In this chapter, generalized scattering matrix (GSM)-based approach presented in Chapter 2 is implemented for efficiently evaluating the element performance. With only the two fundamental Floquet modes taken into consideration, as shown in Figure 3-2, the element is equivalent to a 4-port network with 5 building blocks representing each layer. Besides, the element performance can be fully characterized by the two matrix equations shown in equations 2-7~2-10. Here, component of T_{xy} is of critical concern. For complete control of EM waves, the element responses should satisfy the following requirements:

1) Full-coverage of transmission phase
2) Full-coverage of transmission amplitude

After huge parametric studies and geometric optimization, the final element design parameters are listed in Table 3-1. Three discrete values of R_1 are selected to fulfill

TABLE 3-1
FINAL DESIGN PARAMETERS OF THE ELEMENT

R_1	6.5, 6.8, 7.1 mm
w_1	3.0 mm
L	1.0~12.8 mm (R_1=6.5) 1.0~13.4 mm (R_1=6.8) 1.0~14.0 mm (R_1=7.1)
θ	0°~45°

the requirements.

The T_{xy} responses vs. L at discrete θ are shown in Figure 3-3 (a) and (b). Figure 3-3 (c) and (d) present the T_{xy} responses vs. θ at discrete L. All the results in Figure 3-3 are evaluated at 10 GHz with element configuration of $R_1 = 7.1$ mm under normal incidence. It can be mainly concluded that L is in charge of phase responses, while amplitude responses are controlled by θ. Figure 3-4 depicts the $|R_{yy}|$, $|T_{yy}|$, and $|R_{xx}|$ responses with element configuration of $R_1 = 7.1$ mm and $L = 10.8$ mm under normal incidence. Compared the pentagram-marked curve in Figure 3-3 (c) with the circle-marked curve in Figure 3-4, the inverse relation between $|T_{xy}|$ and $|R_{yy}|$ can be clearly observed. In addition, high polarization purity on transmission side can be addressed by ignorable value of $|T_{yy}|$ and near-unity value of $|R_{xx}|$. Meanwhile, all the discrete results evaluated in different configurations are plotted in polar diagram shown in Figure 3-5. Full amplitude coverage and half phase coverage can be achieved directly. The other half space can be easily obtained by mirroring the middle layer, where the top view is shown in Figure 3-1 (c), consequently leading to full coverage of both transmission amplitude and transmission phase. The frequency responses in element configuration of $R_1 = 6.8$ mm under normal incidence are given in Figure 3-6 (a) and (b). Smooth amplitude responses and linear phase responses can be obtained, illustrating the potentials of wideband operation. It should be noticed that the discrete data obtained in Figure 3-5 are interpolated by cubic spline and then packed as a

numerical function, which is used directly in system design and synthesis step.

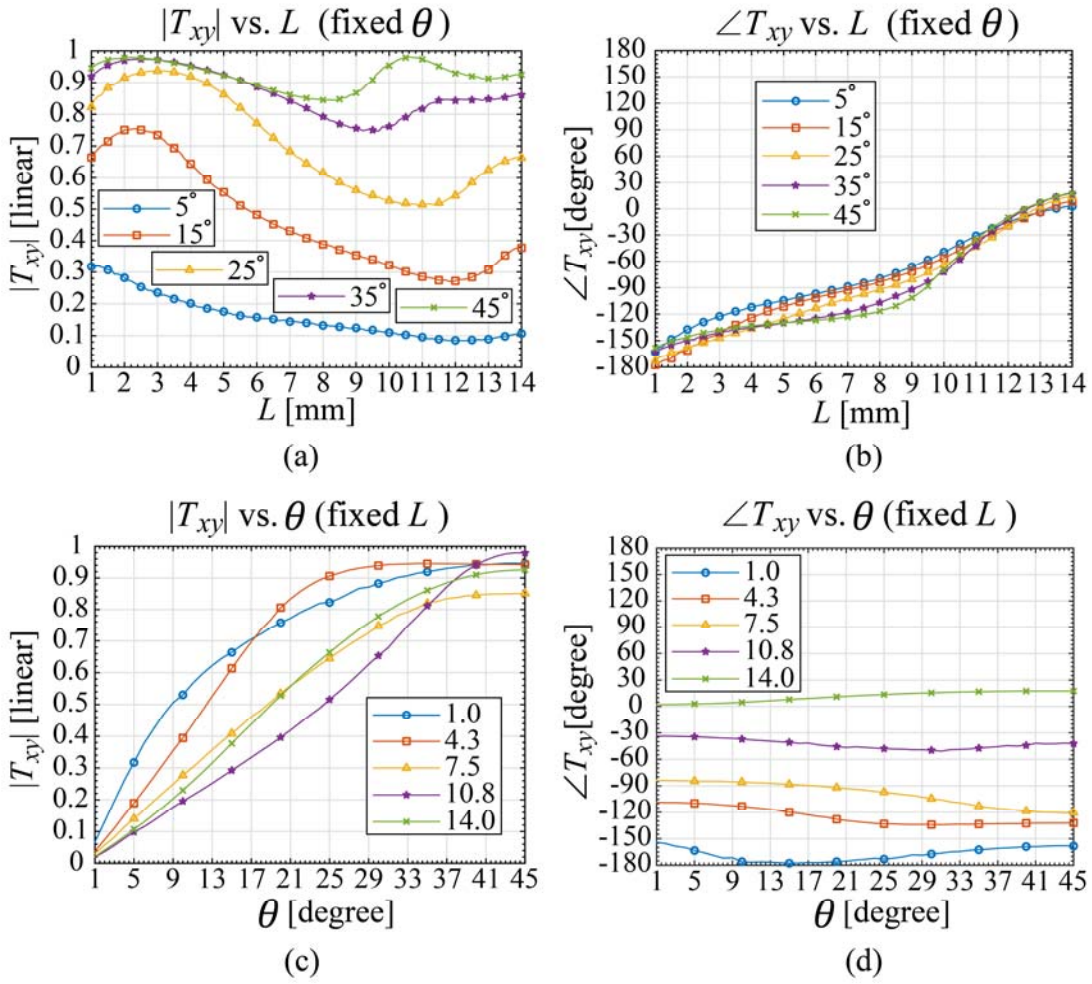

Figure 3-3 (a) $|T_{xy}|$ vs. L at discrete values of θ. (b) $\angle T_{xy}$ vs. L at discrete values of θ. (c) $|T_{xy}|$ vs. θ at discrete values of L. (d) $\angle T_{xy}$ vs. θ at discrete values of L.

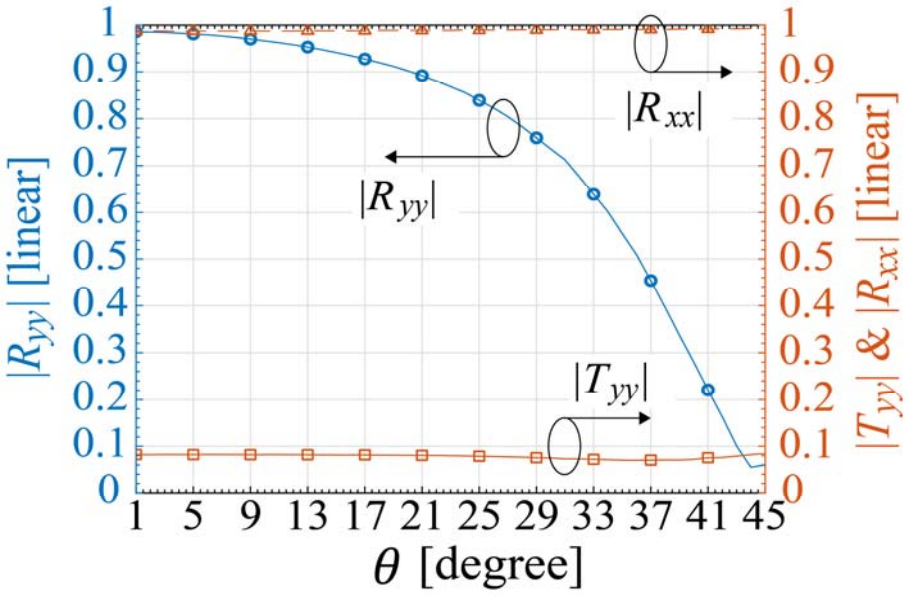

Figure 3-4 $|R_{yy}|$, $|T_{yy}|$, and $|R_{xx}|$ vs. θ.

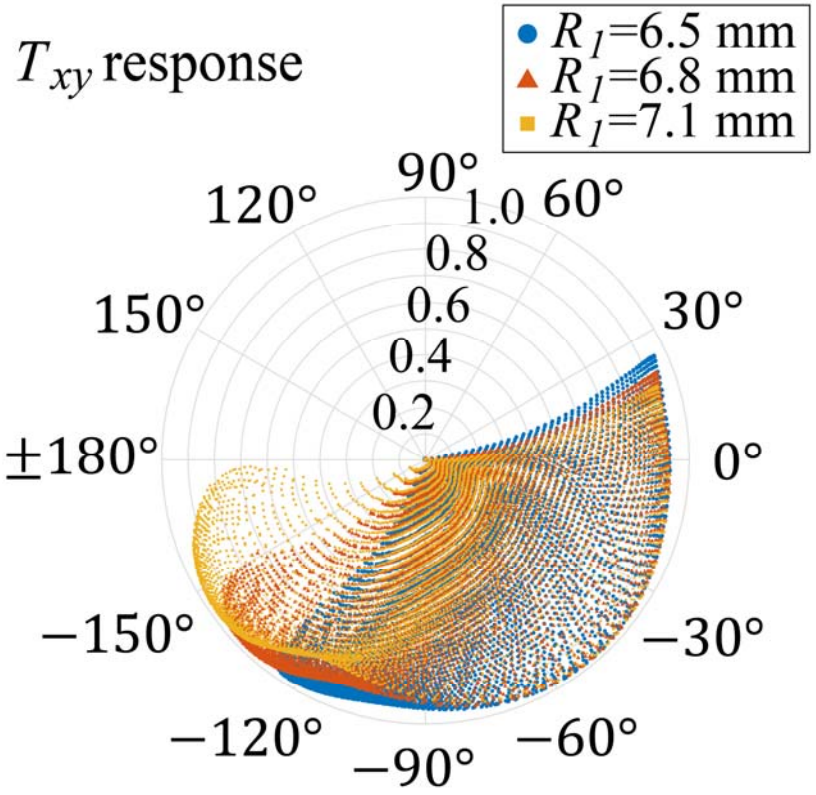

Figure 3-5 Polar diagram of all the results evaluated.

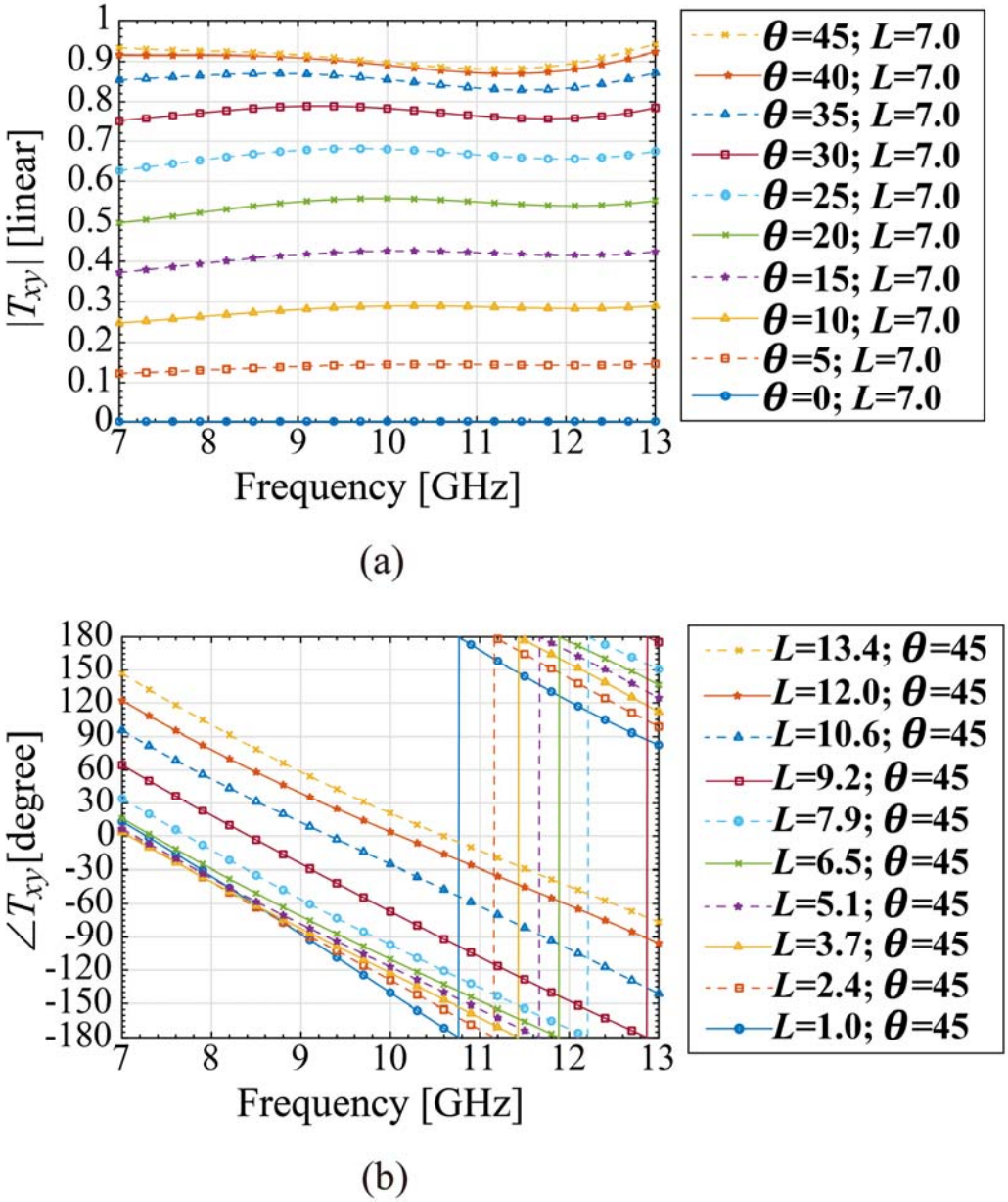

Figure 3-6 Frequency responses of T_{xy} (a) Frequency responses of $|T_{xy}|$ with fixed value of L and discrete values of θ. (b) Frequency responses of $\angle T_{xy}$ with fixed value of θ and discrete values of L. All the results are based on the element configuration of $R_1 = 6.8$ mm

3.1.2 Transmitarray Synthesis

For transmitarray synthesis, radiation pattern of the transmitarray antenna with specific element distribution need to be computed efficiently. Here, array factor-based approach as presented in Chapter 2 is used, and the calculation formula is shown in equation 2-16. The incident field distribution is determined by full-wave simulation instead of cosine q model. The element power factor is 1.2 in this design. By adopting FFT algorithm, the radiation pattern is obtained efficiently in a discrete number of angular coordinates (300×300 points in this design). Proper $Mask$ functions (M_U, M_L) are defined to restrict the achievable radiation pattern to meet the design requirements. Classical fitness function is defined here as [81, 82]:

$$\begin{aligned} \mathbf{COST} = & \sum_{\substack{(u,v) \in \text{ beam region} \\ and\ |E(u,v)| < M_L(m,n)}} \sum \left(|E(u,v)| - M_L(u,v)\right)^2 \\ & + \sum_{\substack{(u,v) \notin \text{ beam region} \\ and\ |E(u,v)| > M_U(m,n)}} \sum \left(|E(u,v)| - M_U(u,v)\right)^2 \end{aligned} \tag{3-1}$$

where $E(u,v)$ is the calculated radiation patterns in angular coordinates, $M_{U/L}(u,v)$ represent the masks. Global-robust particle swarm optimization algorithm is deployed to execute the iteration loop. An initial position based on superposition method [83] could be added to reduce the loop time. The flowchart of the optimization is shown in Figure 3-7. The optimization is considered to be converged with stable value, and the element distribution on the aperture will be extracted for further verification.

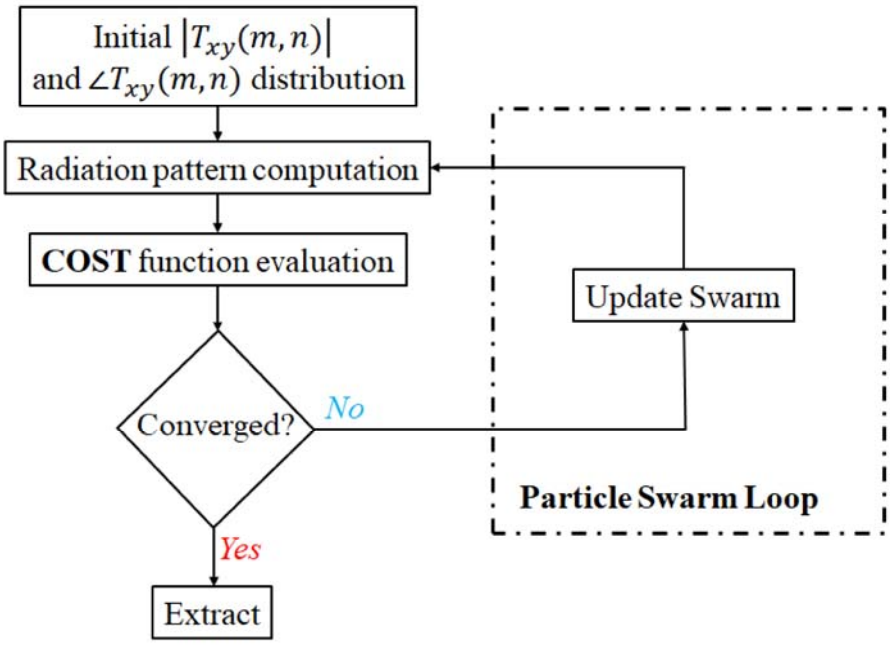

Figure 3-7 Flowchart of the optimization.

3.2 Design and Measurements of Transmitarray Antenna with A Flat-Top Beam

To verify the effectiveness of the amplitude-phase synthesis method, a 13×13-element transmitarray antenna with a flat-top beam is designed, fabricated, and tested. The sector region is set from $0.12 < u < 0.22$, $|v| \leq 0.17$, and the maximum SLL outside the beam region is set to -30 dB. Besides, the maximum tolerance in sector region is fixed to 1 dB. For comparison purpose, the phase-only synthesis method is also implemented by enforcing the θ of each element on the aperture to $45°$, where the $|T_{xy}|$ is approximately unity. The optimization parameters are the same for both loop-runs, and are listed in Table 3-2. After the convergence of the optimizations, the

TABLE 3-2
OPTIMIZATION SETTINGS

Inertial weight	1.1~0.1
Self-/social-knowledge constants	2
Swarm size	1000
Initial particle position	superposition

element distributions are extracted. Then, the full antenna system is modeled and verified using Ansys HFSS simulator. Antenna prototype with amplitude-phase synthesis method was fabricated and tested. For measurement, firstly, radiated far-field θ-/φ-components were tested separately in space, with X-band standard gain horn as receiver. Then, Co-/Cr-Pol radiation patterns were directly computed in postprocessing step. The Co-/Cr-Pol components in this design are based on the Ludwig third definition [84], and the formula is shown below:

$$\begin{pmatrix} E_{Co} \\ E_{Cr} \end{pmatrix} = \begin{bmatrix} \cos\varphi & -\sin\varphi \\ \sin\varphi & \cos\varphi \end{bmatrix} \bullet \begin{pmatrix} E_{\theta} \\ E_{\varphi} \end{pmatrix} \tag{3-2}$$

where $E_{\theta/\varphi}$ denote the measured radiated far-field components, and φ represents the angle in the spherical coordinate system.

The initial particle position for the synthesis is computed based on the superposition principle without amplitude modulation, leading to the same fitness function value at the beginning of the loop for amplitude-phase synthesis and phase-

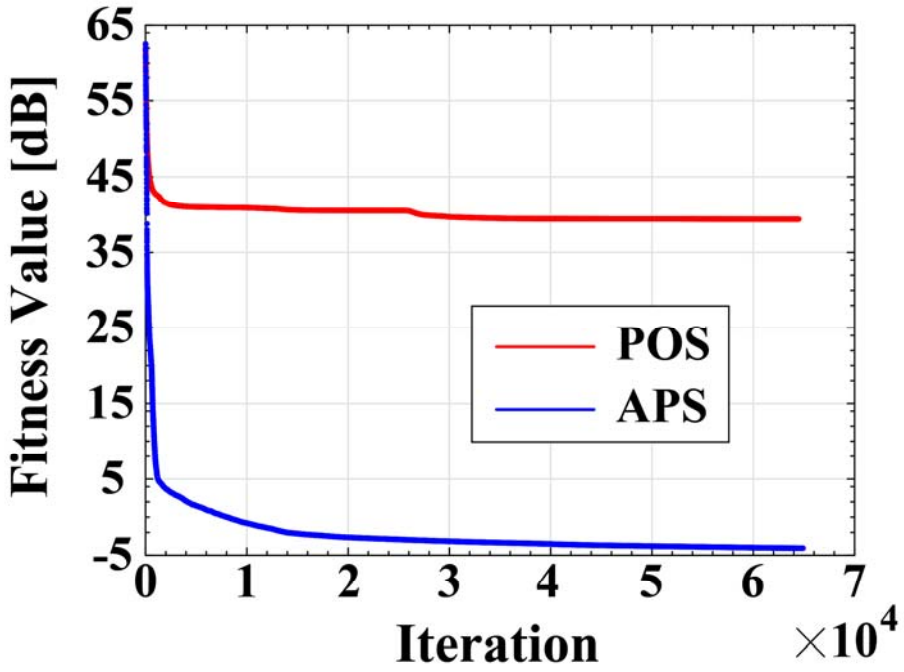

Figure 3-8 Convergence curves.

only synthesis situations. The convergence curves are depicted in Figure 3-8, revealing faster convergence rate of phase-only synthesis method and much better final result of amplitude-phase synthesis method. The optimal amplitude and phase distribution at 10 GHz for amplitude-phase synthesis situation are shown in Figure 3-9 (a) and (b), respectively. The calculated normalized radiation patterns for both situations at 10 GHz are plotted in Figure 3-10 (a) and (b). The transformation relation between angular coordinates and spherical coordinates is shown in the following:

$$\begin{cases} u = \sin\theta\cos\varphi \\ v = \sin\theta\sin\varphi \end{cases} \tag{3-3}$$

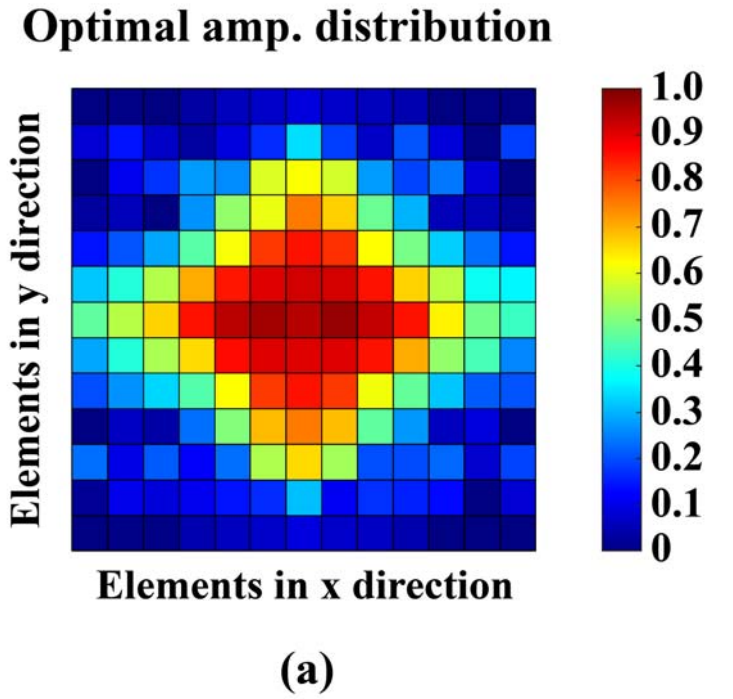

Figure 3-9 Optimal distribution at 10 GHz (a) Optimal $|T_{xy}|$ distribution of APS. (b) Optimal $\angle T_{xy}$ distribution of APS.

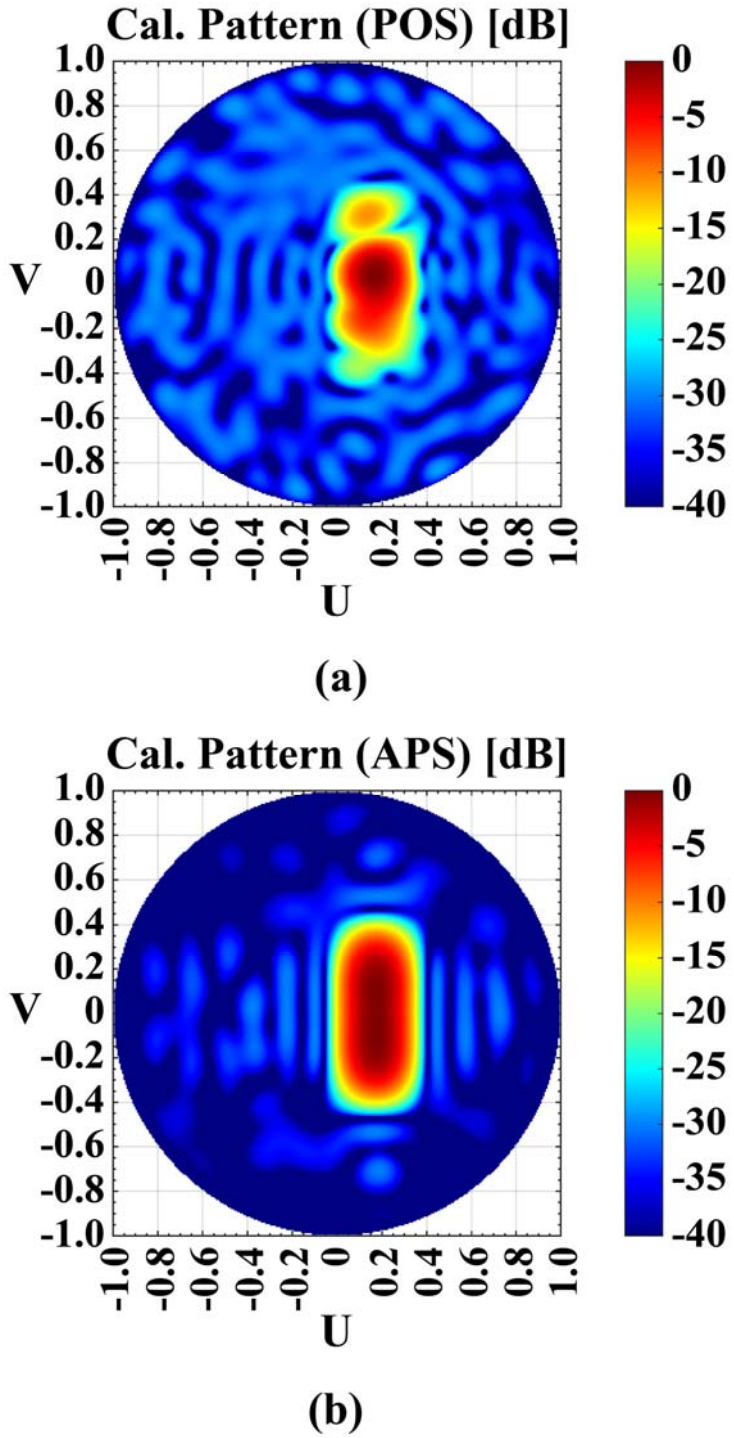

Figure 3-10 (a) Calculated radiation pattern of POS. (b) Calculated radiation pattern of APS. Both at 10 GHz.

Here, (θ, φ) are the angles in spherical coordinate. More complete sector beam can be observed for amplitude-phase synthesis situation. Figure 3-11 (a) and (b) depict the simulated normalized Co-Pol radiation patterns for both situations at 10 GHz in z>0 hemispace, from which the same conclusion can be addressed. For clarity, the normalized calculated/simulated radiation patterns cut in $u = 0.17$ plane are extracted and plotted in Figure 3-12 for both situations. Sector even cannot be formed by phase-only synthesis method. High agreement between calculated/simulated results can only be observed in the beam region. The simulated normalized radiation pattern in z<0 hemispace for amplitude-phase synthesis situation is depicted in Figure 3-13, where leakage of the energy is evident and the normalized back lobe is about -8 dB. However, the leakage is isolated by the aperture, and it has little effect on the beam region, which could be an advantage for this design.

The photograph of the fabricated prototype and the layout of the middle layer are shown in Figure 3-14 (a) and (b), respectively. The measured absolute Co-Pol radiation pattern and measured normalized Cr-Pol radiation pattern in z>0 hemispace at 10 GHz are presented in Figure 3-15 (a) and (b). The simulated and measured radiation patterns cut in u=0.17 plane and v=0 plane for both Co-/Cr-Pol are shown in Figure 3-16 (a) and (b), respectively. Realized gain of 18 dBi at 10 GHz is achieved. Besides, a reasonable agreement between these results is confirmed. The simulated Co-Pol radiation patterns cut in u=0.17 plane and v=0 plane at multiple frequency points are depicted in Figure 3-17 (a) and (b), respectively. The patterns are normalized to the value at 10 GHz. Radiation consistency can be observed, directly revealing the potential of wideband operation for this design.

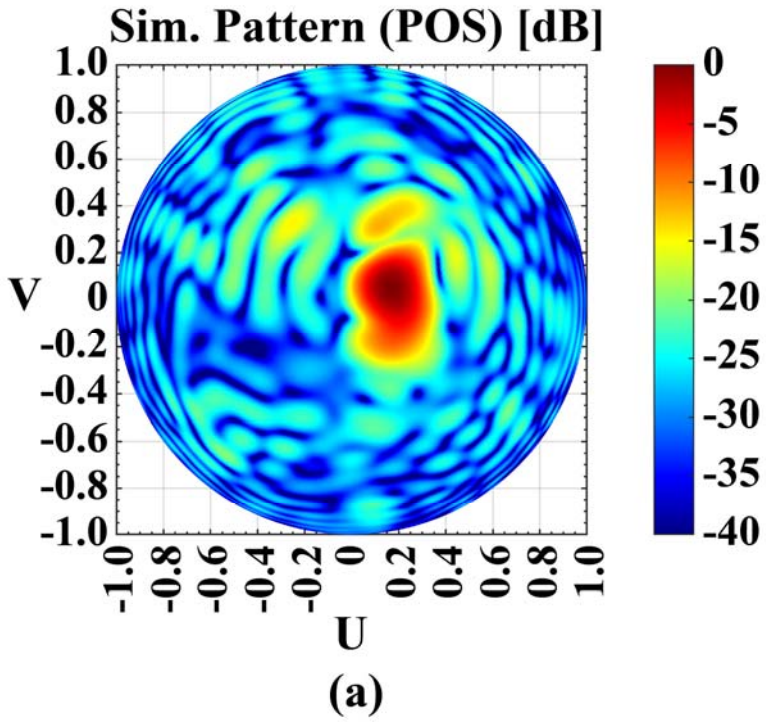

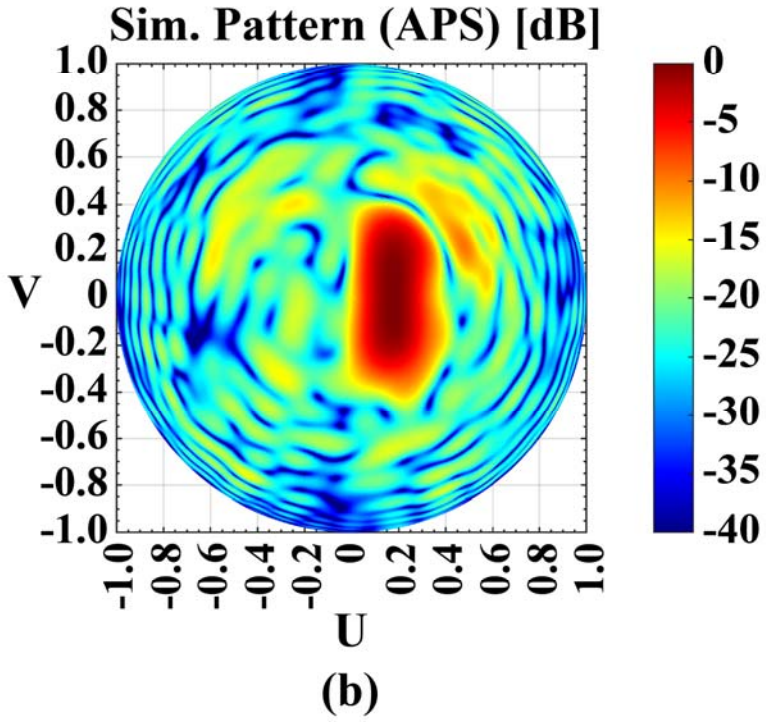

Figure 3-11 (a) Simulated Co-Pol radiation pattern (z>0) of POS. (b) Simulated Co-Pol radiation pattern (z>0) of APS. Both at 10 GHz

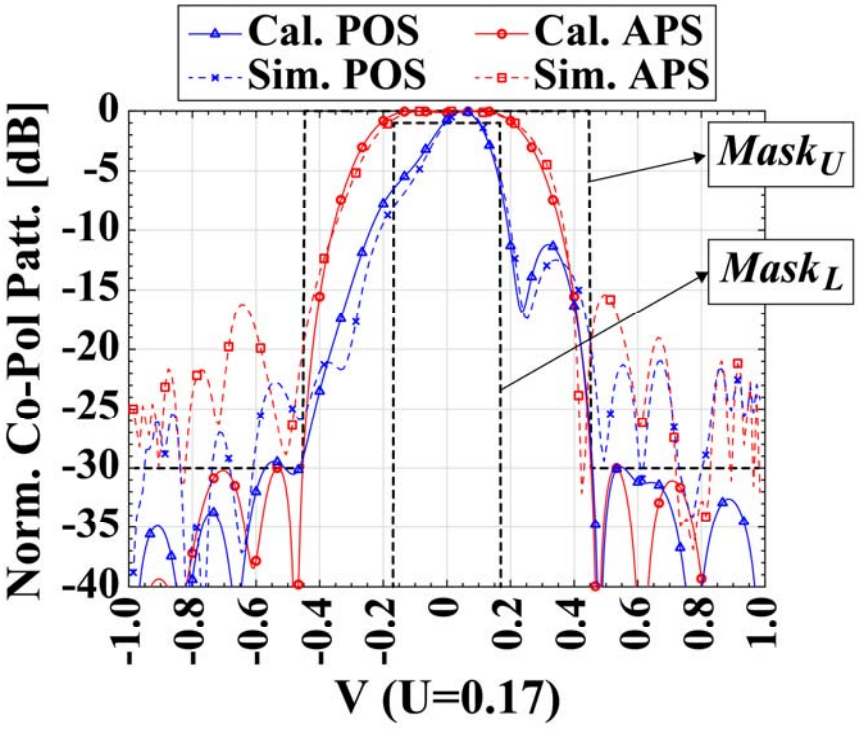

Figure 3-12 Radiation patterns cut in $u = 0.17$ plane for both APS and POS situations.

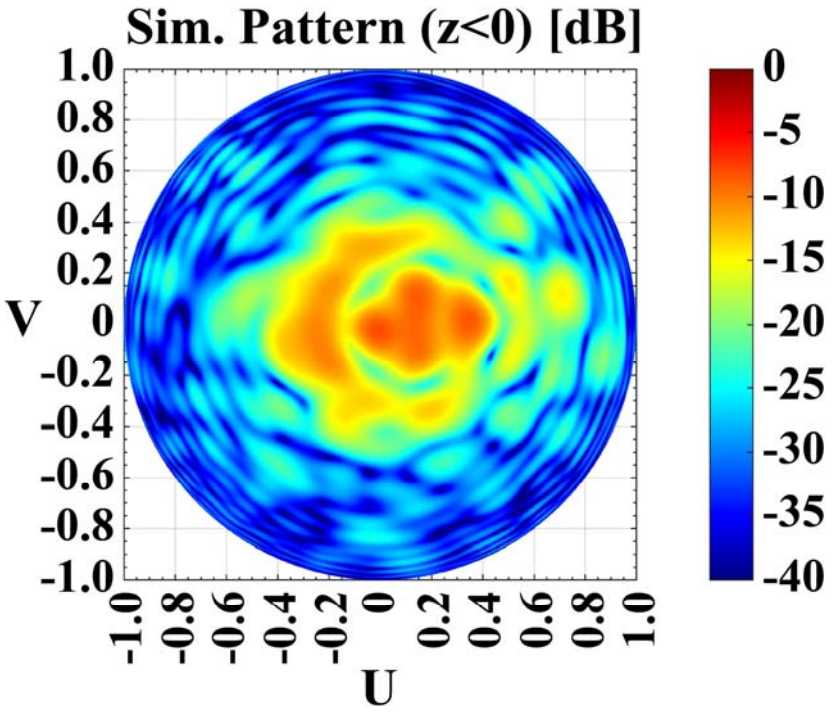

Figure 3-13 Simulated radiation pattern of APS in z<0 hemispace.

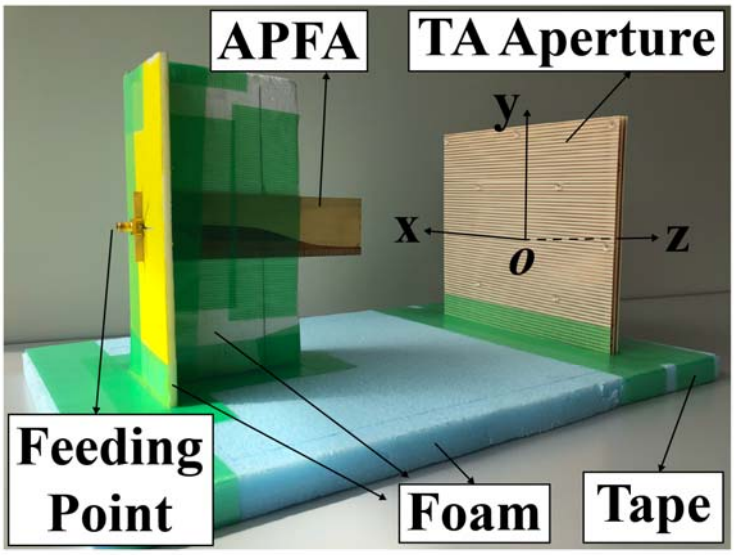

(a)

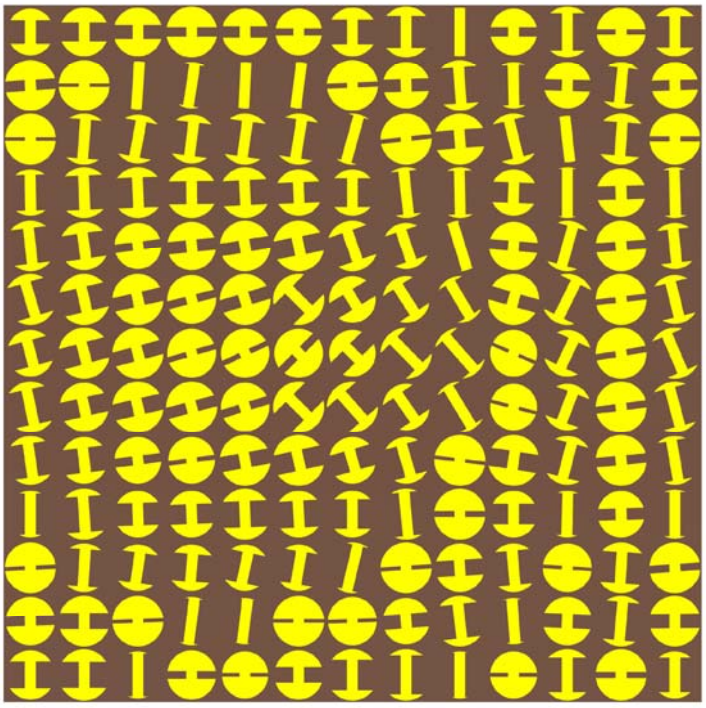

(b)

Figure 3-14 (a) Photograph of the fabricated prototype; (b) Element layout in the middle layer.

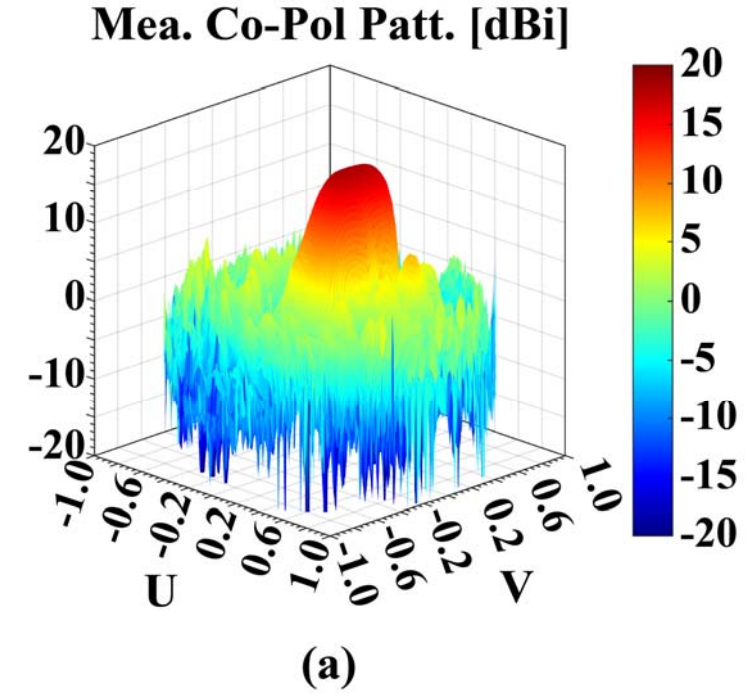

(a)

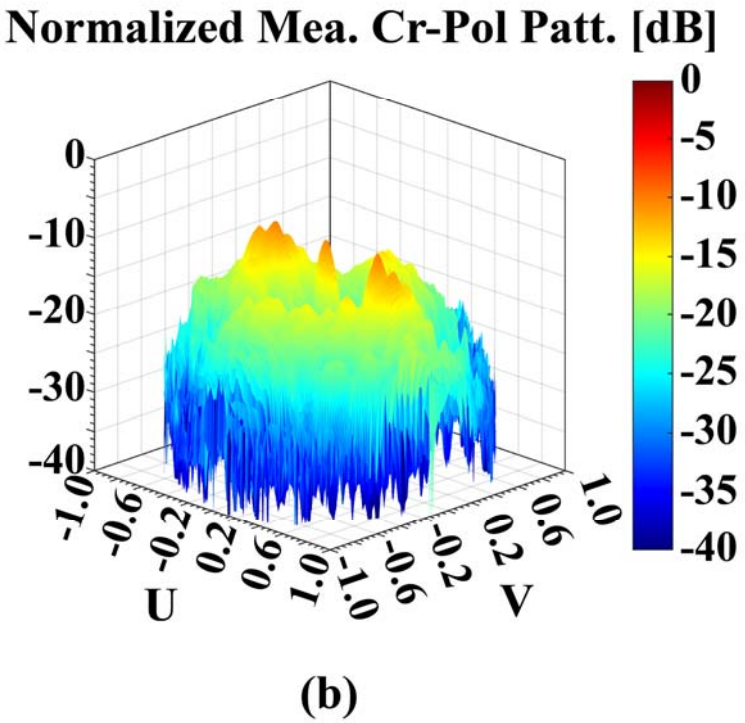

(b)

Figure 3-15 (a) Measured Co-Pol radiation pattern in z>0 hemispace. (b) Measured Cr-Pol radiation pattern in z>0 hemispace. Both at 10 GHz.

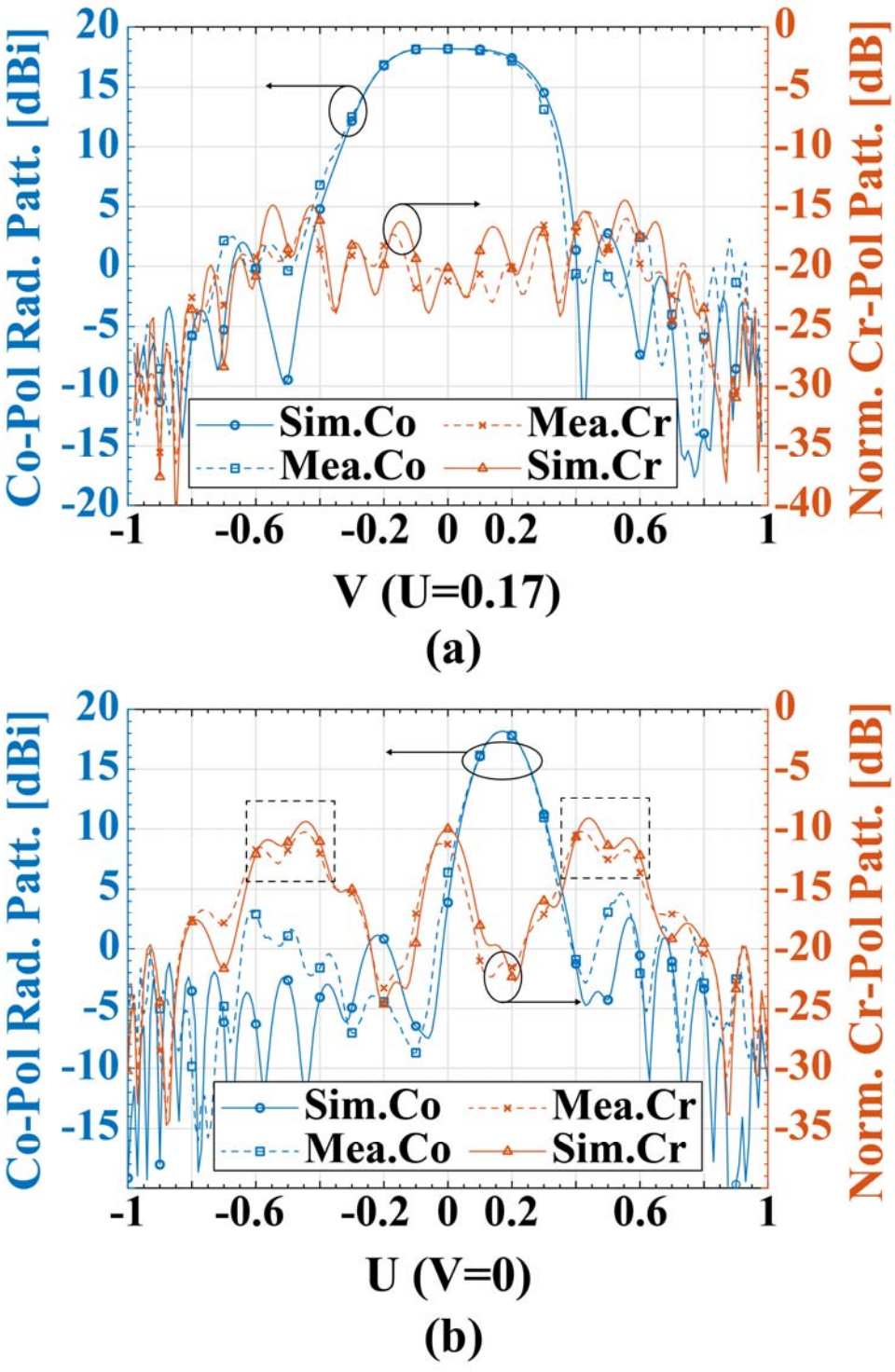

Figure 3-16 (a) Normalized Co-/Cr-Pol radiation pattern cut in $u = 0.17$ plane. (b) Normalized Co-/Cr-Pol radiation pattern cut in $v = 0$ plane. All the results are evaluated at 10 GHz.

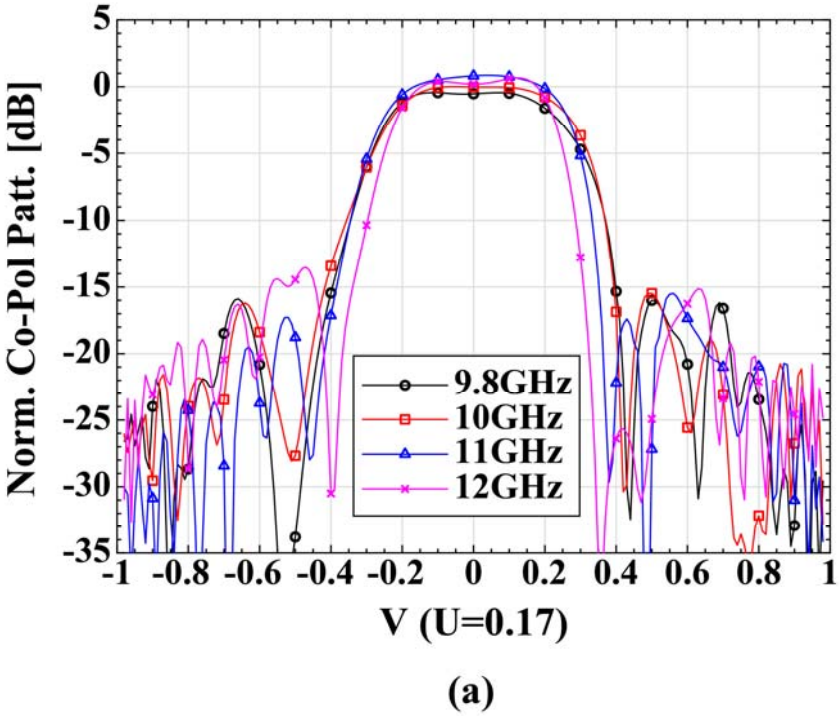

(a)

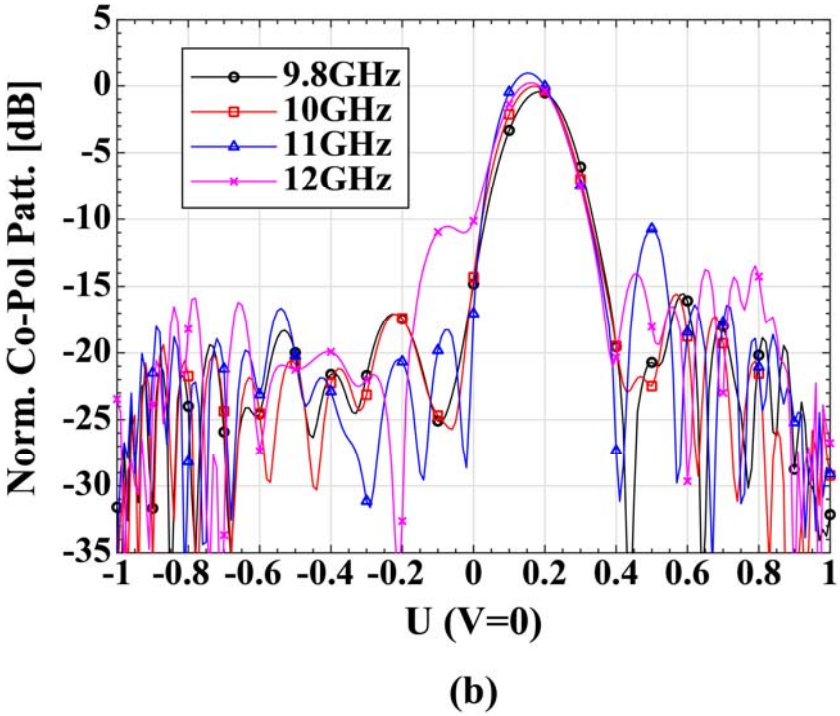

(b)

Figure 3-17 (a) Co-Pol radiation patterns cut in $u = 0.17$ plane at multiple frequency points. (b) Co-Pol radiation patterns cut in $v = 0$ plane at multiple frequency points. All the results are normalized to the value at 10 GHz.

3.3 Discussion and Summary

A small-sized ($6.5\lambda_0 \times 6.5\lambda_0$) transmitarray antenna with a flat-top radiation pattern is successfully synthesized by using the developed amplitude-phase synthesis method. Besides, the comparison between the developed amplitude-phase synthesis method and conventional phase-only synthesis method is widely provided, demonstrating more flexible beam-shaping capability of the former one. However, there are some points need to be pointed out:

1) No matter which methods are under consideration, the results of the array factor-based calculation can be matched with those of the full-wave simulation only in beam region. The discrepancy outside the beam region is mainly caused by the interelement coupling and edge diffraction, and can be mitigated by using more realistic calculation model in [85-87]. However, this could lead to increased computation cost during optimization process.
2) The marked undesired large Cr-Pol in Figure 3-16 (b) is mainly caused by the large edge diffraction across $\mathrm{v} = 0$ plane, which is attributed to the asymmetric radiation pattern provided by the source feed presented in Chapter 2. However, this can be mitigated by using source feed with symmetric radiation pattern or enlarging the transmitarray aperture across $\mathrm{v} = 0$ plane.
3) The required flat-top beam can also be synthesized by the conventional phase-only synthesis method with a larger transmitarray aperture size. Therefore, when the aperture size is limited, the developed amplitude-phase synthesis method is an efficient method to design beam-shaping transmitarray antenna.

Chapter 4

Transmit-Reflect-Combined-Array Antenna with Forward and Backward Beams

In this chapter, a novel four-layer polarization-dependent multifunctional element is proposed for designing single-feed transmit-reflect-combined-array antenna with expected forward and backward beams, which is desired in interferometric synthetic aperture radar [10], simultaneous indoor and outdoor communications, and tunnel communications[11, 12]. Considering the polarization sensitive behavior of the element developed in Chapter 3, in order to support the ability of reflection phase control, one more bowtie layer is added to form a new element. By optimizing the element geometric parameters, the proposed element provides the features of simultaneous and decoupled control of transmission phase and reflection phase. Here, generalized scattering matrix (GSM)-based cascaded network solver is implemented again to efficiently evaluate the element performance during the optimization process. Besides, the element performance under oblique incidence is also investigated, demonstrating stable behavior for both transmission response and reflection response. The oblique incidence stability of the element guarantees the high aperture efficiency of the resulting antenna. Based on these studies, a 13×13-element antenna prototype is designed, fabricated, and tested. The antenna operates as transmitarray and reflectarray at the same frequency band, by discriminating in polarization of the source feed. The measured realized gains of the transmitarray functionality and reflectarray functionality at 10 GHz are 23.5 dBi with 22.6% 1-dB fractional gain bandwidth and 24 dBi with 18.6% 1-dB fractional gain bandwidth, respectively. Moreover, the antenna achieves aperture efficiency of 42.2%

at 10 GHz for transmitarray functionality and 47.3% at 10 GHz for reflectarray functionality, which are better than the existing designs. In addition, in order to verify the simultaneously bidirectional capability of the antenna, an additional experiment, which is based on slanting the source feed, is implemented. Measured results match well with those of simulated results.

4.1 Design and Optimization of the Unit Cell

The 3-D perspective view of the four-layer multifunctional unit cell is shown in Figure 4-1 (a) with periodicity of $P = 15$ mm, which is equivalent to $0.5\lambda_0$, where λ_0 is the free-space wavelength at 10 GHz. The metal structures, as the yellow parts

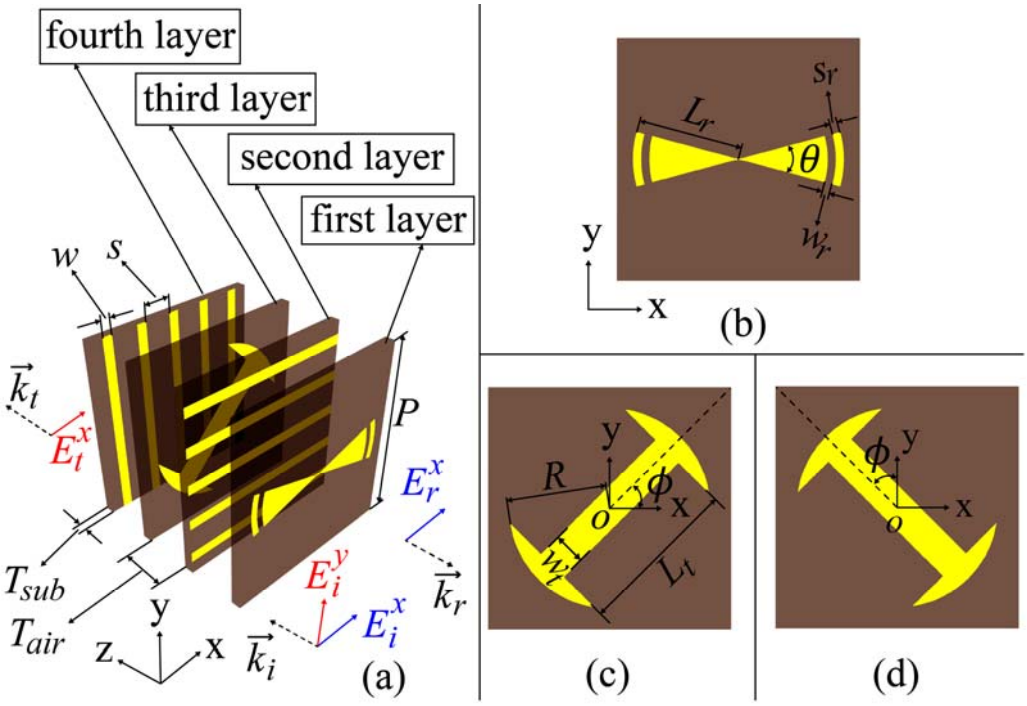

Figure 4-1 Unit cell view (a) 3-D view of the unit cell; red lines: polarization-rotation transmission process; blue lines: reflection process. (b) Top view of the first layer. (c) Top view of the third layer. (d) Mirrored structure of the third layer.

indicate, are printed on four dielectric substrates ($\varepsilon_r = 3.3,\ \tan\delta = 0.001,\ T_{sub} = 0.8$ mm) with same air gaps ($T_{air} = 4$ mm). The detailed top view of the first layer and third layer are shown in Figure 4-1 (b) and (c), respectively. The first layer is composed of bowtie dipole, where the bowtie angle is θ and dipole length is L_r. An arc gap with width of w_r and boundary width of s_r is inserted into the bowtie. As shown in Figure 4-1 (c), the shape of the third layer is similar with the middle layer of the element in Chapter 3. However, in this chapter, the angle ϕ is fixed to $45°$ to maintain the high value of the transmission magnitude when the transmission phase is changing. The second layer and fourth layer are two orthogonal grid polarizers with the same geometric parameters used in Chapter 3. The responses of the element are determined by the polarization of the incident wave. On one hand, as shown by the red lines in Figure 4-1 (a), with y-polarized normal illumination, the wave is immune to the first layer and completely transmitted to the second layer. Then, the remaining layers guide the wave pass through the element with the same mechanism presented in Chapters 2 and 3. Besides, the transmission phase is controlled by varying L_t. On the other hand, considering x-polarized normal illumination as shown by the blue lines in Figure 4-1 (a), the incident wave is fully reflected due to the frequency cut-off of the second layer. The reflection phase is controlled by altering L_r. It should be mentioned that due to coupling effect between transmission process and reflection process, the variation of L_r has undesired effect on the transmission phase. Therefore, in order to realize independent control of reflection phase (only by L_r) and transmission phase (only by L_t), the geometric parameters of the element ($\theta,\ s_r,\ w_r,\ R,\ w_t$) need to be optimized, which is achieved by generalized scattering matrix (GSM)-based cascaded network solver.

In this chapter, generalized scattering matrix (GSM)-based approach is implemented again to efficiently evaluate the element performance. With only the two fundamental Floquet space harmonics taken into consideration, as shown in Figure 4-2, the element is equivalent to a 4-port network with 7 building blocks representing each layer. Besides, the element responses should meet the following requirements as

much as possible [1, 88]:

1) Minimize the coupling effect between transmission and reflection;

2) Phase shift coverage of $360°$ for both transmission and reflection;

Parametric studies have found that there is a trade-off between the coupling effect and the phase coverage. The coupling effect is mainly caused by the opening angle of the bowtie structure in the first layer. Here, we choose to minimize the coupling effect first,

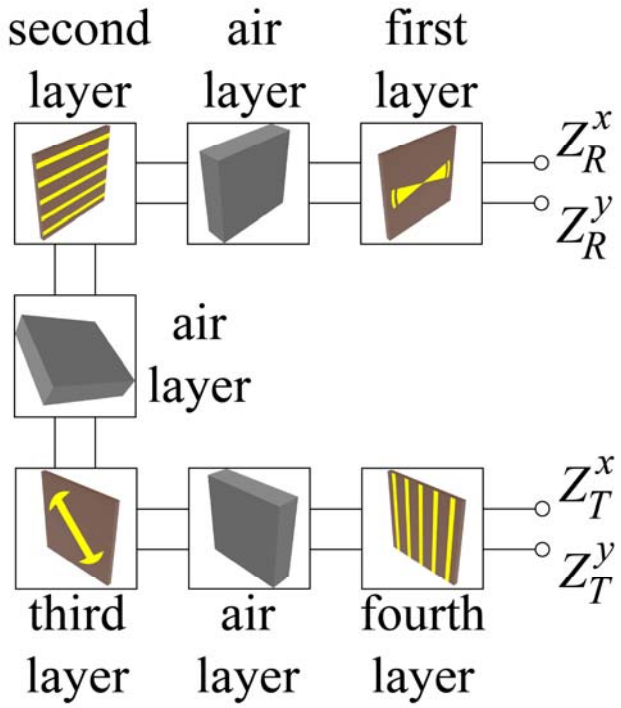

Figure 4-2 Network model of the proposed element.

TABLE 4-1
FINAL DESIGN PARAMETERS OF THE ELEMENT

First layer		Third layer	
θ	30°		
s_r	0.5 mm	R	6.2 mm
w_r	0.5 mm	w_t	2.0 mm
L_r	2.0-7.4 mm	L_t	1.0-12.2 mm

and the final design parameters are listed in Table 4-1.

In this chapter, the element performance can also be fully characterized by the two matrix equations listed in equations 2-7~2-10. Components of R_{xx} and T_{xy} are essential. The R_{xx} and T_{xy} vs. L_t or L_r are shown in Figure 4-3, where all the results are evaluated at 10 GHz with normal incidence. Decoupled control of transmission phase and reflection phase is achieved. The transmission phase is only controlled by varying L_t in the third layer, while the reflection phase is only controlled by varying L_r in the first layer. The responses of R_{xx} and T_{xy} components at multiple frequency points with normal incidence are plotted in Figure 4-4. For transmission phase responses as shown in Figure 4-4 (b), around $150°$ phase shift coverage can be directly obtained by varying L_t. An additional π phase shift is created by simply mirroring the structure of the third layer as shown in Figure 4-1 (d), consequently leading to around $300°$ total transmission phase coverage achieved, which is sufficient for transmitarray design [1]. For reflection phase responses as shown in Figure 4-4 (d), similar behaviors between each frequency point are obtained, and reflection phase coverage of $280°$ is achieved. The element performance under oblique incidence is also studied and depicted in Figure 4-5, where the first angle in the legend denotes the θ_{inc}, while the second one represents the φ_{inc}. The performance is obtained by periodic boundary condition-based full-wave analysis with the entire element as one building block. Stable responses are obtained for both transmission and reflection, which is vital for antenna efficiency. Compared with reflection responses, the transmission responses are slightly more sensitive to oblique incident angle.

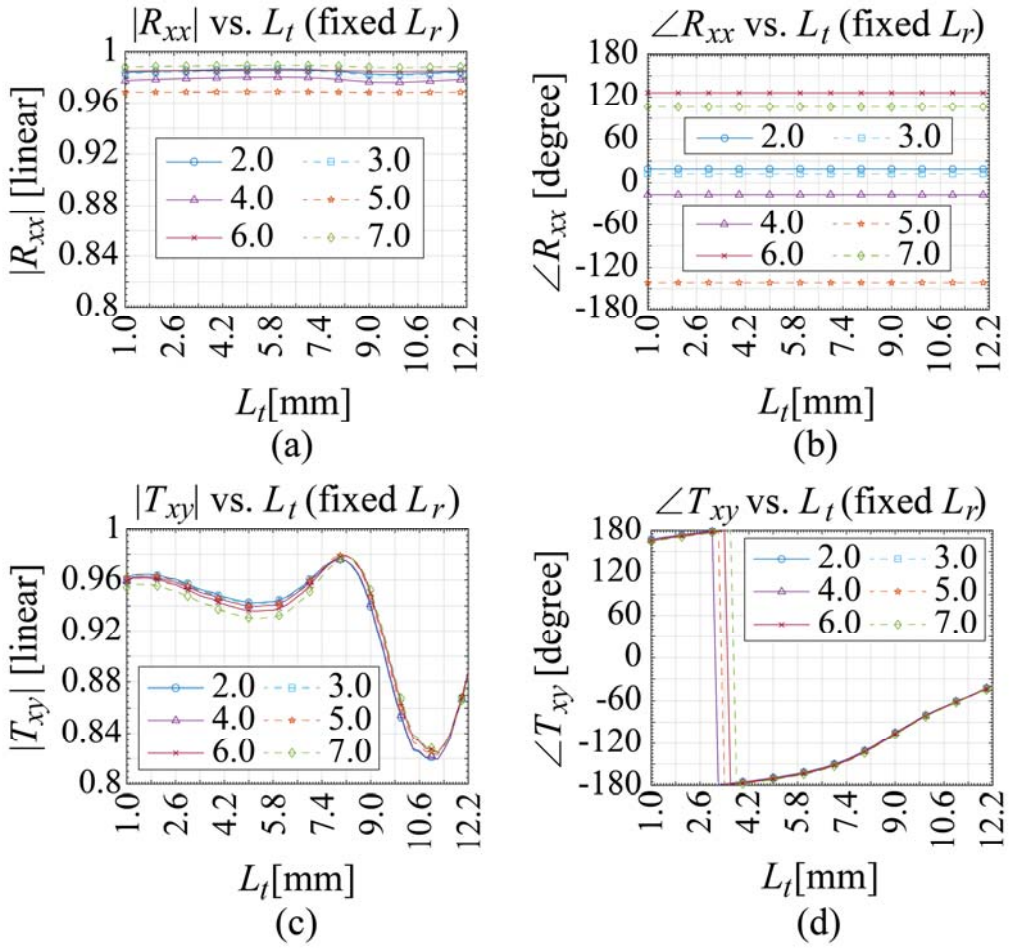

Figure 4-3 (a) $|R_{xx}|$ vs. L_t at discrete L_r. (b) $\angle R_{xx}$ vs. L_t at discrete L_r. (c) $|T_{xy}|$ vs. L_t at discrete L_r. (d) $\angle T_{xy}$ vs. L_t at discrete L_r. All the results are evaluated at 10 GHz.

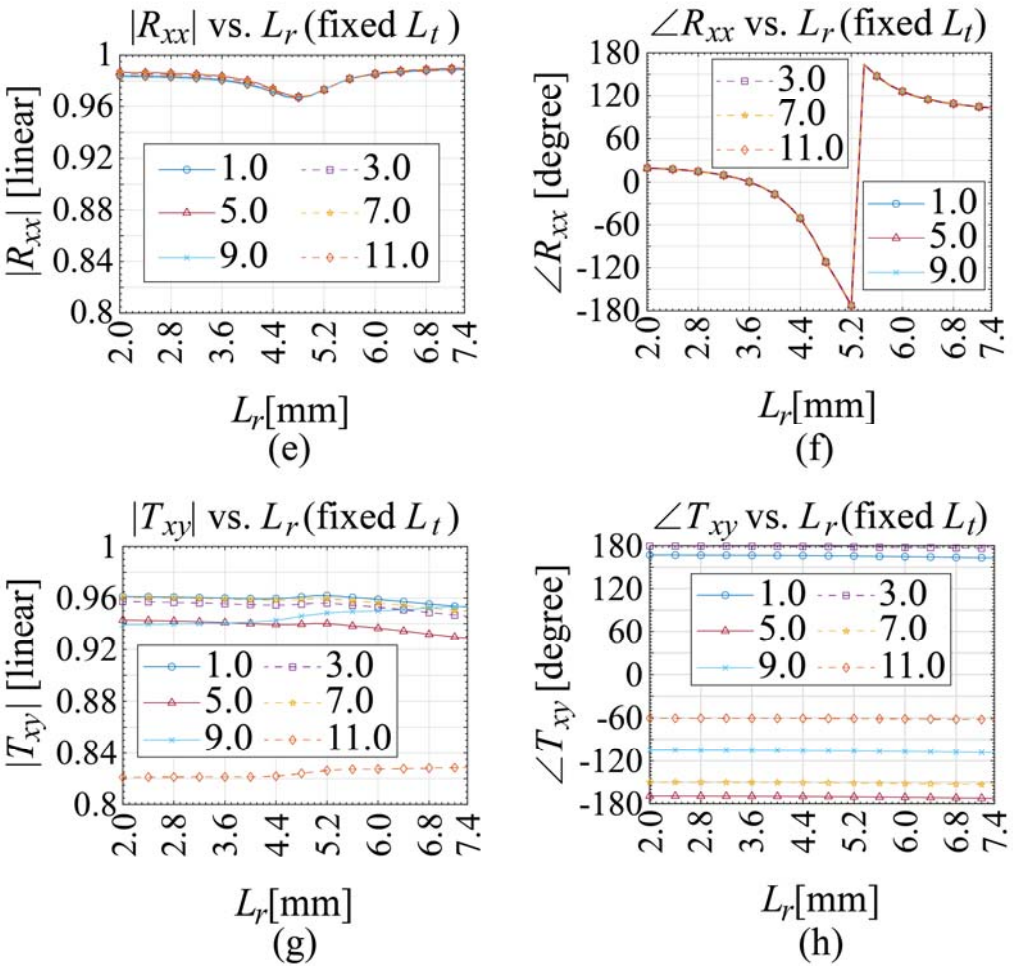

Figure 4-3 (e) $|R_{xx}|$ vs. L_r at discrete L_t. (f) $\angle R_{xx}$ vs. L_r at discrete L_t. (g) $|T_{xy}|$ vs. L_r at discrete L_t. (h) $\angle T_{xy}$ vs. L_r at discrete L_t. All the results are evaluated at 10 GHz.

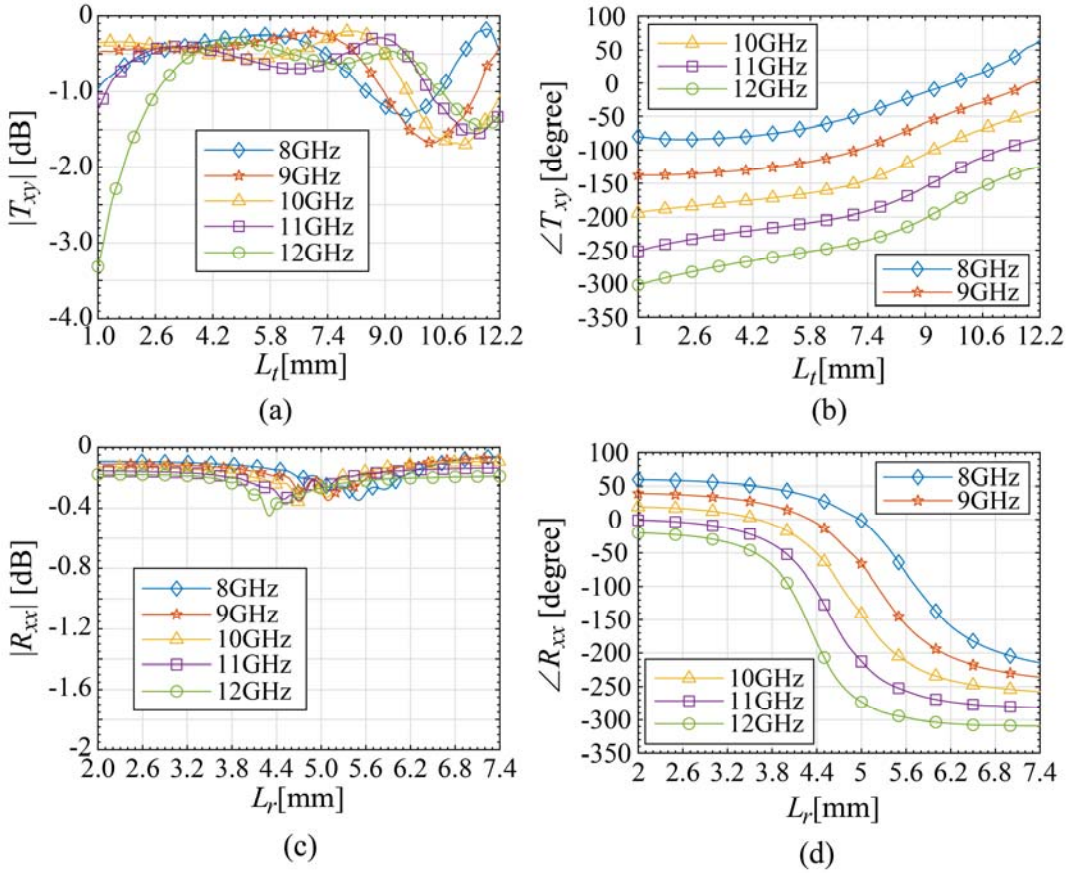

Figure 4-4 (a) $|T_{xy}|$ responses under normal incidence. (b) $\angle T_{xy}$ responses under normal incidence. (c) $|R_{xx}|$ responses under normal incidence. (d) $\angle R_{xx}$ responses under normal incidence.

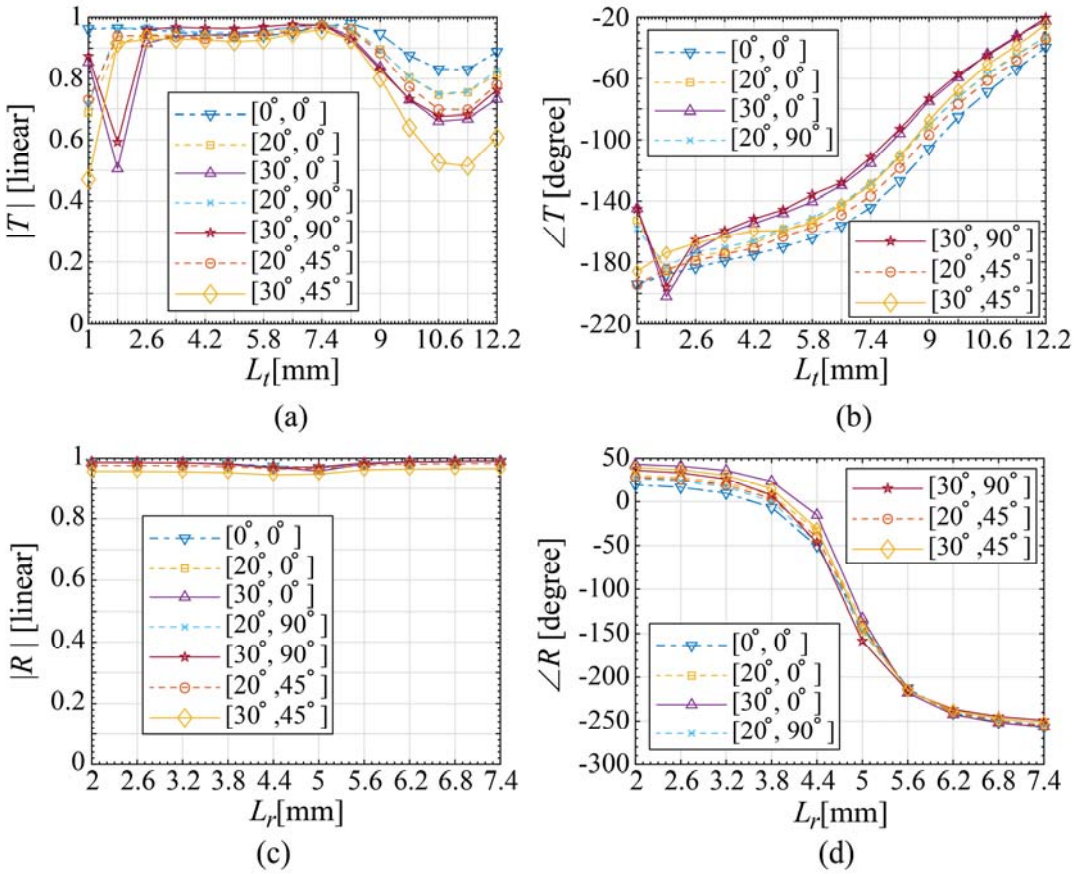

Figure 4-5 (a) Oblique responses of $|T|$ at 10 GHz. (b) Oblique responses of $\angle T$ at 10 GHz. (c) Oblique responses of $|R|$ at 10 GHz. (d) Oblique responses of $\angle R$ at 10 GHz.

4.2 System Design and Measurements

The antenna system configuration and functionality illustrations are shown in Figure 4-6. The antenna system configuration used in this chapter is the same as that in Chapter 3, where the aperture size is set to $D = 195$ mm (13×13-element) and $H = 320$ mm. For space-fed planar array antennas, each element on the aperture need to compensate the spatial phase delay from the source feed to that element to generate a pencil beam in desired direction. According to the array theory, the phase distribution is described as:

$$\phi^f(m,n) = -\psi_{mn}^{inc}(f) - \frac{2\pi f}{c} \cdot (x_{mn} \cos\varphi_b + y_{mn} \sin\varphi_b) \cdot \sin\theta_b \tag{4-1}$$

where $\phi^f(m,n)$ is the required phase distribution, $\psi_{mn}^{inc}(f)$ is the incident phase distribution on the aperture, f is the operating frequency, (x_{mn}, y_{mn}) are the coordinates of each element, and (θ_b, φ_b) denote the main beam direction. Due to completely independent control of the transmission phase and reflection phase of the element, the transmitarray functionality and reflectarray functionality can be designed individually. In this design, the beam for transmitarray is broadside as shown in Figure 4-6 (a), while that for reflectarray is along $\theta_b = 20^\circ$, $\varphi_b = -90^\circ$, which is shown in Figure 4-6 (b). The beam direction of reflectarray functionality is set to avoid the source feed blockage effect. Once the required phase distributions for both functionalities are determined, the required element layouts are obtained from Figure 4-4 (b) for transmitarray and Figure 4-4 (d) for reflectarray.

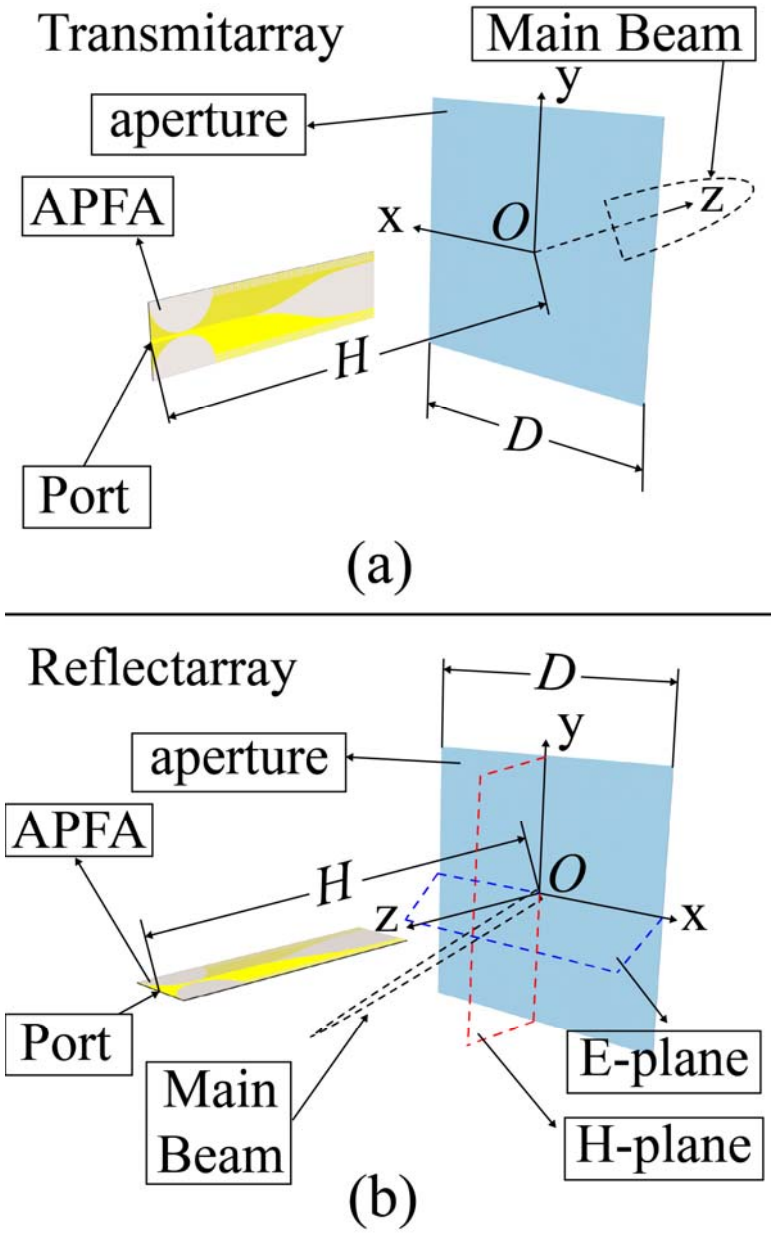

Figure 4-6 (a) TA functionality. (b) RA functionality.

The antenna is designed based on single frequency point at 10 GHz without any optimization. The final element layout of the first layer and third layer are shown in Figure 4-7, respectively. Figure 4-8 presents the antenna under test (AUT) models for transmitarray functionality and reflectarray functionality. For clarity, the results of transmitarray functionality and reflectarray functionality are discussed separately in the following.

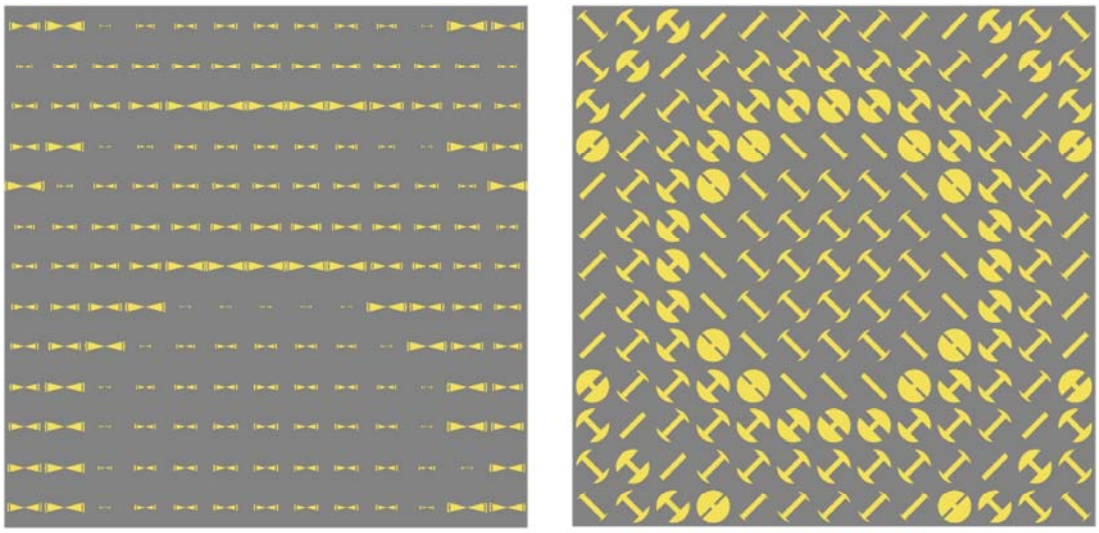

First Layer (a)

Third Layer (b)

Figure 4-7 Final element layout of (a) first layer; (b) third layer.

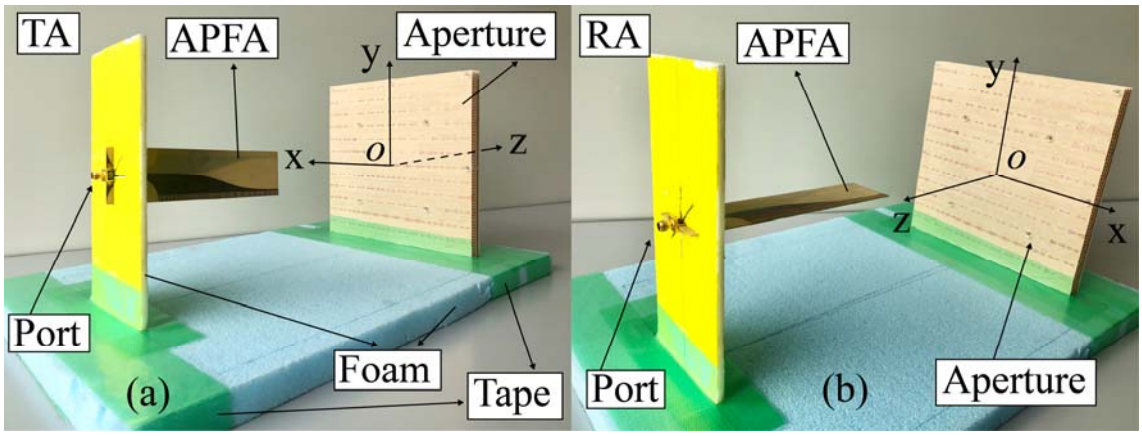

Figure 4-8 (a) Photograph of AUT for TA. (b) Photograph of AUT for RA.

4.2.1 Transmitarray Functionality Results

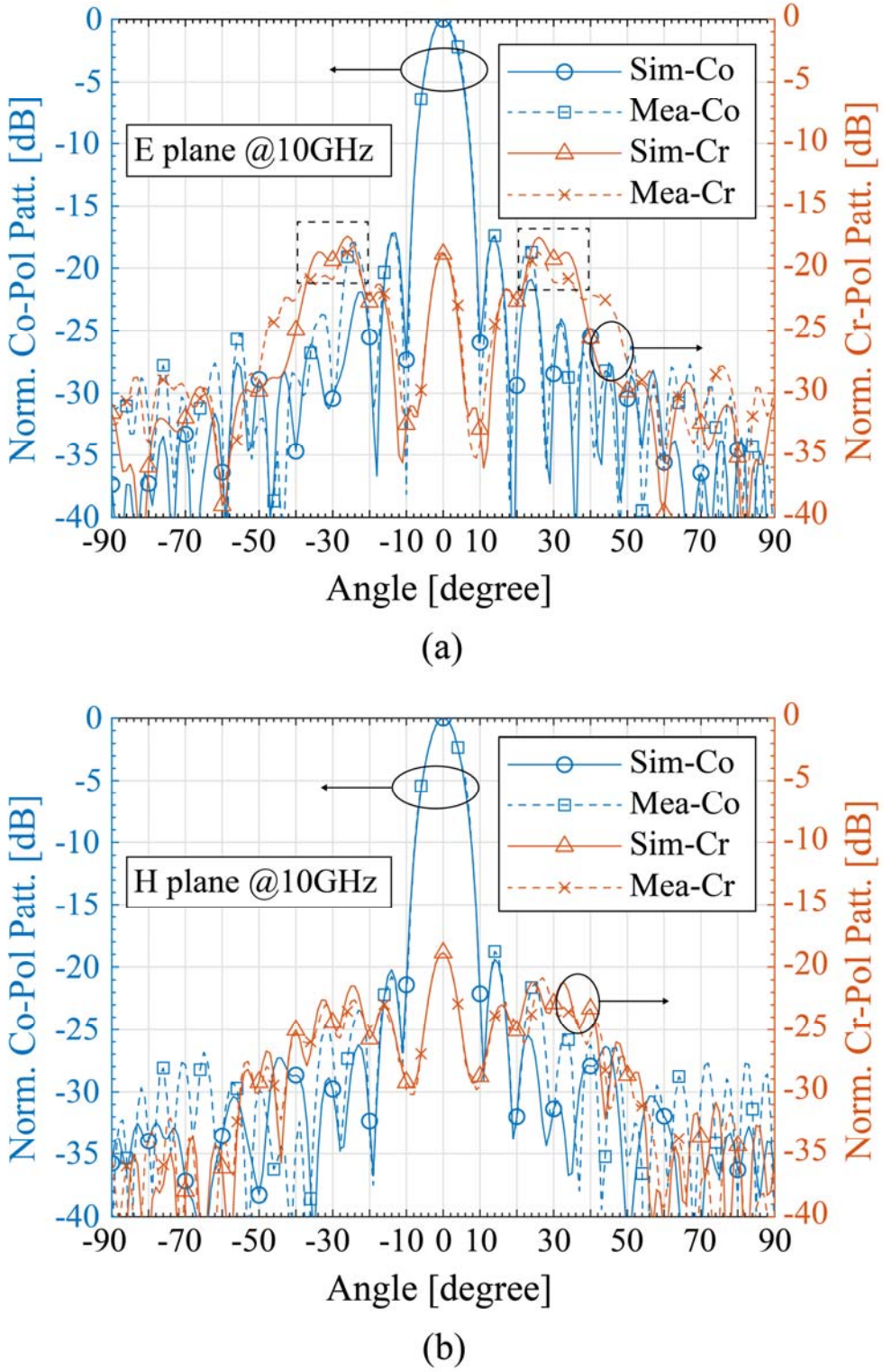

Figure 4-9 (a) Radiation patterns of TA in E-plane at 10 GHz. (b) Radiation patterns of TA in H-plane at 10 GHz.

The simulated and measured normalized radiation patterns for both Co-/Cr-Pol in E/H-plane at 10 GHz are depicted in Figure 4-9. Here, E-plane is XoZ plane, and H-plane is YoZ plane. Reasonable agreements between simulated and measured results can be observed. The marked undesired large Cr-Pol outside the beam region in Figure 4-9 (a) is mainly attributed to the large edge diffraction across E-plane caused by the asymmetric radiation pattern of the source feed presented in Chapter 2.

The frequency responses of the measured realized gain and aperture efficiency are depicted in Figure 4-10. There is a frequency shift of the best performance point occurring, which is mainly caused by the non-optimal system configuration. Following the standard definition, the measured fractional 1-dB realized gain bandwidth is 22.6%, corresponding to the frequency band from 10.1-12.7 GHz. Moreover, the 3-dB fractional gain bandwidth is 45.2%, denoting frequency band from 8.6-13.8 GHz. The aperture efficiency at 10 GHz is 42.2%. The peak aperture efficiency of 45.6% is achieved at 11 GHz.

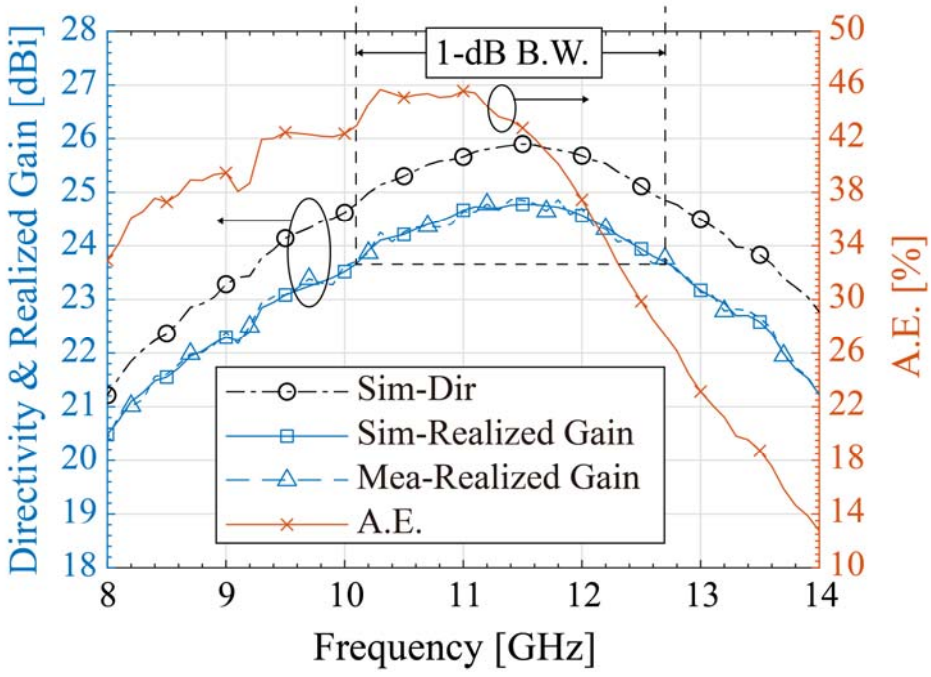

Figure 4-10 Frequency responses of the realized gain and aperture efficiency.

4.2.2 Reflectarray Functionality Results

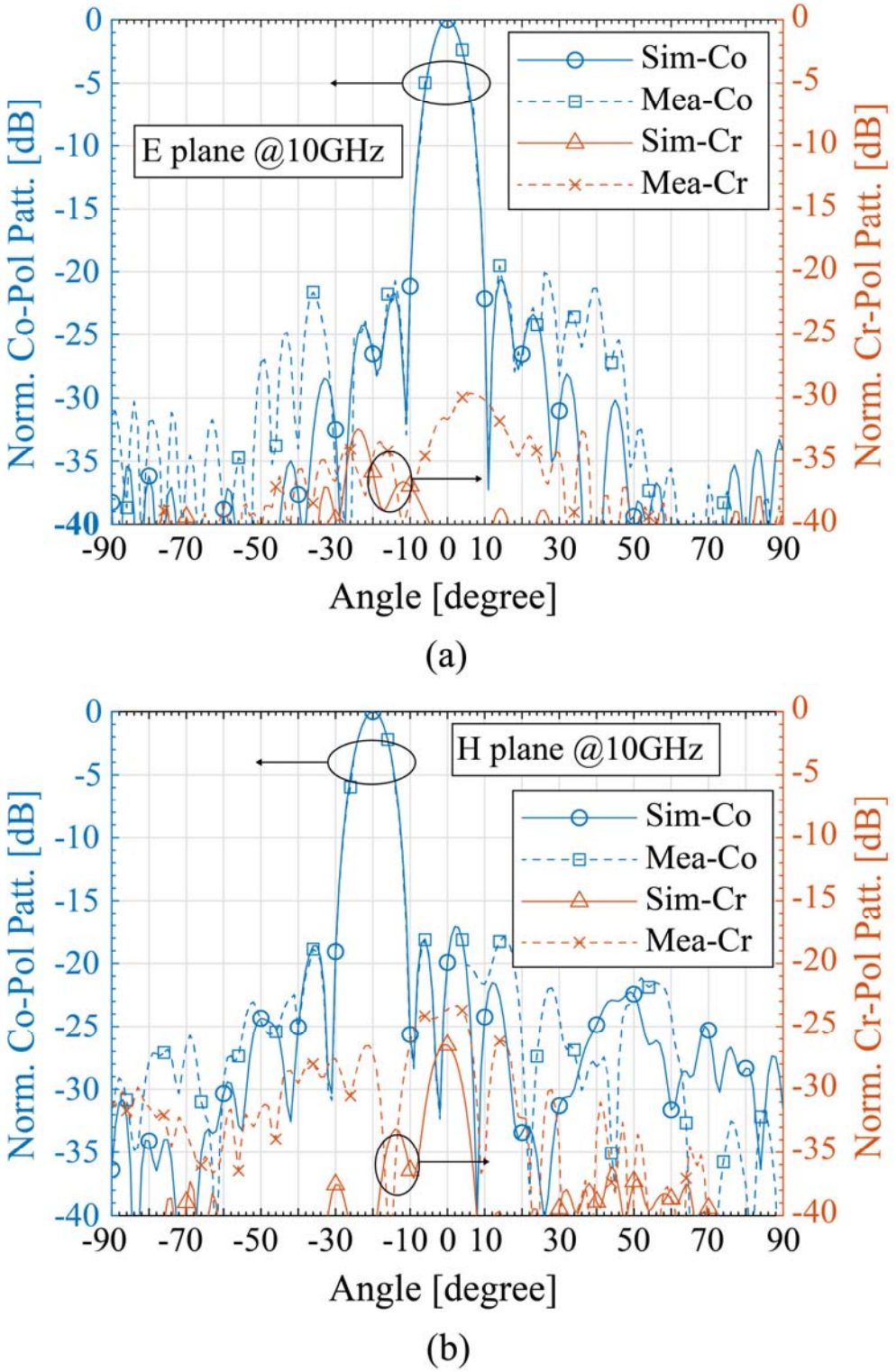

Figure 4-11 (a) Radiation patterns of RA in E-plane at 10 GHz. (b) Radiation patterns of RA in H-plane at 10 GHz.

The normalized Co-/Cr-Pol radiation patterns for both simulated and measured results at 10 GHz in E-/H-plane are shown in Figure 4-11. The E-/H-plane in this design are illustrated in Figure 4-6 (b). For Co-Pol, the measured results match well with those of simulation in main beam region. For Cr-Pol, large discrepancy occurs, which is mainly attributed to the structure of the AUT. For reflectarray, the feeding and fixing platform are on the same side with the aperture, which inevitably introduce test errors. However, as the Cr-Pol is still very low, the impact of this discrepancy on antenna gain is ignorable.

The frequency responses of the measured realized gain and aperture efficiency are plotted in Figure 4-12. It should be pointed out that the main beam deflects from $26°$ at 8 GHz to $17°$ at 12 GHz, which is mainly caused by the changes in propagation constant and reflection phase slope. Therefore, considering the beam squint, the realized gain in fixed direction of $\theta_b = 20^\circ$, $\varphi_b = -90^\circ$ is also depicted in Figure 4-12 by black lines, revealing a 1-dB fractional gain bandwidth of 18.6% (9.3-11.2 GHz). The aperture efficiency of 47.3% at 10 GHz is achieved.

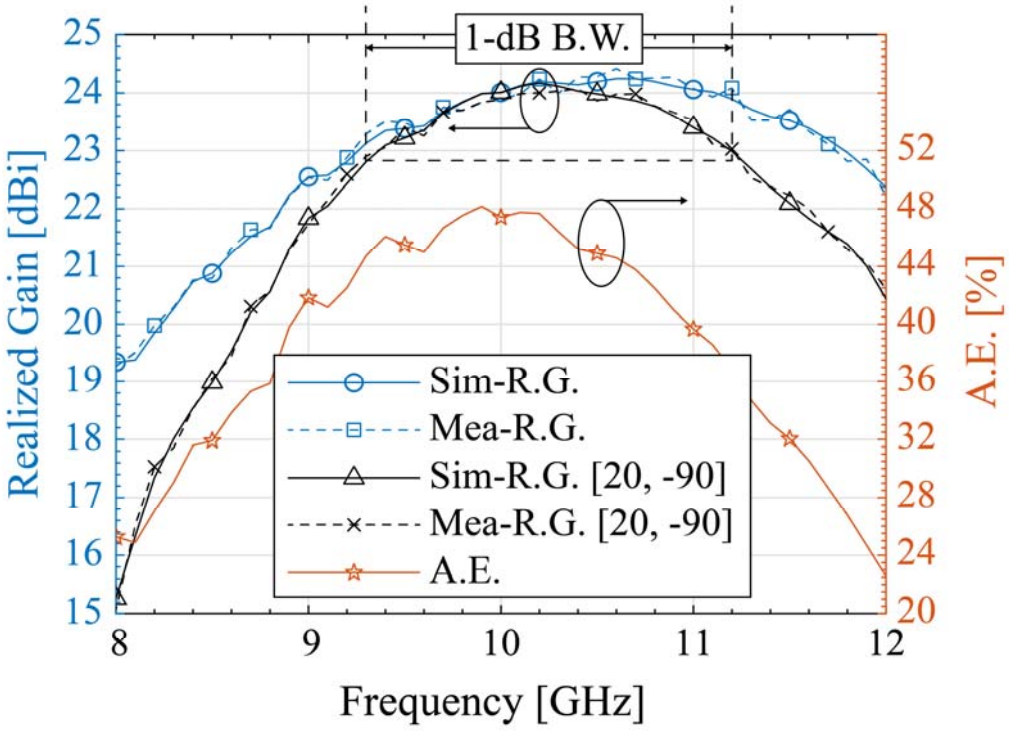

Figure 4-12 Frequency responses of the realized gain and aperture efficiency.

4.3 Simultaneously Bidirectional Capability Verification

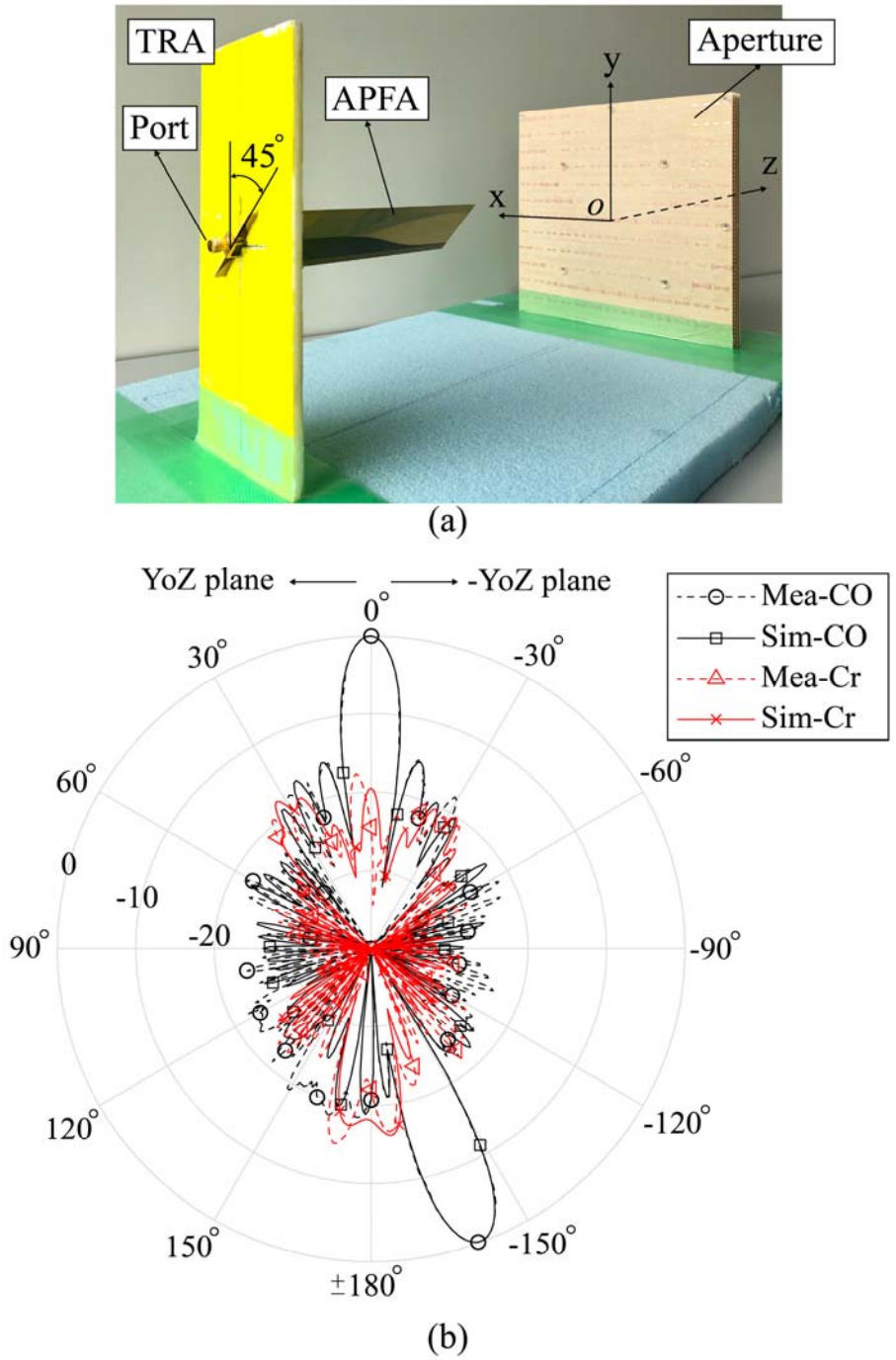

Figure 4-13 (a) Photograph of AUT for bidirectional verification. (b) Normalized radiation patterns in YoZ plane for both Co-Pol and Cr-Pol components at 10 GHz.

The functionalities of the antenna are determined by the incident polarization. Therefore, with circular- or tilted-polarized incidence, the antenna could exhibit simultaneously bidirectional performance in accordance with the superposition principle. To verify the capability, an additional experiment was carried out. The AUT model is shown in Figure 4-13 (a), where the source feed slants to $45°$. The polarizations of the forward and backward beams are both along x-axis. Therefore, in YoZ plane, the components of Co-Pol and Cr-Pol can be easily defined. The measured normalized radiation patterns in YoZ plane at 10 GHz are depicted in Figure 4-13 (b). Forward beam and backward beam with equal amplitude can be clearly observed.

4.4 Discussion and Summary

The proposed four-layer multifunctional unit cell was successfully applied to design single-feed transmit-reflect-combined-array antenna with expected forward and backward beams with features of being high efficiency, low-cost, and wideband. However, there are some points need to be pointed out:

1) Even with oblique beam direction of the reflectarray functionality in this case, the realized gain of reflectarray functionality (24 dBi @10 GHz) is little higher than that of transmitarray functionality (23.5 dBi @10 GHz). This is due to the more stable reflection phase responses of the element with oblique incidence.
2) The frequency shift phenomenon could be mitigated by carefully redesigning the H of the system configuration, as the H determines the inherent antenna system behavior.
3) The beam squint phenomenon of the reflectarray functionality could be mitigated by aligning the source feed to the specular direction of the outgoing beam.
4) By using a dual-polarized feed, the functionality of the antenna can be easily expanded to support multi-channel applications. Besides, the amplitudes of the forward and backward beams can be easily controlled by different slanting angle of the source feed.

Chapter 5

A Low-Cost and Reduced-Complexity Design Approach for Wideband Transmitarray Antenna

There are different techniques for designing wideband transmitarray antennas. These techniques were mentioned in Chapter 1. Although improved bandwidth can be obtained based on these techniques, they either surfer from complicated element structure [18, 25] or sophisticated optimization process [30, 31], leading to considerable design complexity and high fabrication cost. In this chapter, an efficient approach for designing wideband transmitarray antennas, which combines two different techniques—1-bit phase quantization and phase distribution optimization, is presented. The main advantages of this approach lie in its reduced complexity of the system design and unit cell, the simplicity of the fitness function and optimization loop, and the low-cost fabrication. First, a 1-bit unit cell with multiple $45°$-positioned parallel strip lines printed in the middle layer is designed and studied. The element demonstrates extremely wide 1-dB element bandwidth from 7.1-12.8 GHz. Then, considering the element performance, the phase distribution at multiple frequency points is optimized with modified weight at each frequency point to further balance the gain curve of the antenna system. The main core of the optimization is to redistribute the phases at all operating frequency points to not only ensure wideband performance but also reduce the effect of large phase errors caused by the 1-bit element as much as possible. To verify the effectiveness of the approach, a 13×17-element transmitarray antenna working at 10 GHz is designed, fabricated, and tested. 1-dB fractional realized gain bandwidth of 37% is achieved. The approach could be considered as a valid alternative

to obtain a wideband behavior of transmitarray antennas.

5.1 Wideband 1-Bit Transmitarray Antenna Design

The design procedure is composed of two steps—element design and system optimization. Then, a transmitarray antenna prototype is fabricated and tested to verify the design concept. These three aspects are separately discussed in the following.

5.1.1 Element Design

The 3-D perspective view of the unit cell in this chapter is shown in Figure 5-1 (a). The periodicity is $P = 15$ mm, which is equivalent to $0.5\lambda_0$@10 GHz. The upper layer and lower layer are the same two orthogonal grid polarizers used in Chapter 3 and 4, which work as perfect lens or reflector depending on the grid orientation. In the middle layer as shown in Figure 5-1 (b), five parallel strips with different lengths ($L_1 = 18$ mm, $L_2 = 12.5$ mm, $L_3 = 6.5$ mm) are printed in $45°$ with the same width of $w = 2$ mm and spacing of $d = 1$ mm. Besides, the air gaps between adjacent layers are 4 mm. The combined element forms a Fabry-Pérot-like cavity, and the underlying mechanism is based on interference theory presented in Chapter 2. The multiple strip lines in the middle layer forms a multi-resonant structure, consequently leading to wideband operation of the element.

The element performance under normal incidence is obtained by using periodic boundary condition-based full-wave solver, and can be fully characterized by the two matrix equations in equations 2-7~2-10. Moreover, the 1-bit phase quantization is achieved by simply mirroring the middle layer of the element, where the resulting top view is shown in Figure 5-1 (c). Figure 5-2 (a) and (b) show the magnitude and phase responses of component T_{xy}, respectively. The magnitude responses are identical for both phase-states, providing 1-dB element bandwidth from 7.1-12.8 GHz. Besides, the phase differences of $180°$ between the two phase-states are obtained over the entire

operation band.

Figure 5-3 depicts the frequency responses of other essential components. Components T_{yy} and R_{yy} are used here as the Cr-Pol level introduced by the element for transmitted and reflected fields, respectively. Under the condition of normal incidence, T_{yy} has a maximum level of -13 dB from 6-14 GHz, which reveals a high Co-Pol purity of the transmitted wave. As for R_{yy}, the high value occurring at edge frequency only affects the reflected wave. Therefore, both T_{yy} and R_{yy} have little effect on the Cr-Pol in the transmitarray main beam region. Furthermore, due to nearly 0 dB of $|R_{xx}|$, the Cr-Pol of the source feed also has little effect on the transmitted wave.

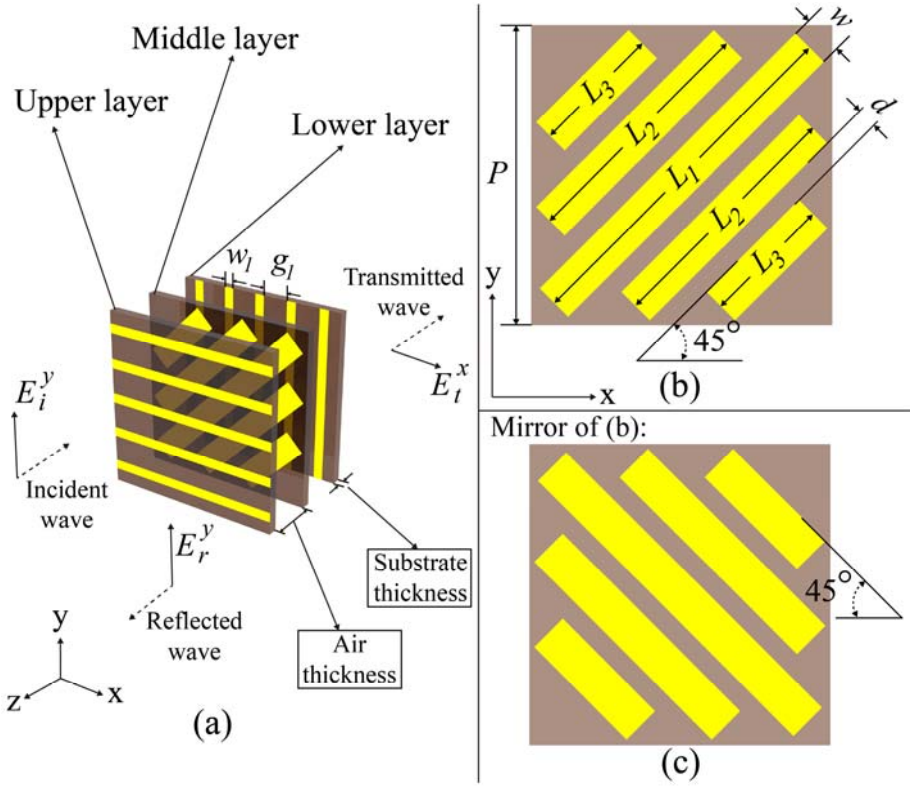

Figure 5-1 Unit cell view (a) 3-D view of the unit cell. (b) Middle layer of 0-bit element. (c) Middle layer of 1-bit element (Mirror of (b)). $L_1 = 18$, $L_2 = 12.5$, $L_3 = 6.5$, $w = 2$, $d = 1$, $w_1 = 0.8$, $g_1 = 2.2$, $air\_thickness = 4$, $substrate\_thickness = 0.8$ in mm.

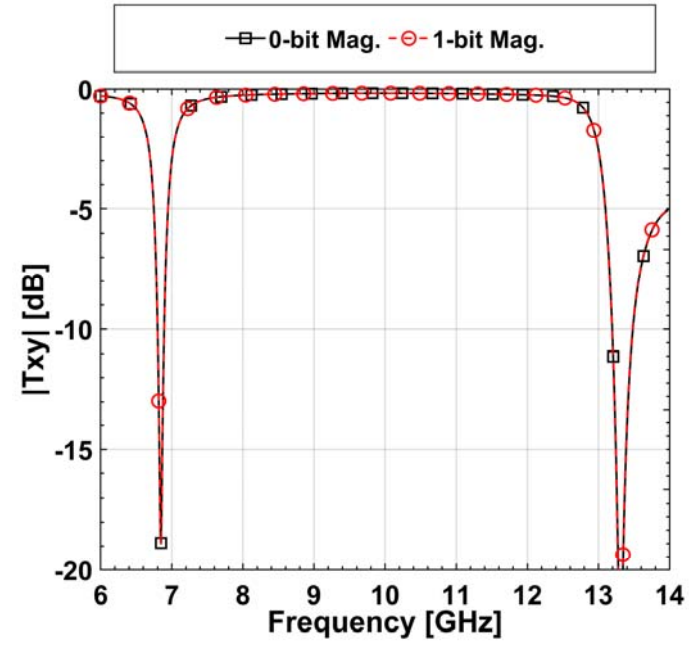

(a)

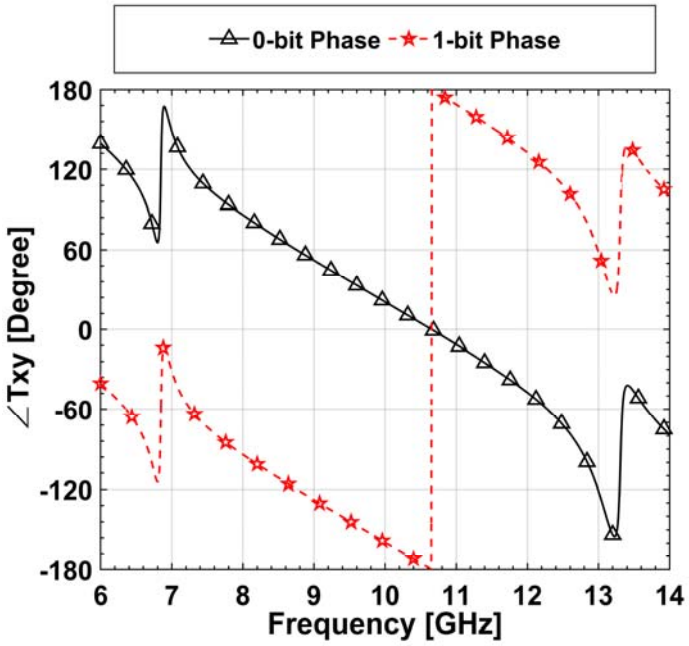

(b)

Figure 5-2 (a) $|T_{xy}|$ responses; (b) $\angle T_{xy}$ response.

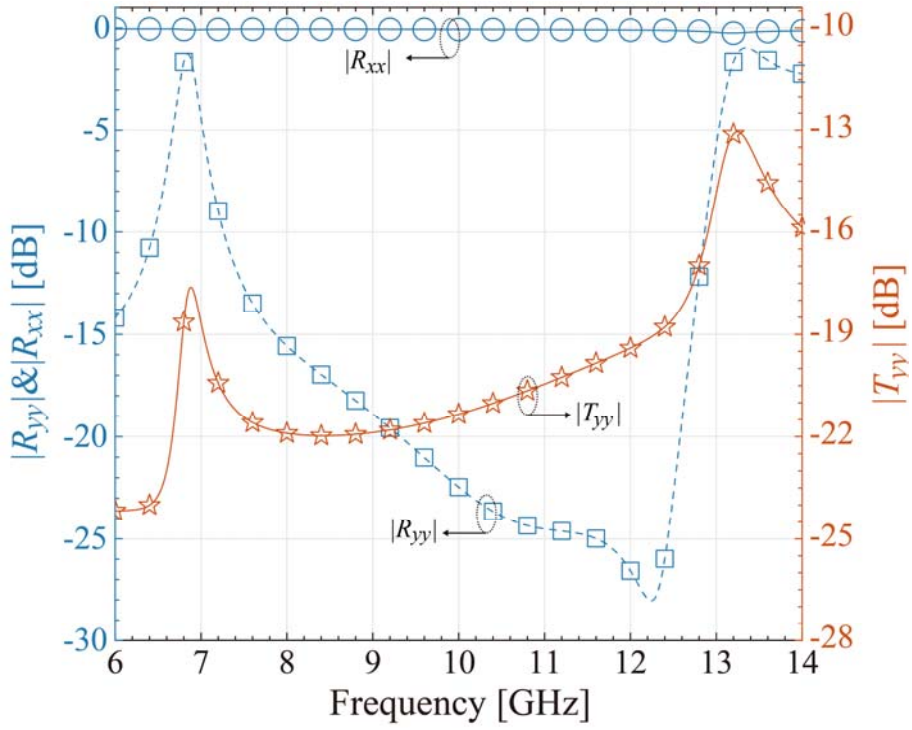

Figure 5-3 Frequency responses of other components R_{xx}, R_{yy}, T_{yy}.

5.1.2 System Configuration and Optimization

Figure 5-4 shows the antenna system configuration. In this chapter, a 195 mm × 255 mm rectangular aperture is introduced to match with the asymmetric radiation pattern provided by the source feed. The H (320 mm) is the same as in Chapter 3 and 4, providing edge center illumination taper of around -10 dB at 10 GHz. The antenna system performances in terms of spillover efficiency (S.E.), illumination efficiency (I.E.), and maximum aperture efficiency (Max A.E.) in this configuration are presented in Figure 5-5. On one hand, spillover efficiency (S.E.) is defined as:

$$\text{Spillover Efficiency} = \frac{\iint_A \vec{P}(\vec{r}_f)\cdot d\vec{S}}{\iint_S \vec{P}(\vec{r}_f)\cdot d\vec{S}} \tag{5-1}$$

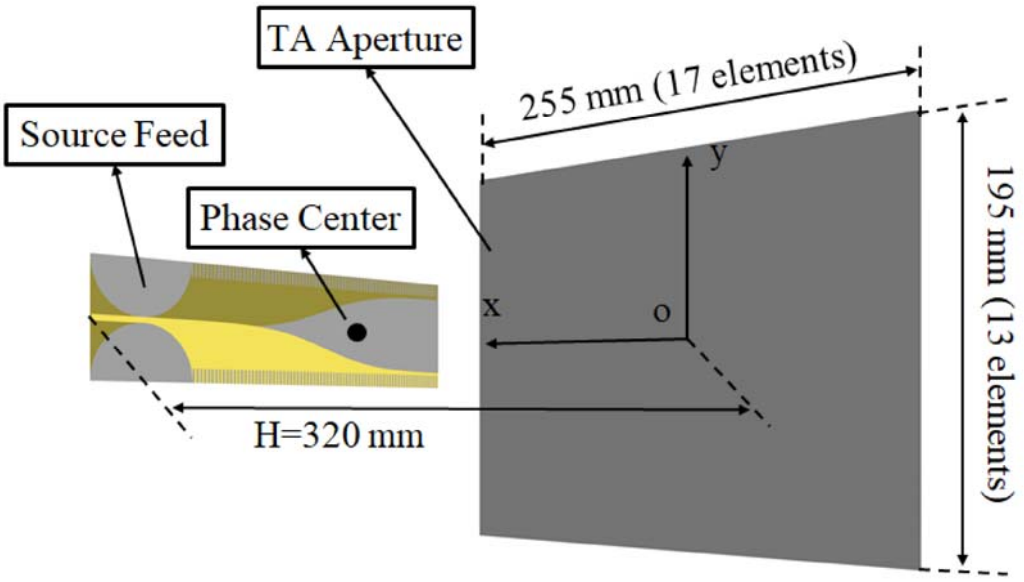

Figure 5-4 Antenna system configuration.

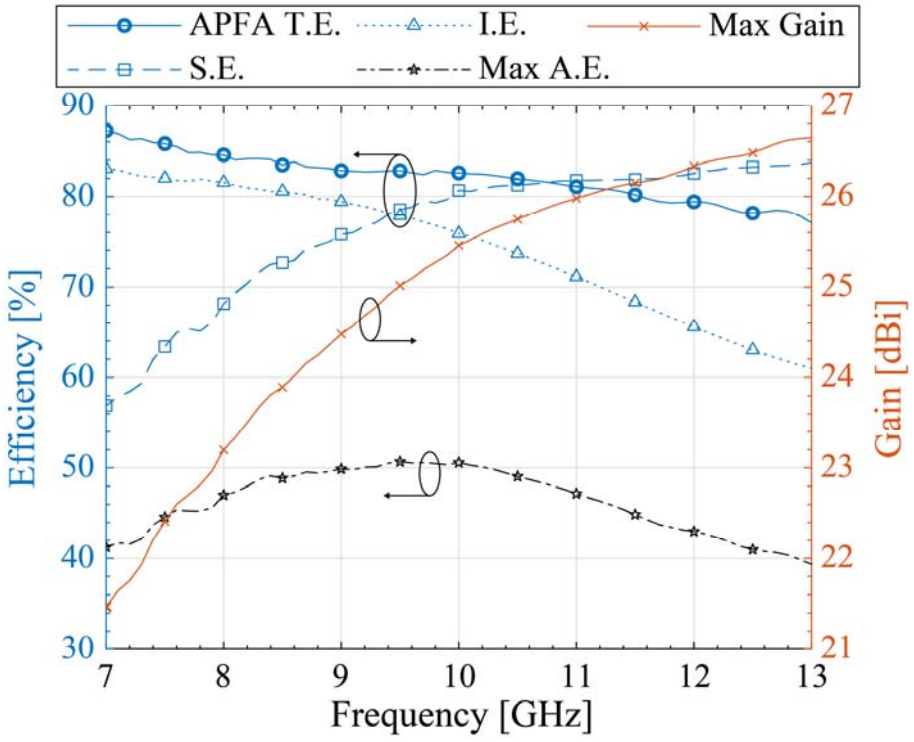

Figure 5-5 Ideal system performances in terms of APFA T.E., S.E., I.E., Max A.E., and Max Gain.

where both integrals are fluxes of the Poynting vector, $\vec{P}(\vec{r}_f)$, evaluated over certain surfaces. It represents the percentage of radiated power from the source feed that is intercepted by the aperture relative to the total radiated power. As depicted by square-marked line in Figure 5-5, spillover efficiency gradually increases with increasing frequency, which is mainly attributed to the increasing gain of the source feed. On the other hand, illumination efficiency (I.E.) is defined as:

$$\text{Illumination Efficiency} = \frac{1}{A} \cdot \frac{\left| \iint_A \left| I(A') \cdot dA' \right| \right|^2}{\iint_A \left| I(A') \right|^2 \cdot dA'} \tag{5-2}$$

denoting the efficiency due to nonuniform amplitude distribution over the aperture. Here $I(A')$ is the incident field distribution over the transmitarray aperture, A. As shown by the triangle-marked line in Figure 5-5, illumination efficiency declines as frequency rises. Meanwhile, the APFA T.E. in Figure 5-5 is the source feed total efficiency, and is repeated from Figure 2-2 (e). Max A.E. is defined as:

$$\text{Max A.E.} = \text{APFA T.E.} \times \text{S.E.} \times \text{I.E.} \tag{5-3}$$

representing the ideally achievable maximum aperture efficiency of this antenna system configuration. Typical arch-shaped curve is obtained, with maximum of 50.66% at 9.5 GHz. Considering the Max A.E., the max gain curve is also plotted in Figure 5-5. It should be pointed out that it represents the gain curve without any phase errors and loss over the entire band. Obviously, the ideal gain curve of the system demonstrates upward trend. In order to obtain flat gain response, which means wideband operation, phase errors are introduced at each frequency point in the form of 1-bit phase quantization. However, by deploying the 1-bit element in this chapter, large phase errors, even over

90° in some cases, appear, which degrade the antenna gain rapidly [89]. Therefore, in the case of ensuring wideband operation, it is of particular interest to avoid the effect of large phase errors as much as possible. This process is achieved by optimizing the phase distribution on the aperture.

As referred in [29, 90], the optimization algorithm is based on optimizing the reference phase for each frequency point and corresponding phase distribution over the aperture to minimize the weighted overall phase errors relative to all desired frequency points. The underlying core is to shift the elements with large phase errors to the edge region over the aperture, which belongs to the poorly illuminated zone. Besides, by properly defining the weight of each frequency point, weight-related different overall phase errors can be obtained over different frequencies, leading to flat gain response. Considering the increasing gain curve in Figure 5-5, flat gain response can be achieved by introducing larger/smaller overall phase errors in higher/lower frequency band.

The fitness function for single frequency point is described as:

$$\mathrm{cost}(f)=\sum_{mn} A_{mn}(f)\cdot\left|\psi_{mn}^{achievable}(f)-[-\psi_{mn}^{inc}(f)+c(f)]\right| \tag{5-4}$$

in which $A_{mn}(f)$ is the amplitude distribution of the incident field on the aperture at certain frequency point, $\psi_{mn}^{achievable}(f)$ denotes the achievable compensation phase value, $\psi_{mn}^{inc}(f)$ is the incident phase distribution on the aperture, and $c(f)$ is the constant reference phase. This fitness function takes into account the influence of nonuniform amplitude contribution on the radiation patterns. Based on this, the final wideband fitness function is defined as:

$$\mathrm{COST}=\sum_{f} a(f)\cdot\mathrm{cost}(f) \tag{5-5}$$

representing the weighted summation of the single frequency fitness functions. Here,

$a(f)$ is the weight at each frequency point, and the optimization variables are the reference phase at each frequency point.

Global-robust particle swarm optimization (PSO) is selected to implement the optimization loop. Besides, frequency points of 8, 9, 10, 11, 12 GHz are used to evaluate the loop, and the corresponding weights $a(f)$ is set to 0.3, 0.25, 0.2, 0.15, 0.1 to introduce less/more phase errors in low/high frequency band. It only takes 95 seconds on the laptop with Intel i5 processor and 8 GB memory to reach the convergence condition of the optimization process. The optimal results after the loop at each frequency point are $-178°$, $35°$, $-118°$, $93°$, $-53°$, respectively, and the corresponding overall phase error diagrams in different situations are plotted in Figure 5-6. Each diagram represents the phase errors experienced at certain frequency point under certain situation, and the single frequency optimization is evaluated only at 10 GHz. Compared with un-optimized case, the single frequency optimized case demonstrates less phase errors in center zone. Besides, for wideband optimization case, more overall phase errors are obtained in higher frequency band. Finally, the element arrangement of the middle layer is shown in Figure 5-7.

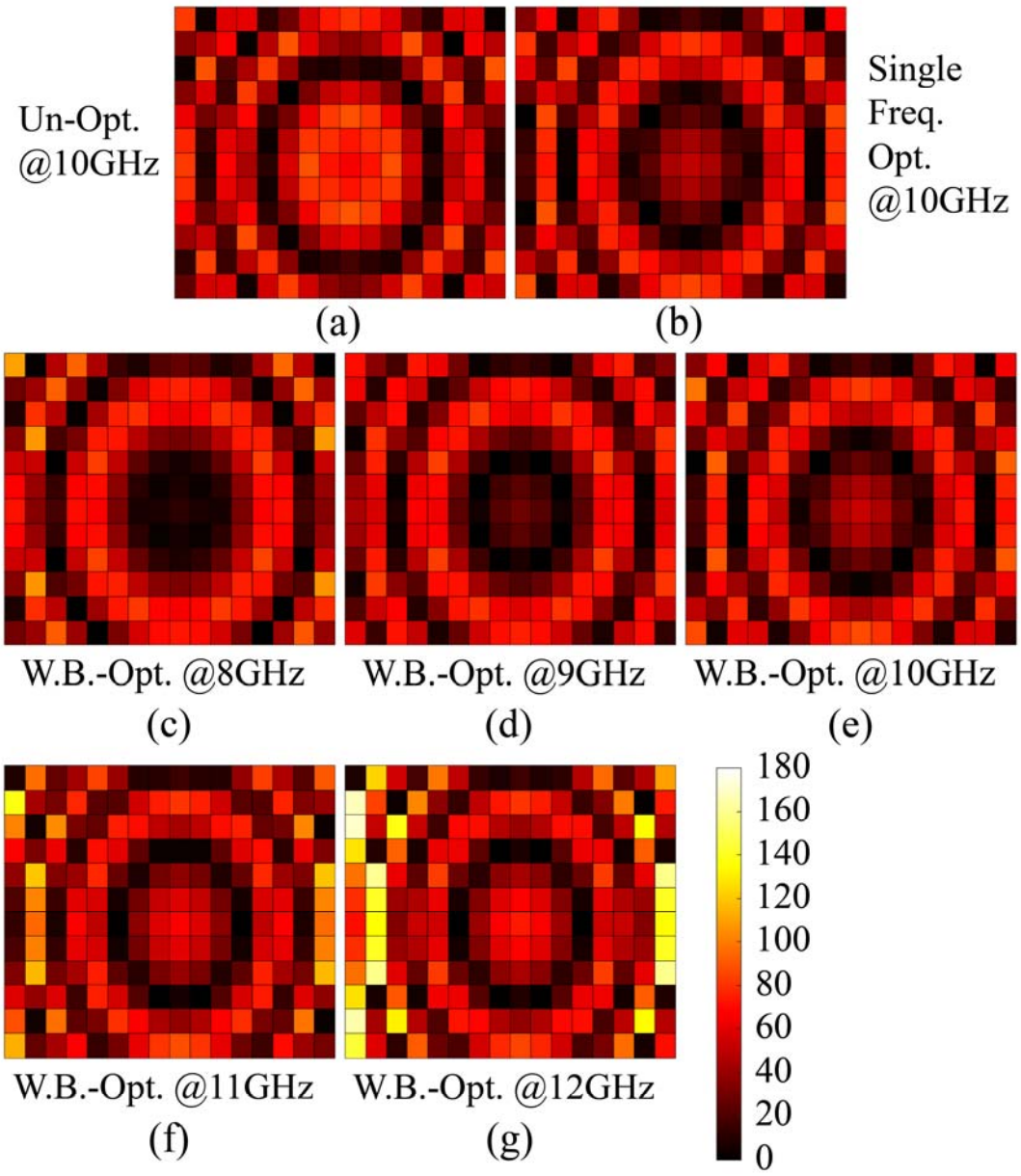

Figure 5-6 Phase error diagrams for (a) unoptimized @10GHz. (b) Single frequency point optimized @10GHz. (c) Wideband optimized @8GHz. (d) Wideband optimized @9GHz. (e) Wideband optimized @10GHz. (f) Wideband optimized @11GHz. (g) Wideband optimized @12GHz.

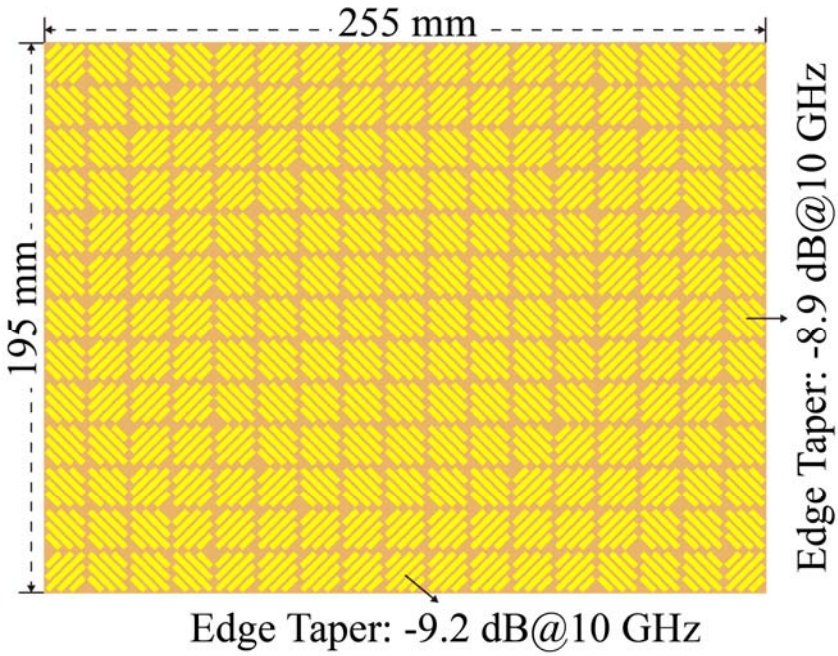

Figure 5-7 Final element arrangement in the middle layer.

5.1.3 Measurements

A 13 × 17-element antenna prototype was fabricated and tested. The photograph of the antenna under test model is shown in Figure 5-8. The measurements were carried out in anechoic chamber, with X-band standard gain horn as receiver. Besides, in this design, the E-plane is XoZ plane, while the H-plane is YoZ plane.

The normalized radiation patterns for both Co-Pol and Cr-Pol in E-/H-plane at 8.5 GHz, 10 GHz, and 12.2 GHz are given in Figure 5-9, where 8.5 GHz and 12.2 GHz represent the lower and upper frequency ends of the 1-dB realized gain bandwidth. High agreements between measured results and simulated results are obtained, especially in main beam and first SLL regions. The measured 3-dB beamwidthes in E-plane are 8°, 7.5°, and 6.9°, whereas those in H-plane are 9.7°, 9.3°, 8.5°, at 8.5 GHz, 10 GHz, and 12.2 GHz, respectively. Due to rectangular shape of the aperture, the beamwidths

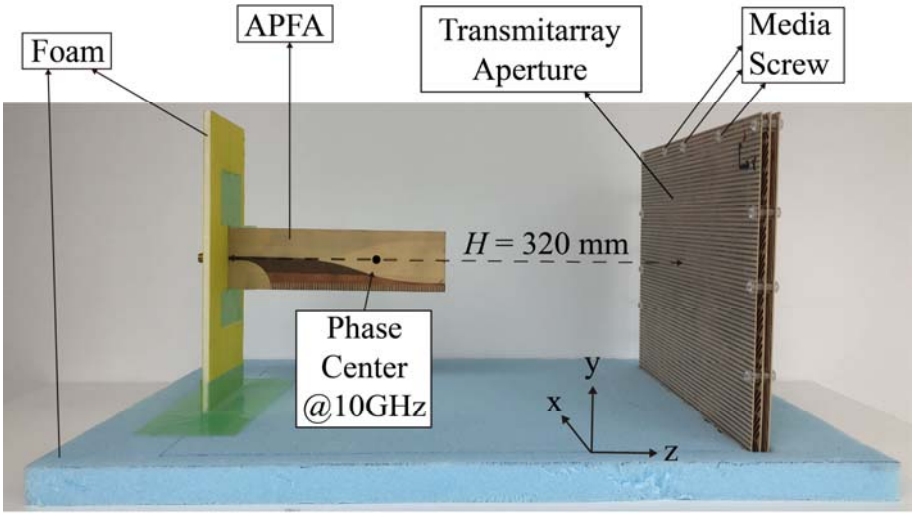

Figure 5-8 Photograph of the AUT.

in E-plane are reasonably narrower than those in H-plane. The realized gain responses in different cases are presented in Figure 5-10. Compared with the unoptimized case, the single frequency optimized case shows upward movement, which is mainly attributed to the shift of large phase error elements. Meanwhile, the 1-dB fractional gain bandwidth for unoptimized case is 26% (9-11.6 GHz). However, after the wideband optimization, the gain curve demonstrates flatter response, with slight increase in low band and decrease in high band. The measured results show reasonable agreement with simulated results, revealing 1-dB fractional realized gain bandwidth of 37%. Moreover, the measured 3-dB fractional realized gain bandwidth is 50%, corresponding to frequency band of 7.7-12.7 GHz. The aperture efficiency response is also plotted in Figure 5-10, with peak of 32% achieved at 8.4 GHz. It gradually decreases as frequency rises and relatively low aperture efficiency are suffered, especially at high frequency band, which is mainly caused by poorly illuminated aperture and large phase errors experienced. It should be mentioned that unlike the true-time-delay design [18, 19, 21, 25], where different slopes of element phase responses are required, the wideband mechanism in this design is based on introducing phase errors and redistributing the phase errors at all desired frequencies, leading to flat gain response over a wide band on a certain degree. The antenna system performances in terms of loss factors at 10 GHz are summarized in Table 5-1.

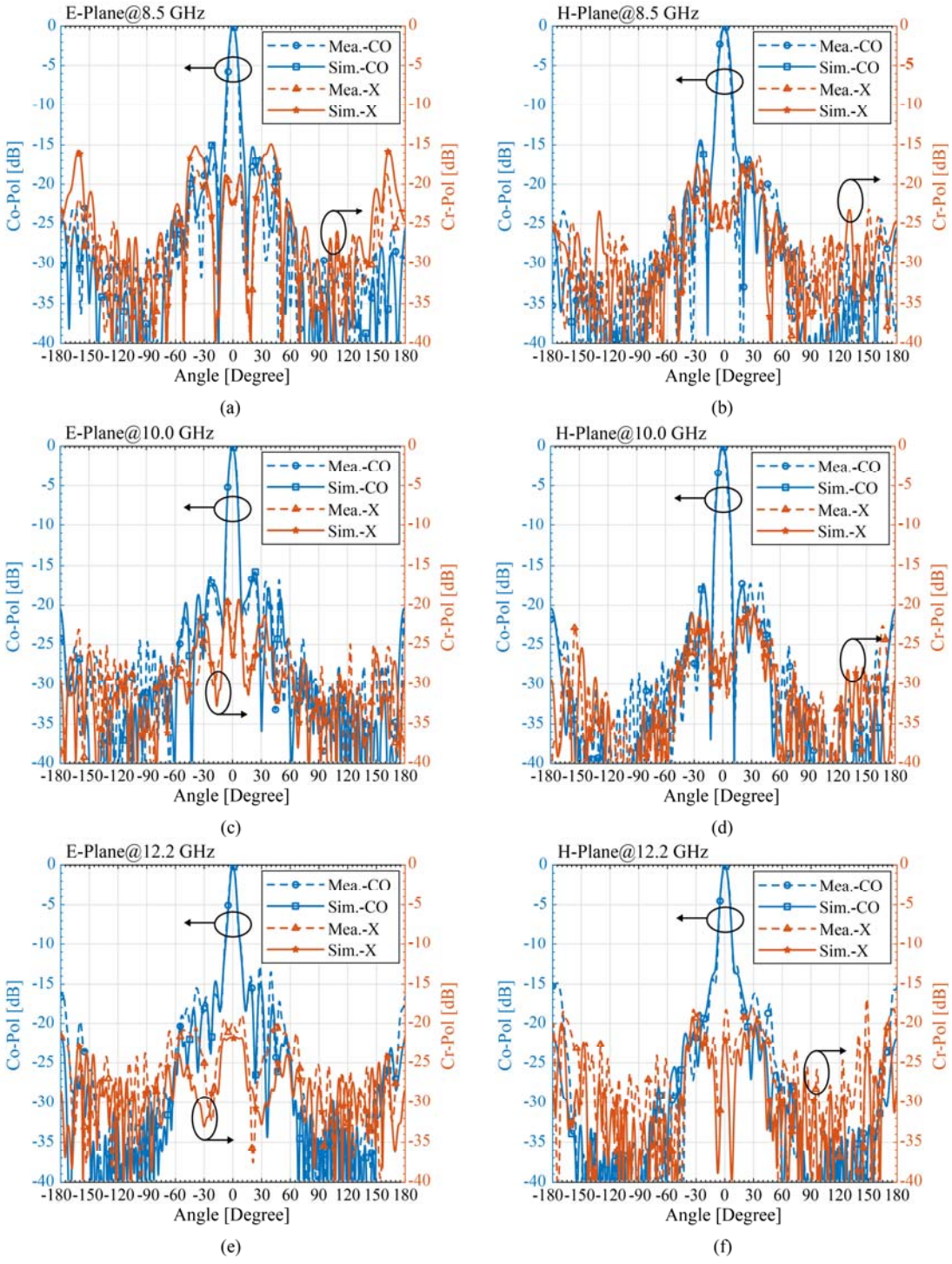

Figure 5-9 Normalized radiation patterns (a) E-plane @8.5GHz. (b) H-plane @8.5GHz. (c) E-plane @10GHz. (d) H-plane @10GHz. (e) E-plane @12.2GHz. (f) H-plane @12.2GHz.

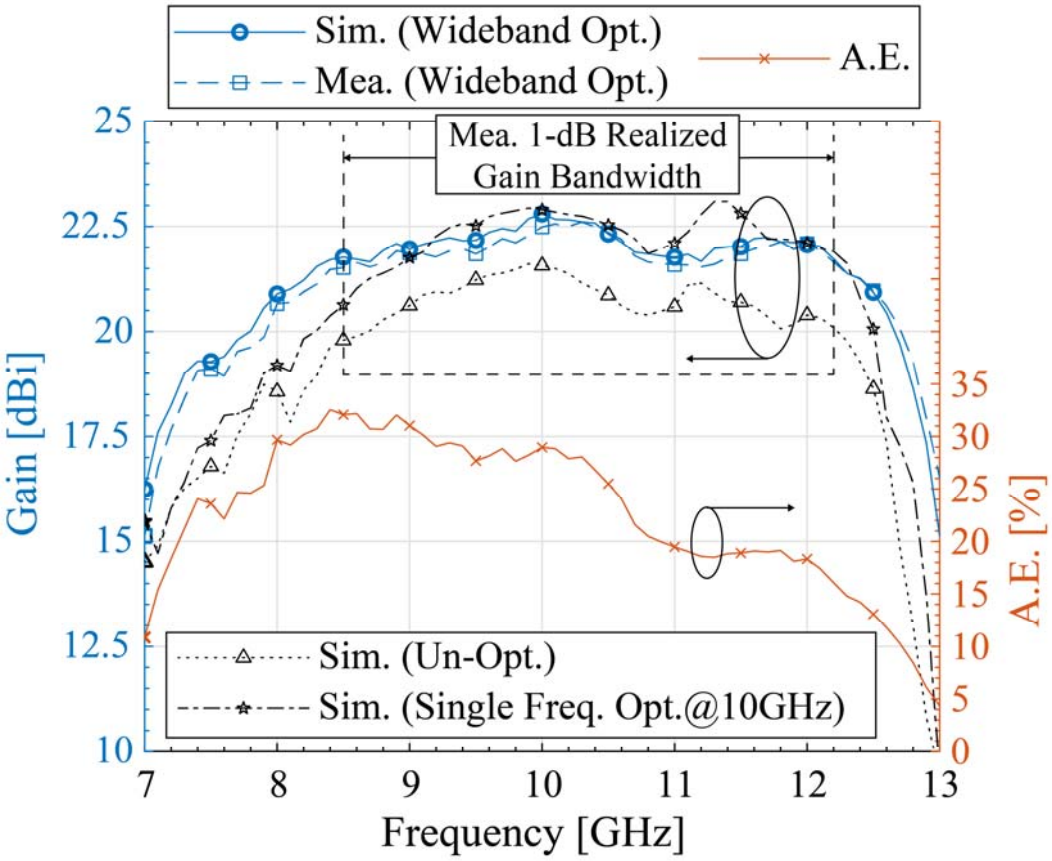

Figure 5-10 Gain responses and aperture efficiency responses

TABLE 5-1
GAIN TABLE AT 10 GHZ

Ideal Directivity	28.42 dBi
APFA T.E. Loss	0.83 dB
S.E. Loss	0.93 dB
I.E. Loss	1.20 dB
Achievable Max. A.E.	50.56%
Achievable Max. Gain	25.45 dBi
Phase Error Loss	2.65 dB
Measured Gain	22.49 dBi
A.E.	25.55%

5.2 Discussion and Summary

In this chapter, a wideband transmitarray antenna was successfully designed by using the proposed approach, which has the features of being low-cost and reduced-complexity. However, there are some points need to be pointed out:

1) By using this approach, the wideband operation of the transmitarray antenna is obtained by sacrificing the aperture efficiency. Therefore, this approach could only be a valid alternative to obtain a wideband behavior.
2) The phase response slope of the element obtained in this chapter is not the optimal one. In other words, by carefully redesigning the phase slope of the element, the aperture efficiency of the antenna system could be enhanced, as the overall phase errors of the system could be reduced.
3) The main focus of the optimization in this chapter is to maintain the antenna efficiency on an acceptable level, that is, to avoid significant efficiency loss caused by the 1-bit phase quantization. However, if the antenna efficiency is not under consideration, the gain bandwidth could be further increased at the cost of the decreased efficiency. This could be achieved by redesigning the phase slope of the element.

Chapter 6

Conclusion

This work covers several major topics required to be tackled and investigated on transmitarray antennas with enhanced performance and expanded functionalities. Research has been conducted on both unit cell and full transmitarray levels. Several novel designs have been proposed and detailed design procedures have been presented. Some experiments have been performed to validate the designs.

This dissertation is divided into 6 chapters.

Chapter 1 is a general introduction. The background and the motivation of this research have been presented.

In chapter 2, general theory and analysis methods of transmitarray antennas used in this dissertation have been presented at component and system levels. At component level, firstly, comprehensive performances of the source feed have been presented. Then, the underlying operation principle of the transmitarray elements with Fabry-Pérot-like cavity and the generalized scattering matrix-based analysis approach have been discussed. These have provided valuable inspiration for the transmitarray elements developed in the following chapters. At system level, firstly, the determination of the phase distribution and element arrangement on the transmitarray aperture have been given. Then, array factor approach for computing radiation pattern of transmitarray antennas has been discussed in detail.

In chapter 3, beam-shaping transmitarray antennas have been investigated at unit cell and array synthesis levels. At unit cell level, based on the principle of Fabry-Pérot-like cavity, a three-layer transmitarray element with shaped-dipole structure in the middle layer sandwiched by two orthogonal grid polarizers has been developed. This element is capable of controlling both amplitude and phase of the transmission

coefficient, which is rarely reported before in the field of transmitarray element. Compared with the existing designs, full-coverage of transmission coefficient is achieved due to the flexible control of interference inside the element. At array synthesis level, particle swarm optimization algorithm is used to determine the element distribution on the transmitarray aperture for required shaped beam. Transmission amplitude control has been taken into account during the synthesis process, which is rarely considered before in the field of transmitarray synthesis. The above transmitarray element design and transmitarray synthesis are concluded as amplitude-phase synthesis method. Based on the method, a small-sized transmitarray antenna with both amplitude and phase control has been designed, fabricated, and tested. Numerical and experimental results have revealed that the transmitarray antenna based on the amplitude-phase synthesis method achieves better performance in terms of beam-shaping quality, compared to the one designed by the conventional phase-only synthesis technique. The transmitarray antenna based on the phase-only synthesis method cannot form the expected radiation pattern even in main beam region.

In chapter 4, single-feed multifunctional transmit-reflect-combined-array antennas have been studied. Inspired from the element in chapter 3, a four-layer polarization-dependent multifunctional unit cell with one more bowtie layer inserted has been developed. The unit cell provides feature of simultaneous controls of transmission phase and reflection phase by discriminating in incident polarization. The unit cell has achieved better performances in terms of phase linearity, stability under oblique incidence, and completely decoupled control than the existing designs in transmit-reflect-combined-array unit cell. Based on the unit cell, a novel single-feed transmit-reflect-combined-array antenna working in X-band has been designed, fabricated, and tested. Simulated and measured results have demonstrated that the proposed antenna achieves better performances in terms of aperture efficiency, flexibility, and bandwidth than the existing designs in transmit-reflect-combined-array antennas.

In chapter 5, wideband transmitarray antennas have been investigated. A new design approach is developed to design wideband transmitarray antennas in a low-cost

and reduced-complexity manner. The design approach combines two different techniques—1-bit phase quantization and phase distribution optimization. Firstly, by replacing the middle layer of the element in chapter 3 to a multiple 45°-positioned parallel strip lines printed layer, a three-layer polarization-rotation 1-bit element is developed. The element has demonstrated extremely wide 1-dB bandwidth, and is used to introduce phase error on the transmitarray aperture to balance the gain behavior of the entire system. It is the first time to use phase error as one kind of degree-of-freedom to design wideband transmitarray antennas. Then, an optimization is performed to redistribute the phase errors on the aperture at all operating frequency points. It aims to not only ensure wideband performance of the antenna system but also reduce the effect of large phase errors caused by the 1-bit element as much as possible. The underlying core is to shift the elements with large phase error to the edge region, which belongs to the poor illuminated zone. The proposed design approach has been validated through the fabrication and test of a $6.5\lambda_0 \times 8.5\lambda_0$ transmitarray antenna at X-band. Numerical and experimental results have demonstrated that wideband operation of transmitarray antenna is achieved in a less cost and less design complexity manner than the existing design approaches.

This research has contributed greatly in the field of transmitarray antennas, with particular emphasis on analyzing and designing transmitarray antennas with enhanced performance and expanded functionalities. It is no doubt that the results from this dissertation will benefit the design and improvement of the transmitarray antennas.

References

[1] Ahmed H. Abdelrahman, F. Yang, Atef Z. Elsherbeni, and Payam Nayeri, *Analysis and Design of Transmitarray Antennas*: Morgan & Claypool, 2017.

[2] A. H. Abdelrahman, "Critical analysis of transmitarray antenna design," Ph.D. dissertation, Department of Electrocal Engineering, The University of Mississippi, Ann Arbor, Michigan, 2014.

[3] H. Nematollahi, J. Laurin, M. Barba, and J. A. Encinar, "Realization of Focused Beam and Shaped Beam Transmitarrays Based on Broadband Unit Cells," *IEEE Transactions on Antennas and Propagation,* vol. 65, no. 8, pp. 4368-4373, Aug. 2017.

[4] O. M. Bucci, G. Franceschetti, G. Mazzarella, and G. Panariello, "Intersection approach to array pattern synthesis," *IEE Proceedings H - Microwaves, Antennas and Propagation,* vol. 137, no. 6, pp. 349-357, Dec. 1990.

[5] O. M. Bucci, G. Mazzarella, and G. Panariello, "Reconfigurable arrays by phase-only control," *IEEE Transactions on Antennas and Propagation,* vol. 39, no. 7, pp. 919-925, Jul. 1991.

[6] A. H. Abdelrahman, P. Nayeri, A. Z. Elsherbeni, and F. Yang, "Single-Feed Quad-Beam Transmitarray Antenna Design," *IEEE Transactions on Antennas and Propagation,* vol. 64, no. 3, pp. 953-959, Mar. 2016.

[7] J. Robinson, and Y. Rahmat-Samii, "Particle swarm optimization in electromagnetics," *IEEE Transactions on Antennas and Propagation,* vol. 52, no. 2, pp. 397-407, Feb. 2004.

[8] D. W. Boeringer, and D. H. Werner, "Particle swarm optimization versus genetic algorithms for phased array synthesis," *IEEE Transactions on Antennas and Propagation,* vol. 52, no. 3, pp. 771-779, Mar. 2004.

[9] N. Gagnon, A. Petosa, and D. A. McNamara, "Electrically thin free-standing phase and amplitude shifting surface for beam shaping applications,"

Microwave and Optical Technology Letters, vol. 54, no. 7, pp. 1566-1571, Jul. 2012.

[10] M. Martone, P. Rizzoli, and G. Krieger, "Volume Decorrelation Effects in TanDEM-X Interferometric SAR Data," *IEEE Geoscience and Remote Sensing Letters,* vol. 13, no. 12, pp. 1812-1816, Dec. 2016.

[11] F. Fuschini, and G. Falciasecca, "A Mixed Rays—Modes Approach to the Propagation in Real Road and Railway Tunnels," *IEEE Transactions on Antennas and Propagation,* vol. 60, no. 2, pp. 1095-1105, Feb. 2012.

[12] R. Wang, B.-Z. Wang, X. Ding, and J.-Y. Ou, "Planar array with bidirectional elements for tunnel environments," *Scientific Reports,* vol. 7, no. 1, pp. 15421, Nov. 2017.

[13] F. Yang, R. Deng, S. Xu, and M.-K. Li, "Design and Experiment of a Near-Zero-Thickness High-Gain Transmit-Reflect-Array Antenna Using Anisotropic Metasurface," *IEEE Transactions on Antennas and Propagation,* vol. 66, no. 6, pp. 2853-2861, Jun. 2018.

[14] T. Cai, G.-M. Wang, X.-L. Fu, J.-G. Liang, and Y.-Q. Zhuang, "High-Efficiency Metasurface With Polarization-Dependent Transmission and Reflection Properties for Both Reflectarray and Transmitarray," *IEEE Transactions on Antennas and Propagation,* vol. 66, no. 6, pp. 3219-3224, Jun. 2018.

[15] X.-J. Zhong, H.-X. Xu, L. Chen, W.-T. Li, H. Wang, and X.-W. Shi, "An FSS-Backed Broadband Phase-Shifting Surface Array With Multimode Operation," *IEEE Transactions on Antennas and Propagation,* vol. 67, no. 9, pp. 5974-5981, Sep. 2019.

[16] Q. Cheng, H. F. Ma, and T. J. Cui, "Broadband planar Luneburg lens based on complementary metamaterials," *Applied Physics Letters,* vol. 95, no. 18, pp. 181901, Nov. 2009.

[17] M. N. Jazi, M. R. Chaharmir, J. Shaker, and A. R. Sebak, "Broadband Transmitarray Antenna Design Using Polarization-Insensitive Frequency Selective Surfaces," *IEEE Transactions on Antennas and Propagation,* vol. 64,

no. 1, pp. 99-108, Jan. 2016.

[18] M. Li, M. A. Al-Joumayly, and N. Behdad, "Broadband True-Time-Delay Microwave Lenses Based on Miniaturized Element Frequency Selective Surfaces," *IEEE Transactions on Antennas and Propagation,* vol. 61, no. 3, pp. 1166-1179, Mar. 2013.

[19] E. B. Lima, S. A. Matos, J. R. Costa, C. A. Fernandes, and N. J. G. Fonseca, "Circular Polarization Wide-Angle Beam Steering at Ka-Band by In-Plane Translation of a Plate Lens Antenna," *IEEE Transactions on Antennas and Propagation,* vol. 63, no. 12, pp. 5443-5455, Dec. 2015.

[20] K. Pham, N. T. Nguyen, A. Clemente, L. D. Palma, L. L. Coq, L. Dussopt, and R. Sauleau, "Design of Wideband Dual Linearly Polarized Transmitarray Antennas," *IEEE Transactions on Antennas and Propagation,* vol. 64, no. 5, pp. 2022-2026, May 2016.

[21] S. A. Matos, E. B. Lima, J. S. Silva, J. R. Costa, C. A. Fernandes, N. J. G. Fonseca, and J. R. Mosig, "High Gain Dual-Band Beam-Steering Transmit Array for Satcom Terminals at Ka-Band," *IEEE Transactions on Antennas and Propagation,* vol. 65, no. 7, pp. 3528-3539, Jul. 2017.

[22] B. Rahmati, and H. R. Hassani, "High-Efficient Wideband Slot Transmitarray Antenna," *IEEE Transactions on Antennas and Propagation,* vol. 63, no. 11, pp. 5149-5155, Nov. 2015.

[23] A. H. Abdelrahman, A. Z. Elsherbeni, and F. Yang, "High-Gain and Broadband Transmitarray Antenna Using Triple-Layer Spiral Dipole Elements," *IEEE Antennas and Wireless Propagation Letters,* vol. 13, pp. 1288-1291, Jul. 2014.

[24] B. Rahmati, and H. R. Hassani, "Low-Profile Slot Transmitarray Antenna," *IEEE Transactions on Antennas and Propagation,* vol. 63, no. 1, pp. 174-181, Jan. 2015.

[25] Y.-M. Cai, W.-T. Li, K. Li, S. Gao, Y.-Z. Yin, L.-Y. Zhao, and W. Hu, "A Novel Ultrawideband Transmitarray Design Using Tightly Coupled Dipole Elements," *IEEE Transactions on Antennas and Propagation,* vol. 67, no. 1, pp. 242-250,

Jan. 2019.

[26] Y. Zhang, R. Mittra, and W. Hong, “On the Synthesis of a Flat Lens using a Wideband Low-Reflection Gradient-Index Metamaterial,” *Journal of Electromagnetic Waves and Applications,* vol. 25, no. 16, pp. 2178-2187, Jan. 2011.

[27] A. H. Abdelrahman, A. Z. Elsherbeni, and F. Yang, “Transmitarray Antenna Design Using Cross-Slot Elements With No Dielectric Substrate,” *IEEE Antennas and Wireless Propagation Letters,* vol. 13, pp. 177-180, Jan. 2014.

[28] Q. Luo, S. Gao, M. Sobhy, and X.-X. Yang, “Wideband Transmitarray With Reduced Profile,” *IEEE Antennas and Wireless Propagation Letters,* vol. 17, no. 3, pp. 450-453, Mar. 2018.

[29] A. H. Abdelrahman, P. Nayeri, A. Z. Elsherbeni, and F. Yang, “Bandwidth Improvement Methods of Transmitarray Antennas,” *IEEE Transactions on Antennas and Propagation,* vol. 63, no. 7, pp. 2946-2954, Jul. 2015.

[30] P. Feng, S. Qu, and S. Yang, “Octave Bandwidth Transmitarrays With a Flat Gain,” *IEEE Transactions on Antennas and Propagation,* vol. 66, no. 10, pp. 5231-5238, Oct. 2018.

[31] P. Feng, S. Qu, and S. Yang, “Ultrawideband Low-Profile Transmitarray With Vivaldi Array Feed,” *IEEE Transactions on Antennas and Propagation,* vol. 68, no. 4, pp. 3265-3270, Apr. 2020.

[32] A. Clemente, L. Dussopt, R. Sauleau, P. Potier, and P. Pouliguen, “1-Bit Reconfigurable Unit Cell Based on PIN Diodes for Transmit-Array Applications in X-Band,” *IEEE Transactions on Antennas and Propagation,* vol. 60, no. 5, pp. 2260-2269, May 2012.

[33] J. Y. Lau, and S. V. Hum, “Analysis and Characterization of a Multipole Reconfigurable Transmitarray Element,” *IEEE Transactions on Antennas and Propagation,* vol. 59, no. 1, pp. 70-79, Jan. 2011.

[34] M. Frank, F. Lurz, R. Weigel, and A. Koelpin, “Electronically Reconfigurable 6 × 6 Element Transmitarray at K-Band Based on Unit Cells With Continuous

Phase Range," *IEEE Antennas and Wireless Propagation Letters,* vol. 18, no. 4, pp. 796-800, Apr. 2019.

[35] P. Padilla, A. Muñoz-Acevedo, M. Sierra-Castañer, and M. Sierra-Pérez, "Electronically Reconfigurable Transmitarray at Ku Band for Microwave Applications," *IEEE Transactions on Antennas and Propagation,* vol. 58, no. 8, pp. 2571-2579, Aug. 2010.

[36] J. Y. Lau, and S. V. Hum, "A Planar Reconfigurable Aperture With Lens and Reflectarray Modes of Operation," *IEEE Transactions on Microwave Theory and Techniques,* vol. 58, no. 12, pp. 3547-3555, Dec. 2010.

[37] J. Y. Lau, and S. V. Hum, "Reconfigurable Transmitarray Design Approaches for Beamforming Applications," *IEEE Transactions on Antennas and Propagation,* vol. 60, no. 12, pp. 5679-5689, Dec. 2012.

[38] A. Clemente, L. Dussopt, R. Sauleau, P. Potier, and P. Pouliguen, "Wideband 400-Element Electronically Reconfigurable Transmitarray in X Band," *IEEE Transactions on Antennas and Propagation,* vol. 61, no. 10, pp. 5017-5027, Oct. 2013.

[39] J. Y. Lau, and S. V. Hum, "A Wideband Reconfigurable Transmitarray Element," *IEEE Transactions on Antennas and Propagation,* vol. 60, no. 3, pp. 1303-1311, Mar. 2012.

[40] T. Jiang, Z.-Y Wang, D. Li, J.-N. Pan, B. Zhang, J.-T. Huangfu, Y. Salamin, C.-Z. Li, and L.-X. Ran, "Low-DC Voltage-Controlled Steering-Antenna Radome Utilizing Tunable Active Metamaterial," *IEEE Transactions on Microwave Theory and Techniques,* vol. 60, no. 1, pp. 170-178, Jan. 2012.

[41] Y. Sun, Z. Li, W. Zhu, Z. Ji, and Q. Wang, "New steerable antenna with controllable metamaterial," in *Proceedings of the 42nd European Microwave Conference*, 2012, pp. 936-939.

[42] M. Maasch, M. Roig, C. Damm, and R. Jakoby, "Voltage-Tunable Artificial Gradient-Index Lens Based on a Liquid Crystal Loaded Fishnet Metamaterial," *IEEE Antennas and Wireless Propagation Letters,* vol. 13, pp. 1581-1584, Aug.

2014.

[43] W. Pan, C. Huang, P. Chen, M. Pu, X. Ma, and X. Luo, “A Beam Steering Horn Antenna Using Active Frequency Selective Surface,” *IEEE Transactions on Antennas and Propagation,* vol. 61, no. 12, pp. 6218-6223, Dec. 2013.

[44] M. Sazegar, Y. Zheng, C. Kohler, H. Maune, M. Nikfalazar, J. R. Binder, and R. Jakoby, “Beam Steering Transmitarray Using Tunable Frequency Selective Surface With Integrated Ferroelectric Varactors,” *IEEE Transactions on Antennas and Propagation,* vol. 60, no. 12, pp. 5690-5699, Dec. 2012.

[45] J. R. Reis, R. F. S. Caldeirinha, A. Hammoudeh, and N. Copner, “Electronically Reconfigurable FSS-Inspired Transmitarray for 2-D Beamsteering,” *IEEE Transactions on Antennas and Propagation,* vol. 65, no. 9, pp. 4880-4885, Sep. 2017.

[46] J. R. Reis, N. Copner, A. Hammoudeh, Z. M.-E. Al-Daher, R. F. S. Caldeirinha, T. R. Fernandes, and R. Gomes, “FSS-Inspired Transmitarray for Two-Dimensional Antenna Beamsteering,” *IEEE Transactions on Antennas and Propagation,* vol. 64, no. 6, pp. 2197-2206, Jun. 2016.

[47] L. Boccia, I. Russo, G. Amendola, and G. D. Massa, “Multilayer Antenna-Filter Antenna for Beam-Steering Transmit-Array Applications,” *IEEE Transactions on Microwave Theory and Techniques,* vol. 60, no. 7, pp. 2287-2300, Jul. 2012.

[48] B. D. Nguyen, and C. Pichot, “Unit-Cell Loaded With PIN Diodes for 1-Bit Linearly Polarized Reconfigurable Transmitarrays,” *IEEE Antennas and Wireless Propagation Letters,* vol. 18, no. 1, pp. 98-102, Jan. 2019.

[49] M. Sato, H. Sato, T. Hirose, H. Kobayashi, K. Sawaya, and K. Mizuno, “Antipodal LTSA with Corrugation for 94-GHz band Passive Millimeter-wave Imager,” in *Proceedings of Asia-Pacific Microwave Conference 2007*, 2007, pp. 1-4.

[50] H. Sato, K. Sawaya, N. Arai, Y. Wagatsuma, and K. Mizuno, “Broadband FDTD analysis of Fermi antenna with narrow width substrate,” in *IEEE Antennas and Propagation Society International Symposium*, 2003, pp. 261-264.

[51] H. Sato, K. Sawaya, Y. Wagatsuma, and K. Mozuno, “Broadband FDTD design of Fermi antenna for passive millimeter wave imaging, ” in *2005 IEEE International Symposium on Microwave, Antenna, Propagation and EMC Technologies for Wireless Communications Proceedings*, 2005, pp. 123-126.

[52] S. Sugawara, Y. Maita, K. Adachi, K. Mori, and K. Mizuno, “Characteristics of a MM-wave tapered slot antenna with corrugated edges, ” in *1998 IEEE MTT-S International Microwave Symposium*, 1998, pp. 533-536.

[53] H. Sato, K. Sawaya, Y. Wagatsuma, and K. Mizuno, “Design of narrow-width Fermi antenna with circular radiation pattern, ” in *IEEE Antennas and Propagation Society Symposium*, 2004, pp. 4312-4315 Vol.4.

[54] H. Sato, Y. Murakami, K. Sawaya, and K. Mizuno, “FDTD analysis of 81-element antipodal Fermi antenna array with axially symmetric array element pattern, ” in *2008 IEEE Antennas and Propagation Society Internatioanl Symposium*, 2008, pp. 1-4.

[55] H. Sato, Y. Takagi, and K. Sawaya, “High Gain Antipodal Fermi Antenna with Low Cross Polarization,” *IEICE Transactions on Communications,* vol. E94.B, no. 8, pp. 2292-2297, Aug. 2011.

[56] S. Sugawara, Y. Maita, K. Adachi, K. Mori, K. Mizuno, “A mm-wave tapered slot antenna with improved radiation pattern, ” in *1997 IEEE MTT-S International Microwave Symposium*, 1997, pp. 959-962 vol.2.

[57] H. Y. Yao, N. C. Chen, T. H. Chang, and H. G. Winful, “Frequency-dependent cavity lifetime and apparent superluminality in Fabry-Pérot-like interferometers,” *Physical Review A,* vol. 86, no. 5, pp. 053832, Nov. 2012.

[58] N. K. Grady, J. E. Heyes, D. R. Chowdhury, Y. Zeng, M. T. Reiten, A. K. Azad, A. J. Taylor, D. A. R. Dalvit, and H.-T. Chen, “Terahertz Metamaterials for Linear Polarization Conversion and Anomalous Refraction,” *Science,* vol. 340, no. 6138, pp. 1304, Jun. 2013.

[59] H. Yao, N. C. Chen, T. Chang, and H. G. Winful, “Tunable Negative Group Delay in a Birefringent Fabry–Pérot-Like Cavity With High Fractional

Advancement Induced by Cross-Interference Effect," *IEEE Transactions on Microwave Theory and Techniques,* vol. 64, no. 10, pp. 3121-3130, Oct. 2016.

[60] P. Gay-Balmaz, J. A. Encinar, and J. R. Mosig, "Analysis of multilayer printed arrays by a modular approach based on the generalized scattering matrix," *IEEE Transactions on Antennas and Propagation,* vol. 48, no. 1, pp. 26-34, Jan. 2000.

[61] W. Changhua, and J. A. Encinar, "Efficient computation of generalized scattering matrix for analyzing multilayered periodic structures," *IEEE Transactions on Antennas and Propagation,* vol. 43, no. 11, pp. 1233-1242, Nov. 1995.

[62] J. Huang and J. A. Encinar, *Reflectarray Antenna*: John Wiley & Sons, 2007.

[63] R. Mittra, C. H. Chan, and T. Cwik, "Techniques for analyzing frequency selective surfaces-a review," *Proceedings of the IEEE,* vol. 76, no. 12, pp. 1593-1615, Dec. 1988.

[64] S. H. R. Tuloti, P. Rezaei, and F. T. Hamedani, "High-Efficient Wideband Transmitarray Antenna," *IEEE Antennas and Wireless Propagation Letters,* vol. 17, no. 5, pp. 817-820, May 2018.

[65] P. Padilla, A. Muñoz-Acevedo, and M. Sierra-Castañer, "Passive microstrip transmitarray lens for Ku band," in *Proceedings of the Fourth European Conference on Antennas and Propagation*, 2010, pp. 1-3.

[66] L. Chang, Z. Zhang, and Z. Feng, "A three-layer transmitarray element with 360° phase range," in *2015 IEEE International Symposium on Antennas and Propagation & USNC/URSI National Radio Science Meeting*, 2015, pp. 1868-1869.

[67] F. Diaby, A. Clemente, L. D. Palma, L. Dussopt, K. Pham, E. Fourn, and R. Sauleau, "Wideband circularly-polarized 3-bit transmitarray antenna in Ka-band," in *2017 11th European Conference on Antennas and Propagation (EUCAP)*, 2017, pp. 2269-2273.

[68] A. H. Abdelrahman, A. Z. Elsherbeni, and F. Yang, "Transmission Phase Limit of Multilayer Frequency-Selective Surfaces for Transmitarray Designs," *IEEE*

Transactions on Antennas and Propagation, vol. 62, no. 2, pp. 690-697, Feb. 2014.

[69] H.-T. Chen, J. Zhou, J. F. O'Hara, F. Chen, A. K. Azad, and A. J. Taylor, "Antireflection Coating Using Metamaterials and Identification of Its Mechanism," *Physical Review Letters,* vol. 105, no. 7, pp. 073901, Aug. 2010.

[70] H.-T. Chen, "Interference theory of metamaterial perfect absorbers," *Optics Express,* vol. 20, no. 7, pp. 7165-7172, Mar. 2012.

[71] Y. Zeng, H.-T. Chen, and D. A. Dalvit, "The role of magnetic dipoles and non-zero-order Bragg waves in metamaterial perfect absorbers," *Optics Express,* vol. 21, no. 3, pp. 3540-3546, Feb. 2013.

[72] M. Vaughan, *The Fabry-Perot Interferometer: History, Theory, Practice and Applications*: CRC Press, 2017.

[73] G. Hernandez, *Fabry-Perot Interferometers*: Cambridge University Press, 1988.

[74] J. R. Wait, *Electromagnetic waves in stratified media: Revised edition including supplemented material*: Elsevier, 2013.

[75] M. Born, and E. Wolf, *Principles of optics: electromagnetic theory of propagation, interference and diffraction of light*: Elsevier, 2013.

[76] T. B. Senior, and J. L. Volakis, *Approximate boundary conditions in electromagnetics*: Iet, 1995.

[77] I. V. Lindell, and A. Sihvola, *Boundary Conditions in Electromagnetics*: John Wiley & Sons, 2019.

[78] P. Nayeri, "Advanced design methodologies and novel applications of reflectarray antennas," Ph.D. dissertation, Department of Electrocal Engineering, The University of Mississippi, Ann Arbor, Michigan, 2012.

[79] C. A. Balanis, *Antenna theory: analysis and design*: John wiley & sons, 2016.

[80] P. Nayeri, A. Z. Elsherbeni, and F. Yang, "Radiation Analysis Approaches for Reflectarray Antennas [Antenna Designer's Notebook]," *IEEE Antennas and Propagation Magazine,* vol. 55, no. 1, pp. 127-134, Feb. 2013.

[81] A. D. Brown, *Electronically Scanned Arrays MATLAB® Modeling and*

Simulation: CRC Press, 2017.

[82] R. L. Haupt, and D. H. Werner, *Genetic algorithms in electromagnetics*: John Wiley & Sons, 2007.

[83] R. C. Hansen, *Phased array antennas*: John Wiley & Sons, 2009.

[84] A. Ludwig, "The definition of cross polarization," *IEEE Transactions on Antennas and Propagation,* vol. 21, no. 1, pp. 116-119, Jan. 1973.

[85] M. Zhou, E. Jorgensen, O. S. Kim, S. B. Sorensen, P. Meincke, and O. Breinbjerg, "Accurate and Efficient Analysis of Printed Reflectarrays With Arbitrary Elements Using Higher-Order Hierarchical Legendre Basis Functions," *IEEE Antennas and Wireless Propagation Letters,* vol. 11, pp. 814-817, Jul. 2012.

[86] M. Zhou, "Accurate modeling of advanced reflectarrays," Ph.D. dissertation, Department of Electrical Engineering, Technical University of Denmark, Lyngby, Denmark, 2013.

[87] M. Zhou, S. B. Sorensen, E. Jorgensen, P. Meincke, O. S. Kim, and O. Breinbjerg, "An Accurate Technique for Calculation of Radiation From Printed Reflectarrays," *IEEE Antennas and Wireless Propagation Letters,* vol. 10, pp. 1081-1084, Oct. 2011.

[88] P. Nayeri, F. Yang, and A. Z. Elsherbeni, *Reflectarray Antennas: Theory, Designs and Applications*: Wiley Online Library, 2018.

[89] H. Yang, F. Yang, S. Xu, M. Li, X. Cao, J. Gao, and Y. Zheng, "A Study of Phase Quantization Effects for Reconfigurable Reflectarray Antennas," *IEEE Antennas and Wireless Propagation Letters,* vol. 16, pp. 302-305, May 2017.

[90] Y. Mao, S. Xu, F. Yang, A. Z. Elsherbeni, "A Novel Phase Synthesis Approach for Wideband Reflectarray Design," *IEEE Transactions on Antennas and Propagation,* vol. 63, no. 9, pp. 4189-4193, Sep. 2015.

Publications

Journal:

[1] Sen Liu, Hiroyasu Sato, Qiang Chen, "A Wideband, 1-Bit Transmitarray Antenna Design with Flat Gain Response," *IEEE Trans. Antennas Propag.*, (Early Access; DOI: 10.1109/TAP.2020.2995417)

[2] Sen Liu, Qiang Chen, "A Wideband, Multifunctional Reflect-Transmit-Array Antenna with Polarization-Dependent Operation," *IEEE Trans. Antennas Propag.*, (Accepted)

[3] Sen Liu, Qiang Chen, "Transmitarray Antenna Design with Simultaneous Amplitude and Phase Modulations for Beam Shaping," *IEEE Trans. Antennas Propag.*, (Under Review)

Conference Proceeding:

[1] Sen Liu, "Dual-Beam Gain-Reconfigurable Antennas Using A Shared Reflectarray Aperture," in *2019 International Symposium on Antennas and Propagation (ISAP 2019)*, Oct. 2019, Xi'an, China.